Stereoscopic Reconstructions of Coronal Loops and Polar Plumes

Dissertation
zur Erlangung des Doktorgrades
der Mathematisch-Naturwissenschaftlichen Fakultäten
der Georg-August-Universität zu Göttingen

vorgelegt von
Li Feng
aus Taixing, Jiangsu, China

Göttingen 2009

Contents

Summary

The STEREO mission launched in October 2006 provides us for the first time with the opportunity to observe the Sun-Earth system in three dimensions. Two almost identical observatories on board make measurements almost simultaneously from two different vantage points in space. In this thesis we analyse the data taken by the EUVI telescope in the SECCHI instrument package, investigate the solar corona and concentrate on active regions and coronal holes. Coronal loops as the building blocks in active regions, and polar plumes, the most prominent and common features in coronal holes are of particular interest for this PhD thesis. A general introduction to the physical background of coronal loops and polar plumes is presented in Chapter 1. The instruments by which the data are produced and related analysis method are shown in Chapter 2.

After a detailed introduction to an automated loop segmentation tool in Chapter 3, in Chapter 4 we have reconstructed the 3D geometry of coronal loops from TRACE and EUVI image pairs by using the stereoscopic technique. It is shown that the loop geometry deviates from the assumptions used in previous studies, such as, loops lie in one plane and have symmetric shapes. The studies in this thesis have found that these assumptions are rarely satisfied. The comparison of the reconstructed 3D loops with the magnetic field lines extrapolated from linear force-free models with different force-free parameters has been made. Different loops often need to be fitted with different force-free parameters which tells us the linear force-free field model is not adequate to describe the magnetic field in the investigated active regions.

In Chapter 5, the 3D orientation and position of polar plumes has been stereoscopically reconstructed. The ten plumes investigated show a superradial expansion in the coronal hole in 3D which is consistent with the 2D results. Their deviations from the local meridian planes are rather small with an average of $6.47°$. By comparing the reconstructed plumes with a dipole field with its axis along the solar rotation axis, it is found that plumes are inclined more horizontally than the dipole field. The lower the latitude is, the larger is the deviation from the dipole field. We have calculated the plume width from two different viewpoints and find that they are consistent with a circular cross section. Given the small separation angle, more samples at large separations are however needed to come to a firm conclusion. By projecting the 3D plumes onto EUVI images, the relationship between plumes and bright points has been investigated. No one-to-one association has been found.

The combination of the 3D plumes with the SUMER observations could tell us more about the physical properties of plumes. The electron temperatures in three plumes do not vary very much and are lower than the interplume regions. The electron densities along the plumes decrease with height above the solar surface. The temperature obtained from the density scale height is $1.6 - 1.8$ times larger than the temperature obtained from

SUMER line ratios. We attribute this discrepancy to a deviation of the electron and the ion temperatures. Finally, we have found that the outflow speeds in the plumes corrected by the angle between the line-of sight and the plume orientation are quite small with a maximum of 10 km s^{-1}. This speed is too small to make plumes a dominant contributor to the fast solar wind.

1 Introduction

1.1 Solar atmosphere

The Sun is the only star on which we can study fundamental physical processes with high resolution. The source of the Sun's energy is produced by nuclear reactions in its core, transported from the core to the surface by photons in the radiative zone and by convection in the convective zone as shown in Figure 1.1. Above the solar surface is the solar atmosphere, divided into photosphere, chromosphere, transition region and corona.

A simple 1D temperature and density profile from the inner to outer solar atmosphere is presented in Figure 1.2. The photosphere is a thin layer of around 400 - 500 km at the top of the convective zone and is the visible surface of the Sun which can be seen by human eyes. The absorption lines in the photosphere are known as the Fraunhofer lines. Observed photospheric phenomena are sunspots, granules, supergranules and faculae. The temperature in the photosphere decreases with height and reaches to a minimum of about
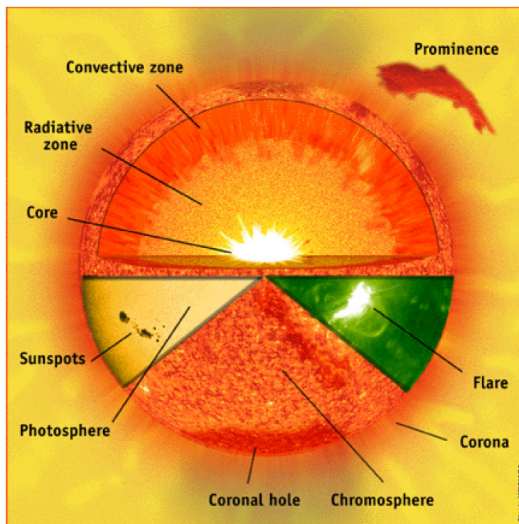
Figure 1.1: Sun structure from interior to atmosphere (sohowww.nascom.nasa.gov).
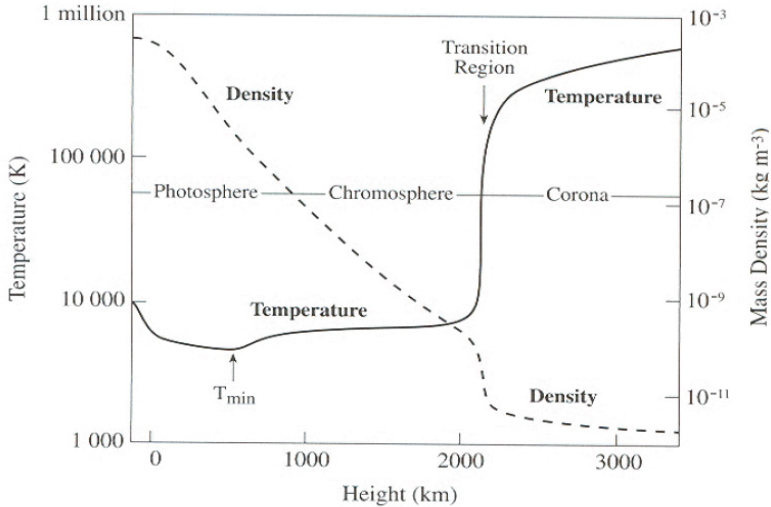
Figure 1.2: The 1D temperature and density stratification as a function of height (Lang 2001).

4500 K at the top of the photosphere. In the chromosphere the temperature rises to about 1×10^4 K. Energy is transported to this layer mainly by radiation and waves. The chromosphere is optically thin in the visible continuum spectrum and optically thick in strong resonance lines such as Hα and Ca II H and K. The features seen in the chromosphere are the network of magnetic elements, bright plages around sunspots, dark filaments across the disk and bright prominences above the limb. Above the chromosphere, the temperature rises drastically from 1×10^4 K to 1×10^6 K. This region is called the transition region where some emission lines in the ultra violet part of the solar spectrum are formed. The outermost layer of the Sun is called the corona which will be introduced in detail below. From the photosphere to the corona, the density decreases abruptly. It should be mentioned that Figure 1.2 only shows a simple 1D model. In reality, the structures in the solar atmosphere are more complicated and inhomogeneous.

1.2 Solar corona

The solar corona obtained its name from the crown like appearance evident during a total solar eclipse. The coronal emission in the visible is faint and can only be observed from the Earth during a total solar eclipse or by means of a coronagraph when the bright photosphere is occulted. For the solar physicist, solar corona is a beautiful and mysterious feature to study. It harbours many eruptive phenomena, such as flares and coronal mass ejections (CMEs). Due to the high temperatures in the solar corona, gravity alone cannot

keep the plasma to the Sun. Where not confined by the magnetic field, it may expand into the interplanetary medium as a continuous stream of particles called the "solar wind". Although its high temperature has been found for over 60 years, up to now, we do not know yet why the temperature in the corona is so high and what are the sources of the heating energy.

The solar corona has three components:

K corona: Kontinuum Corona

The visible coronal radiation (the white-light corona) is primarily composed of two different parts: the K corona and the F corona. The K corona extends between $\sim 1.03\,R_\odot < R < 2.5\,R_\odot$ and it named after the German "Kontinuum". Its continuum spectrum resembles the photospheric spectrum without the Fraunhofer lines (absorption lines). The K corona is produced by Thomson scattering of photospheric light by free electrons in the corona. Due to the high temperature of the coronal electrons, the absorption lines are broadened and mixed with the continuum. Since it is produced by Thomson scattering, the light of the K corona is highly polarized.

F corona: Fraunhofer Corona

The F corona dominates outwards from around $2.5\,R_\odot$. The prefix F is dedicated to Fraunhofer. It displays the Fraunhofer lines superimposed on the continuum solar spectrum as it is mainly produced by the photospheric light scattered by dust particles into the interplanetary space and is weakly polarized. Two images of the white-light corona at solar activity maximum and minimum are presented in Figure 1.3. At activity maximum, the corona is seen all around the Sun, while at activity minimum, the corona is quite different and polar coronal holes appear.

E corona: Emission Corona

The E component comprises the corona in emission lines and has a very wide spectrum from radio waves to ultraviolet and X-rays. The two strongest emission lines in the visible E corona are the Fe xiv 5303 Å and Fe x 6374 Å. The corona emits a very rich spectrum of ultraviolet and extreme ultraviolet (UV/EUV) lines. Images taken with the narrow-band spectral filters selected from some of these lines exhibit the density information of the respective highly-ionized atoms. Figure 1.4 shows the corona observed by the EUVI (Extreme Ultraviolet Imager) telescope on board STEREO (Solar-Terrestrial Relations Observatory) at three wavelengths 171 Å, 195 Åand 284 Å corresponding to the peak temperature of about 1.0 MK, 1.5 MK and 2.0 MK (details on the instrument will be introduced in Chapter 2). Emission at wavelengths less than 100 Å is referred to as X-rays and is often related to higher energy radiation from the hottest regions of the corona. An image taken by the XRT (X-Ray Telescopy) on board Hinode is presented in Figure 1.5.
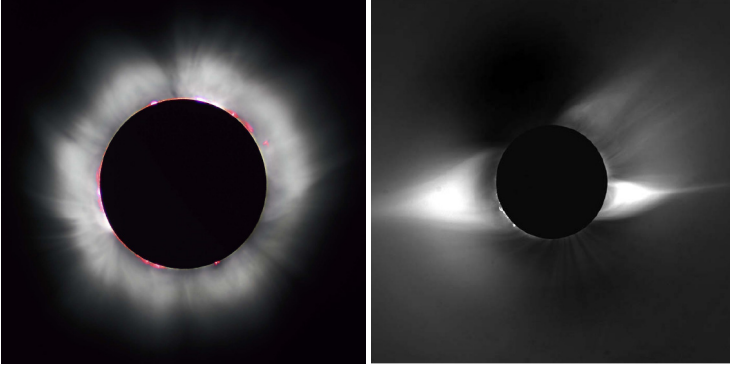
Figure 1.3: The white light corona observed during the total solar eclipses in August 1999 at solar activity maximum (left) and in November 1994 at solar minimum (right). The rosy color features around the solar disk in the left panel is the chromosphere (adapted from http://en.wikipedia.org and http://www.nasa.gov, respectively).

1.2.1 Solar corona and magnetic fields

In the above we have seen the corona at different wavelengths. Because of the high conductivity and the lower plasma β defined as the ratio of the thermal pressure to the magnetic pressure in the corona, magnetic fields dominate the structures. The solar corona is usually divided into three regions, active regions, coronal holes and quiet Sun regions, which have very different magnetic field characteristics, as shown in Figure 1.6. In active regions and the quiet Sun, field lines are dominantly closed, whereas in the polar coronal hole, open field lines are dominating. On the right side of Figure 1.6, a global potential magnetic field model at the solar activity minimum is exhibited. The magnetic field lines in the active region in the northern hemisphere are almost closed, while in the two polar caps are mainly open field lines. A good working definition of quiet Sun regions is the region encompassing all closed magnetic field regions excluding active regions (Aschwanden 2005b). The name "quiet Sun" does not mean that this region is really quiet. In fact, many dynamic processes in small-scale phenomena have been found as the spatial resolution of telescopes has improved, such as bright points, explosive events. Since the structures in active regions and coronal holes are analysed in this thesis, a more detailed description on them will be given below.

1.2.2 Active regions

Active regions are the locations of highly concentrated magnetic field. The heliographic position of active regions is typically confined in bands located at latitudes of $\pm 40°$ with respect to the solar equator. With the dynamic plasma motions in the photosphere and chromosphere, the magnetic field in active regions is reconfigured by flux cancellation and magnetic reconnection. Big eruptive events like solar flares and CMEs usually occur
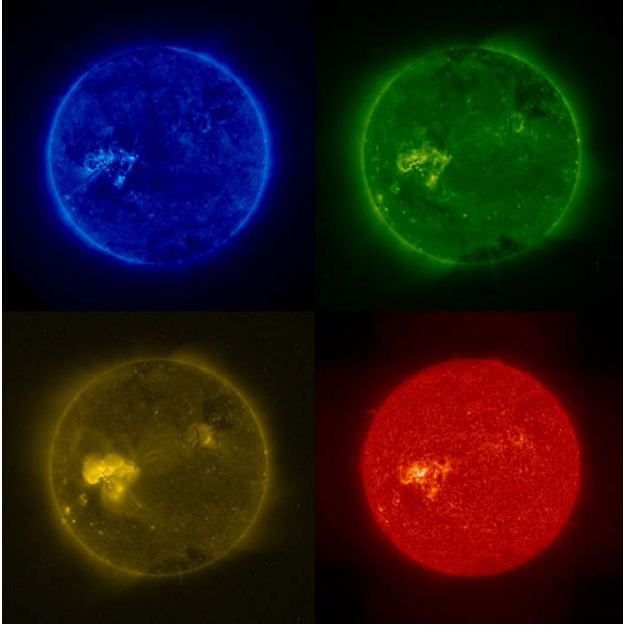
Figure 1.4: Four images at four different EUV wavelengths taken by EUVI telescope on board STEREO on December 4 2006. From upper to bottom and left to right are, respectively, the corona images at 171 Å , 195 Å , 284 Å and the transition region images at 304 Å (from http://www.nasa.gov).

in active regions. A solar flare is a sudden, rapid, and intense variation in brightness and occurs when magnetic energy that has built up in the solar atmosphere is suddenly released. Radiation is emitted across virtually the entire electromagnetic spectrum. A CME is an impulsive ejection of chromospheric and coronal material from the solar corona, usually observed with a coronagraph. Most of the CMEs originate from active regions and are often associated with other solar active phenomena, e.g., solar flares, eruptive prominences, coronal dimmings and EIT waves.

Coronal magnetic loops are the building blocks in active regions. They maybe quite twisted before an eruptive event happen as presented in Figure 1.7 (also in Figure 1.5). Another spectacular loop system are the post-flare loops which are large-scale and bright transient loop systems that are thought to form in the corona after the magnetic reconnection above the loop system occurred. They are best visible at EUV wavelengths (Figure 1.8). Solar flares sometimes can excite transverse oscillations (Aschwanden et al. 1999a, Schrijver et al. 2002, Wang and Solanki 2004) or longitudinal oscillations (Wang et al. 2002, 2003) of the adjacent coronal loops.

The coronal loops not associated to these large eruptive events are also important from
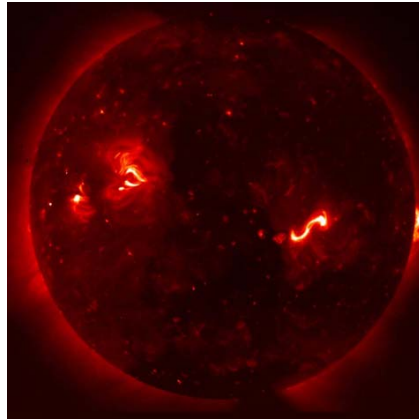
Figure 1.5: The corona in Soft X-rays (SXR) taken by XRT (X-Ray Telescopy) on board Hinode in February 2007 (Courtesy of Hinode/XRT consortium).
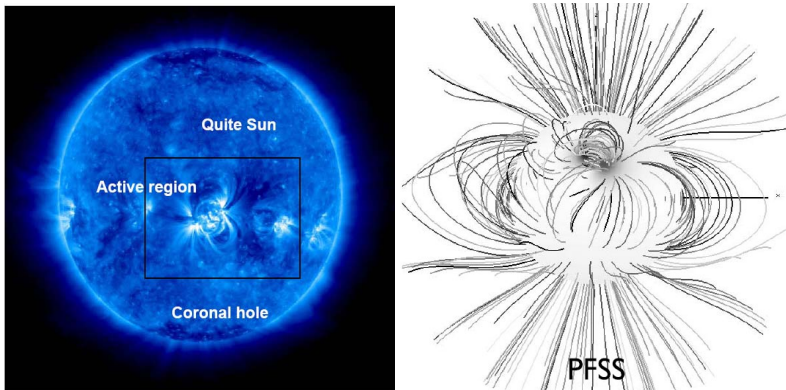
Figure 1.6: Left: three different regions in the solar corona indicated in the image taken by EUVI on June 2007. Right: a global potential field model at the solar activity minimum on another day to show the open and closed field line regions. (Riley et al. 2006).
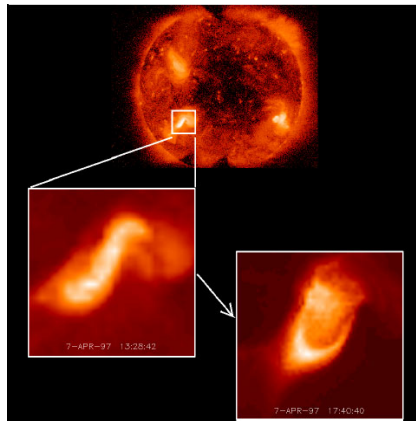
Figure 1.7: The SXR coronal loops observed on April 7 1997 before (at 13:38 UT) and after (at 17:40 UT) a CME (Courtesy of Yohkoh consortium).
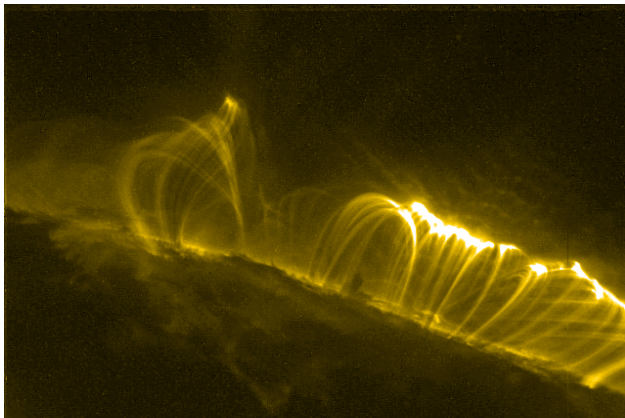
Figure 1.8: The post-flare loop system observed by TRACE at $\lambda = 195$Å on November 4 2003 (Courtesy of TRACE consortium).
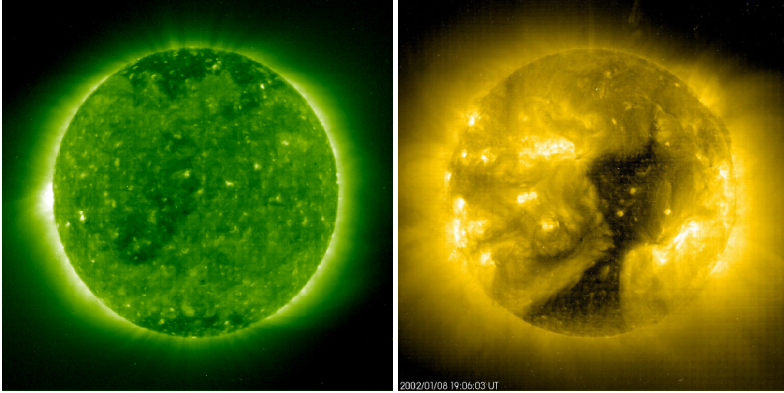
Figure 1.9: Left: the EIT image showing the polar coronal holes at $\lambda = 195\text{Å}$ taken in November 1996 during the solar activity minimum. Right: the coronal hole extended from the south polar cap to the north hemisphere taken by EIT at $\lambda = 284\text{Å}$ in January 2002 during the solar maximum. (Courtesy of the SOHO/EIT consortium).

the viewpoint of coronal heating, since big eruptive events do not occur as frequently as the small eruptions (§9.8 in Aschwanden 2005b). They look more quiescent in active regions and can be observed in SXR and EUV wavebands. Actually, most of them are poorly consistent with the static loop models according to Winebarger et al. (2003) and loops observed in EUV are more dynamic than those observed in SXR. Until now it is unclear yet how these quiescent loops are heated and whether the SXR and EUV loops have different heating mechanisms. The cooling of active region loops has been suggested to be driven first by the electron heat conduction from the corona to the chromosphere then by radiative loss (Winebarger and Warren 2004).

1.2.3 Coronal holes

Coronal holes are regions of significantly reduced emission in all spectral lines formed at coronal temperatures. They can last over several solar rotations. They are linked to funnel-like unipolar concentrations of open magnetic field lines and act as efficient conductors for transporting heated plasma from the corona to interplanetary space. Therefore, coronal holes are the primary source of the fast solar wind. Because of the dominantly open field line structures, coronal holes are most of the time "empty", with lower density and temperature and thus appear darker than the quiet Sun surface regions. During solar minimum, coronal holes are mainly found at the Sun's polar regions, but they can be located anywhere on the Sun during solar maximum. In Figure 1.9, an example is presented of coronal holes at solar activity minimum and maximum respectively. During the solar maximum in January 2002, the southern polar coronal hole extended out to the north hemisphere.

On large scales and in UV and X-ray wavelengths, coronal holes appear much more
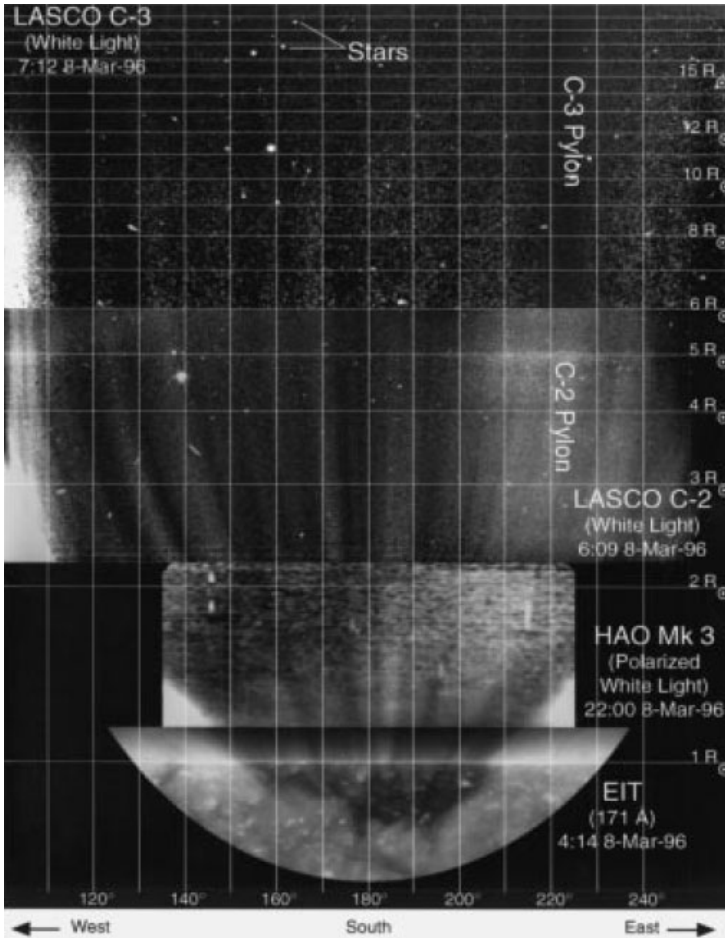
Figure 1.10: Polar plumes observed by four different instruments aboard SOHO in March 1996 (Deforest et al. 1997).

homogeneous comparing to other regions of the Sun. However, if they are seen in chromospheric and transition region lines, the chromospheric network is the most basic structure. Moreover, if observed with high spatial and temporal resolution, coronal holes are highly structured including polar plumes, polar jets, bright points, spicules, macrospicules, and so on. The spatial scales of these structures spatially range from 1 arcsec to several tens of arcsec, and they vary temporally from 1 minute to several days.

Plumes are ray-like structures above the polar caps best visible during the solar activity minimum with a lifetime of several hours to days. They were first found in white light and called polar rays (e.g. Saito 1965). In Deforest et al. (1997) plumes are analysed by taking the observations by SOHO (Solar and Heliospheric Observatory) including the instruments of MDI, EIT, CDS, SUMER, UVCS and LASCO C2 and C3, the ground based HAO Mk 3 white-light coronagraph. The morphology of the plumes observed over the south pole of the Sun is shown in Figure 1.10 and individual plumes have been characterized from the photosphere to approximately 15 $R_\odot$ in polar coordinates. Deforest et al. (1997) have shown that most investigated white-light polar rays can be directly associated with the EUV polar plumes and their footpoints on the solar surface. Plumes are estimated to occupy about 10% of the polar hole volume and reveal superradial expansion to 30 $R_\odot$, if seen in white light (DeForest et al. 2001b). Soft X-rays possibly show mainly the hot plasma at the footpoints of the plumes (Ahmad and Webb 1978), which are also seen as weak radio sources (Gopalswamy et al. 1992). Various efforts have been made to measure the temperature and density of plumes at the base and above the limb (e.g. Young et al. 1999, Wilhelm 2006). From these studies, plumes were identified as cooler and denser structures as compared to the surrounding atmosphere in coronal holes. Often plumes are associated with bright points in coronal holes although there is no one-to-one relation (Wang 1998). Recently Raouafi et al. (2008) found from the observations by Hinode/XRT and STEREO/EUVI that polar jets could be regarded as precursors of polar plumes.

1.2.4 Why do we need 3D?

With the launch of STEREO in October 2006, a new dimension of the Sun has been opened. For the first time we are able to observed the Sun from two different viewpoints simultaneously, which provides us with the opportunity to see the Sun in three dimension. In this thesis the 3D geometry of the coronal loops in active regions and polar plumes in coronal holes are reconstructed. As we will see in the following, the knowledge of their geometry is quite helpful for a better understanding of their physical background.

Why do we need 3D loops?

In the research field of coronal loop modelings, we often compare the observed intensity with the intensity synthesized from the temperature and density results of loop models to obtain some information about the free parameters in models, like loop heating functions (Reale et al. 2000a,b). If we want to synthesize the intensity along one loop correctly, the cosine of the angle between the line of sight and the local tangent direction along the 3D loop should be taken account of. This cannot be done without the 3D loop geometry. As shown in Wood and Raymond (2000) and Alexander and Katsev (1996), the optically thin emissions in one simulated loop from different view directions can present quite different emission distributions along the loop (Figure 1.11). When viewed from above, the geometrical projection causes the footpoints to appear bright where the line-of-sight direction and the local tangent direction are close to parallel. While an edge-on view direction produces an emission maximum at the loop top simply due to the increased path length toward the apex.
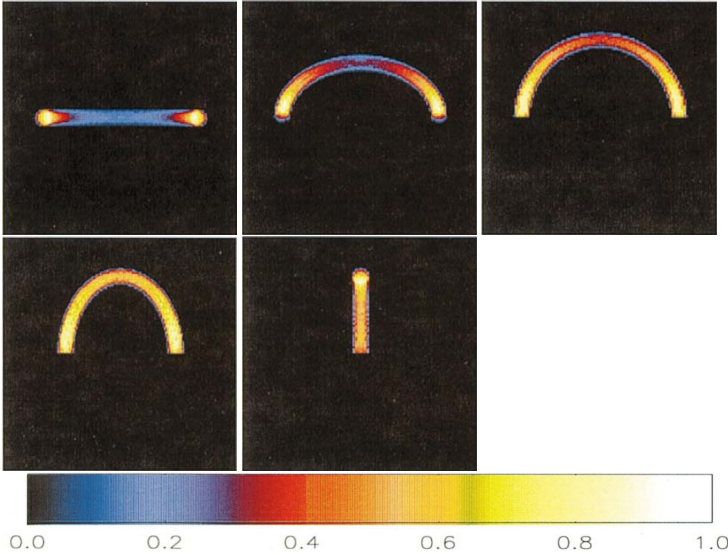
Figure 1.11: Semicircular loop images at different viewing angles with a maximum temperature at the loop top of $logT_{max} = 6.8$. The panels from left to right and upper to bottom are (1) directly above, (2) 45° from vertical, (3) face-on, (4) rotate by 45° and (5) edge-on (Wood and Raymond 2000).

In the previous studies of active region modelings before STEREO the emission from quite a number of loops was simulated assuming loop geometries, which were often approximated by magnetic field extrapolations (Warren and Winebarger 2006, Lundquist et al. 2008a,b). To test theories of coronal heating by the relationship between intensity and the unsigned magnetic flux, one difficulty is the estimates of the loop length, which were hampered by projection effects and the superpositions of structures along the line of sight (Warren and Winebarger 2006). With the STEREO data available, this problem can be reduced by the 3D reconstructions of coronal loops (Aschwanden et al. 2009) where they obtained better modelled active region morphology than previous work. Furthermore, the derived 3D loop length can be utilized to test loop scaling laws, for example, the RTV scaling laws, which predicts the relation between the pressure at the footpoint, the maximum temperature and the loop length (Rosner et al. 1978).

A yet unsolved problem is that in loop observations the apparent loop width hardly changes with height as it should if the hot emitting plasma is confined by a magnetic flux tube bounded by magnetic surfaces. With increasing height above the surface, the flux tube cross section should increase as a result of the flux conservation. However, from observations in both EUV and SXR wavebands nearly constant cross sections are repeatedly found (Klimchuk 2000, Watko and Klimchuk 2000). With the 3D loops reconstructed from STEREO we can check whether the distortion of the flux tube shape is caused by
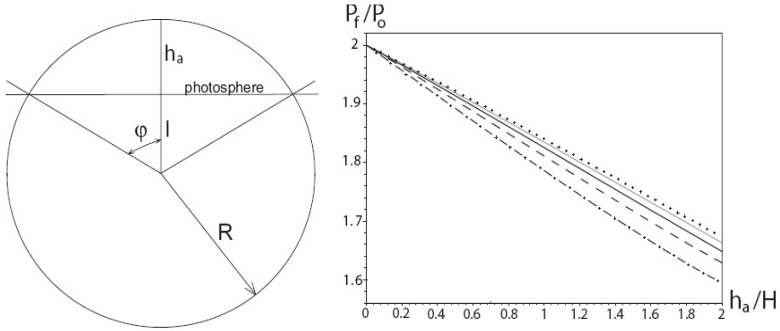
Figure 1.12: The left panel shows the loop shape parameter used by Dymova and Ruderman (2006). The loop is approximated by an arc of a circle of radius R. l is the distance of the circle center to photosphere and being positive when the center is below the photosphere. The right panel is the ratio of periods, P_f/P_0 as a function of the density stratification for different values of the geometrical parameter $\lambda = l/R$. H is the density scale height.

the view angle as suggested by Klimchuk et al. (2000). Another question is whether an isolated loop we observed is a single flux tube. If it is, the cross-sectional shape is highly unlikely to be simple or keep the same shape along its entire length, this can be checked by computing the loop width along the loop at each corresponding point from two EUVI view directions.

By associating one 3D loop with its best fit field line from magnetic field extrapolations from the high spatial resolution magnetogram data (SOLIS, SDO), we can reconstruct a corresponding flux tube to the observed loop. Then we can estimate how magnetic field strength decreases with height in the flux tube more precisely than previous studies, subsequently the flux tube expansion factor can be derived. In this way a one-to-one comparison of the observed loop width with the width of its corresponding magnetic flux tubes could be made.

Another prospective application of the 3D geometry of loops is the loop oscillations. Wang et al. (2008) show that the kink modes of loop oscillations can be misidentified if viewed only from one direction. Dymova and Ruderman (2006) discussed about the geometry effect on transverse oscillations of coronal loops. They found the the ratio of the fundamental mode, P_f, and the first overtone, P_o, depends on the loop geometry (Figure 1.12). As also stated in Aschwanden et al. (2002), a more accurate determination of the oscillation parameters should include the projection effects of the 3D loops. The measured periods which related to the loop length can in principle be used to constrain the Alfven speed, and thus the coronal magnetic field strength. Furthermore, 3D reconstructions of elementary loop structures are of fundamental importance for studying the associated (non-potential) magnetic field and related electric currents.

Why do we need 3D plumes?

In the research of polar plumes, there are still two debates ongoing. One is related to the role of polar plumes for the fast solar wind. In general, plumes are thought to harbor smaller outflow speeds than the interplume regions, which is based on SOHO/SUMER Doppler shift measurements (Hassler et al. 1999, Wilhelm et al. 2000) and simulations (Wang 1994). The SUMER observations have shown that close to the solar limb, polar plumes seem to be nearly in hydrostatic equilibrium and show very small or no line shifts. Doppler dimming techniques applied to SOHO/UVCS derived the same conclusion. Giordano et al. (2000) found that at the height of 1.7 $R_\odot$ the outflow speeds in the interplume regions range from 100 to 150 km s^{-1}, while in bright plumes outflows are much lower from 0 to 65 km s^{-1}. However, Gabriel et al. (2003) used the same Doppler dimming techniques to SUMER data in the height range of $1.05 - 1.35\ R_\odot$ and reached an opposite conclusion: the outflow speeds in plumes are higher than in interplume regions and plumes makes a substantial contribution to the total line of sight.

Another important question to be answered is what are the magnetic structures at the plume footpoints. Some observations have shown that plumes are rooted in unipolar regions. Newkirk and Harvey (1968) suggested that plumes originate in unipolar regions at the intersection of chromospheric network boundaries. While Deforest et al. (1997) agreed to the unipolar magnetic property of plume footpoints, they have shown from MDI and CDS observations that plume footpoints are located within the chromospheric network. On the contrary some people suggested a completely different picture that plumes are associated with mixed polarity magnetic features at the footpoints (Wang and Sheeley 1995, Wang 1998) and formed by magnetic reconnection between bipoles and the background unipolar fields. This is supported by the higher temperature at the plume footpoints and the high density plasma produced by the chromospheric evaporation into the plume. DeForest et al. (2001a) have found that polar plumes are both transient and persistent structures: they are recurring structures that brighten for about one day but reappear at approximately the same location intermittently for up to 2 weeks. This temporal behaviour is consistent with single large unipolar flux concentrations encountering multiple ephemeral bipolars under the influence of supergranulation, suggesting that polar plumes are indeed formed by small scale magnetic reconnection events driven by supergranular motions.

One handicap of all previous studies was the fact that plumes, even though well visible in 2D images beyond the limb, could not be reliably traced to the solar surface. With their 3D reconstructions from EUVI image pairs close to the solar surface, their footpoints can be extrapolated from the known 3D geometry if we assume that the plumes in EUVI images can be approximated by straight lines. Hence, by plotting the footpoints into a photospheric or chromospheric magnetogram, the magnetic properties of plume footpoints can be derived. Another application of 3D plumes is their orientation. Since the outflow speed calculated from Doppler shift or Doppler dimming is along the line of sight or perpendicular to the line of sight, respectively, a true outflow speed can be obtained by correcting for the angle between the line of sight and the plume orientation.

1.3   Research program of the present thesis

This thesis focuses on the stereoscopic reconstructions of coronal loops and polar plumes from the SECCHI/EUVI images. As explained in the preceding discussions, 3D geometry of coronal loops and polar plumes are important for our understanding the physics in active regions and coronal holes.

The structure of the rest of this thesis is arranged in the following. In Chapter 2, the instruments and related data analysis techniques including stereoscopy, EUV emission line spectroscopy and linear force-free coronal magnetic field extrapolation are introduced. In order to extract loop structures from 2D EUV images, the design of an automated loop detection tool is presented in Chapter 3 . Based on the extracted coronal loops from EUV images taken from two different viewpoints, in Chapter 4 the stereoscopic reconstructions of loops are exhibited first from two TRACE images taken about one day apart and using the solar rotation as a test before the STEREO data was available. Then the 3D loop reconstructions are performed by using the real SECCHI/EUVI data. In Chapter 5 we shift the 3D reconstructions from active regions to coronal holes and 3D polar plumes are reconstructed. By combining the 3D geometry with SOHO/SUMER observations, the electron temperature and density in plumes are obtained. In the end, the concluding Chapter 6 of this thesis summarizes the main conclusions and gives an outlook for future work.

2 Instruments and related data analysis techniques

In Chapter 1 we have presented some beautiful images in different wavelengths of the solar atmosphere taken by a few delicately designed space missions, such as SoHO, TRACE, Hinode, STEREO, etc, which have been greatly improving our understanding of the Sun. In this chapter we will first briefly introduce the instruments related to this thesis, then show how to analyse the data observed by them.

2.1 Instruments

2.1.1 SoHO

SOHO (Solar and Heliospheric Observatory) is a project of international collaboration between ESA and NASA to study the Sun from its deep core to the outer corona and the solar wind. The SOHO spacecraft was launched in December 1995 and orbits around the Sun together with the Earth by slowly orbiting around the First Lagrangian Point (L1) where the satellite is balanced by the gravitation of the Sun and the Earth and the centrifugal force. The scientific payload of SOHO comprises 12 instruments that are complementary to each other and can be divided into three main groups: helioseismology instruments (GOLF, VIRGO and MDI/SOI), solar atmosphere remote sensing instruments (CDS, EIT, SUMER, UVCS, LASCO and SWAN), and solar wind in situ instruments (CELIAS, COSTEP and ERNE). Here we introduce three of them, MDI, EIT and SUMER, which are relevant to the work described in this thesis.

2.1.1.1 MDI

MDI (Michelson Doppler Imager) was designed to study the interior structure and dynamics of the Sun by the approach of helioseismology. It measures the line-of-sight velocity, continuum intensity and the line-of-sight magnetic field component with the spectral line of Ni I at $\lambda = 6768$Å. The detailed description of MDI was given by Scherrer et al. (1995). What we are interested in is the magnetic field measurement in the photosphere as it provides the boundary conditions for the calculation of the magnetic field in the solar corona. MDI images the Sun on a 1024^2 CCD camera and has two modes of observations from the spatial resolution point of view. One is the full disk observations with a resolution of $1.98''/pixel$, the other mode is taken in a higher resolution of $0.63''/pixel$ which leads to a magnetogram of part of the solar surface.
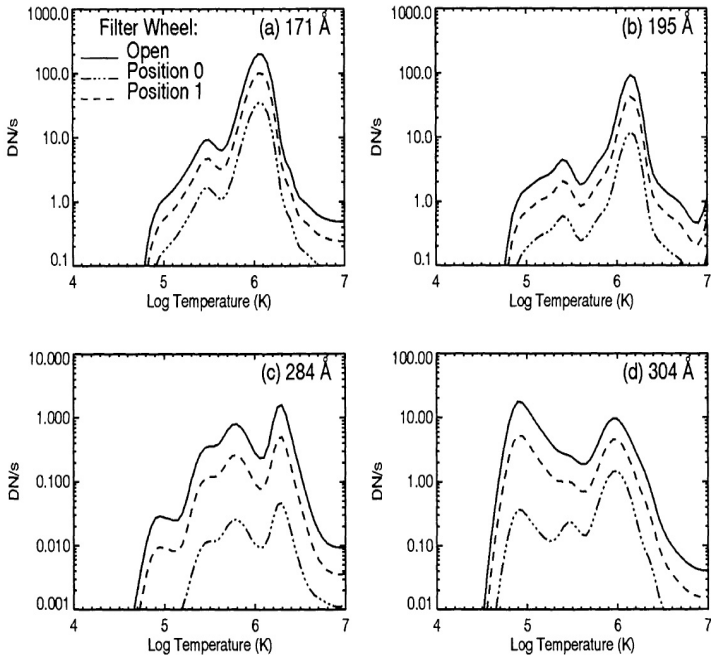
Figure 2.1: Estimated signal strength in the CCD (Date Number/s) for the four wavelengths of EIT as a function of temperature for a emission measure of 10^{44} cm^{-3} (Delaboudinière et al. 1995).

2.1.1.2   EIT

The telescope EIT (Extreme-ultraviolet Imaging Telescope) was designed to investigate the dynamics of the chromospheric network, transition region and coronal structures over a wide range of time scales, sizes and temperatures. It provides full disk images out to 1.5 $R_\odot$ with an approximated $2.6''/pixel$ spatial resolution from four spectral emission lines, Fe IX (171 Å), Fe XII (195 Å), Fe XV (284 Å) and He II (304 Å). The CCD's temperature response functions are shown in Figure 2.1 which are similar to the ones of TRACE and EUVI instruments to be introduced later. We can see that EIT covers the temperature range from 6×10^4 K to 3×10^6 K with a peak temperature around 1.2 MK, 1.5 MK, 2.0 MK and 0.08 MK for the four wavelengths, respectively. On the other hand, EIT images are also helpful to correct the pointing information in TRACE images at the same wavelength. For a detailed description of EIT see Delaboudinière et al. (1995).
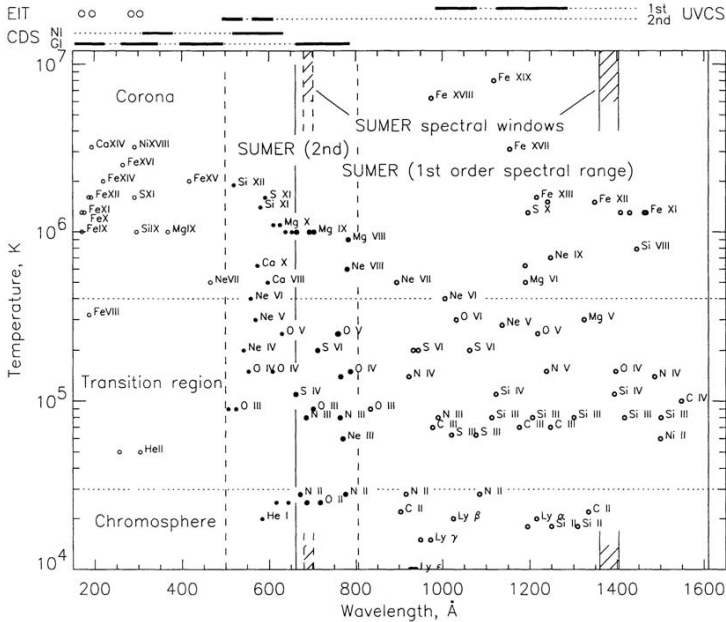
Figure 2.2: Selected important emission lines in the wavelength range from 150 Å to 1610 Å by the combination of SUMER, CDS, UVCS and EIT vs their formation temperatures (Wilhelm et al. 1995).

2.1.1.3 SUMER

SUMER (Solar Ultraviolet Measurements of Emitted Radiation) (Wilhelm et al. 1995) is a spectrograph and measures spectral profiles of FUV/EUV lines emitted by the solar atmosphere from the upper chromosphere to the lower corona with a wide spectral coverage ranging from 500 Å to 1610 Å corresponding to line formation temperatures from 10^4 K to above 2×10^6 K. SUMER aims to obtain dynamic and diagnostic information of the solar atmosphere with a spatial resolution close to $1''$, a temporal resolution of down to $1\ s$, and a spectral resolving power of $\lambda/\triangle\lambda = 17700 - 38300$ ($\triangle\lambda$ is the pixel resolution element). Figure 2.2 gives us the important emission lines selected by SUMER in a formation temperature versus wavelength plot. For plume studies in this thesis we choose the emission line pair Mg IX at 70.6 nm and 75.0 nm for electron temperature measurements, Si VIII at 144.0 nm and 144.6 nm for electron densities and O VI at 103.2 nm and 103.8 nm for Doppler shifts. A raster scan was made for the south polar cap from solar west to east for around 36 hours while the Sun was rotating.
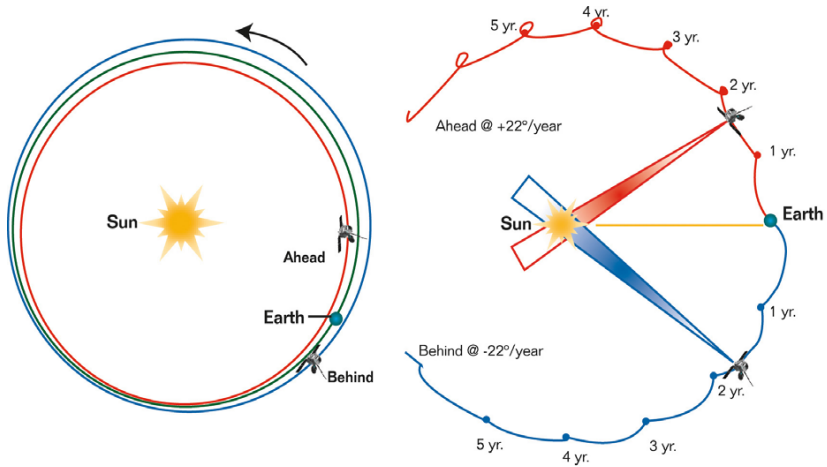
Figure 2.3: The trajectory of STEREO A and B in different years (adapted from NASA STEREO website).

2.1.2 TRACE

TRACE (Transition Region and Coronal Explorer) (Handy et al. 1999) uses multiple UV and normal-incidence XUV channels to collect images of atmospheric plasmas at temperatures from 10^4 K to 10^7 K. In the EUV waveband TRACE observes similar emission lines as EIT, that is, 171 Å, 195 Å and 284 Å. The most prominent characteristics of TRACE is its highest spatial resolution of $0.5''/pixel$, which is the highest of all currently available solar EUV images. The CCD of TRACE is 1024×1024, the same as EIT. Owing to the high spatial resolution, its field of view is only $8.5' \times 8.5'$.

2.1.3 STEREO

The STEREO (Solar-Terrestrial Relations Observatory) mission was launched in October 2006. It provides a unique and revolutionary view of the Sun-Earth System. The main scientific objectives are to understand the causes and mechanisms of coronal mass ejection (CME) initiation and to follow the propagation of CMEs through the inner heliosphere to Earth. As viewed from the Sun, the two nearly identical observatories, one ahead of Earth in its orbit, the other trailing behind, separate at approximately 44 to 45 degrees per year. The trajectories of the two spacecraft at different times is presented in Figure 2.3. Each spacecraft is equipped with four instrument packages, SECCHI (Sun Earth Connection Coronal and Heliospheric Investigation), IMPACT (In-situ Measurements of

Particles and CME Transients), PLASTIC (PLAsma and SupraThermal Ion Composition) and S/WAVES (STEREO/WAVES).

The SECCHI suite is an imaging instrument package. It contains two white light coronagraphs (COR 1 and COR 2), an extreme ultraviolet imager (EUVI) and two heliospheric white light imagers (HI 1 and HI 2) covering the space from the solar corona to 1 AU. The first year after STEREO's launch, while the spacecrafts' distance to each other is still moderate, is the phase of 3D reconstructions of coronal structures, such as the coronal loops and polar plumes which are the major work in this thesis. As we know, loops and plumes are well observed at EUV wavelengths. Therefore we will concentrate on the EUVI instrument. It is actually an updated version of EIT and has four similar emission lines to EIT, 171 Å, 195 Å, 284 Å and 304 Å. But comparing with EIT, it has a large field of view extending to $1.7R_{\odot}$ and higher spatial resolution of $3.2''$ attributed to the large CCD of 2048×2048. In this thesis, we will use the images observed at the wavelength of 171 Å as it produces the sharpest coronal structures comparing to the other three wavelengths. For more details about SECCHI and the EUVI telescopes see Howard et al. (2008) and Wuelser et al. (2004), respectively.

2.2 Data analysis techniques

In this section the data analysis techniques related to the introduced instruments are described. The stereoscopy technique is applied to reconstruct the 3D geometry of coronal features observed from two viewpoints by EUVI/SECCHI. Before STEREO was launched, stereoscopy has been applied to TRACE or EIT data making use of the solar rotation. Typically, image pairs taken one day apart were used and simplified assumptions were made about the evolution of the observed structures (Aschwanden et al. 1999b). The second technique is introduced for SUMER observations to diagnose plasma in the solar corona by using the line-ratio method. Finally the magnetic field models are presented. The linear force-free field models are extrapolated from the MDI photospheric magnetograms.

2.2.1 Stereoscopy and epipolar geometry

STEREO provides us for the first time with two simultaneously observed images of the Sun from different vantage points. Once an object is identified in both images, the 3D reconstruction is a purely linear geometrical problem. However, the most challenging problems associated with stereoscopy preceding the geometrical reconstruction are the identification of objects in the two images and the determination of correspondences between them. We leave these two tasks to Chapter 3 and Chapter 4, respectively. Here we summarize the geometrical method related to curve-like objects, such as coronal loops and polar plumes. The basics of the stereoscopy technique can be found in Inhester (2006a).

For curve-like objects, the principle of stereoscopy is shown in Figure 2.4. From both observational points, we backproject the extracted curves in the images along the two viewing directions and obtain two projection surfaces. The intersection of these two surfaces yields a unique 3D curve in the ideal case which is the solution to the stereoscopic reconstruction. To calculate this intersection, the epipolar geometry is applied to
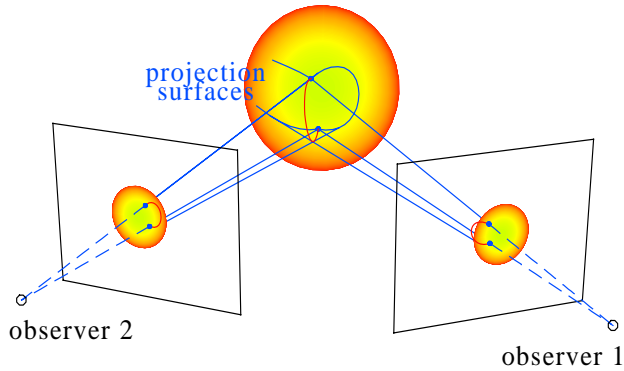
Figure 2.4: Backprojections to reconstruct the 3D structure of a curve-like object (Inhester 2006a).

transform the 3D problem into a set of 2D problems.

2.2.1.1   Epipolar geometry

The epipolar geometry is sketched in Figure 2.5. The line connecting the two observers is called the stereo base line. The reference axis epi_z originates from the solar center and is normal to the plane determined by the two observers and the solar center. If we pick up one point $\mathbf{r_0}$ on the epi_z axis, the two observers and $\mathbf{r_0}$ define an epipolar plane. The intersection of this plane with the two image planes generates two straight lines. They are the so-called epipolar lines. By selecting a series $\mathbf{r_0}$, we segment each image densely into a large number of epipolar lines and get a set of epipolar planes. As we will see below, on each epipolar plane a 3D coordinate can be easily calculated from two corresponding 2D points from two images. By connecting the 3D points on each epipolar plane, a final 3D curve will be achieved.

Practically, we set up one coordinate system as shown in Figure 2.5 for calculations and here we choose the HEEQ (Heliocentric Earth EQuatorial) coordinate system (Thompson 2006). The z axis is the solar rotation axis, x axis is the intersection of the solar equator with the central meridian as seen from the earth, and y axis is in the direction of the cross product of z and x axes to make the coordinate system right-handed. The positions of two spacecraft in this coordinate system is given in each header of the fits files.

A demonstration of the calculation of one 3D point $\triangle\mathbf{r}$ in one certain epipolar plane is presented in Figure 2.6. In one given epipolar plane, $\mathbf{r_0}$ is the intersection of the respec-
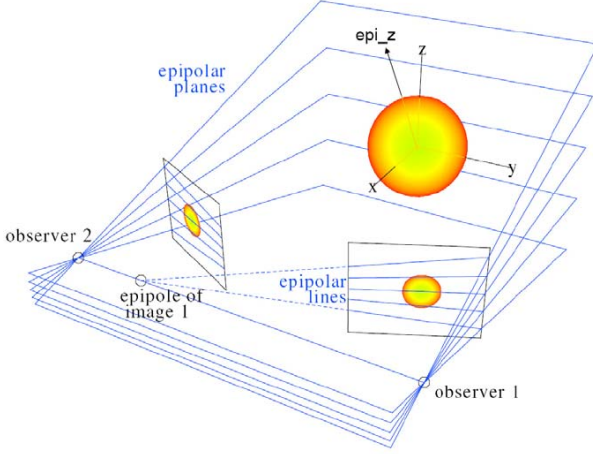
Figure 2.5: A schematic diagram of epipolar planes in space and the respective epipolar lines in two image planes. The observers telescope screens are derived from a projective camera model. The *epi_z* axis originates from the solar center and is normal to the plane determined by the two observers and the solar center (Inhester 2006a).

tive epipolar plane with the *epi_z* axis, $\mathbf{r_1}$ and $\mathbf{r_2}$ represent the two observers. For each observer we then introduce the orthogonal coordinate axes $\mathbf{v_i}$ and $\mathbf{e_i}$. $\mathbf{v_i}$ is the unit vector from the observer to $\mathbf{r_0}$ and $\mathbf{e_i}$ is $\mathbf{v_i}$ rotated clockwise by 90°. d_i is the distance between the observer and $\mathbf{r_0}$. All of these quantities can be calculated explicitly in the HEEQ coordinate system from the known spacecraft position and the given position of $\mathbf{r_0}$. From Figure 2.6, we can derive

$$\tan(s_i) = \frac{\mathbf{e_i^T} \cdot \triangle \mathbf{r}}{d_i + \mathbf{v_i^T} \cdot \triangle \mathbf{r}}. \tag{2.1}$$

where s_i is the angle between $\mathbf{v_i}$ and the direction to the object. Writing Equation 2.1 in another form and for two observers, we get

$$\left(\begin{array}{c} \mathbf{e_1^T} - \mathbf{v_1^T} \tan s_1 \\ \mathbf{e_2^T} - \mathbf{v_2^T} \tan s_2 \end{array} \right) \triangle \mathbf{r} = \left(\begin{array}{c} d_1 \tan s_1 \\ d_2 \tan s_2 \end{array} \right) \tag{2.2}$$

As we will see later, $\tan s_i$ can be read directly from the images. Therefore, the 3D point $\triangle \mathbf{r}$ can be reconstructed by solving Equations 2.2.

To calculate the s_i, for convenience, we assume a simple projective geometry camera model. In this case, the optical axis of the camera is perpendicular to the image plane. According to Figure 2.7, the angle of s can be derived by

$$\cos s = \frac{f^2 + \rho_0 \rho \cos \gamma}{\sqrt{f^2 + \rho_0^2} \sqrt{f^2 + \rho^2}} \tag{2.3}$$
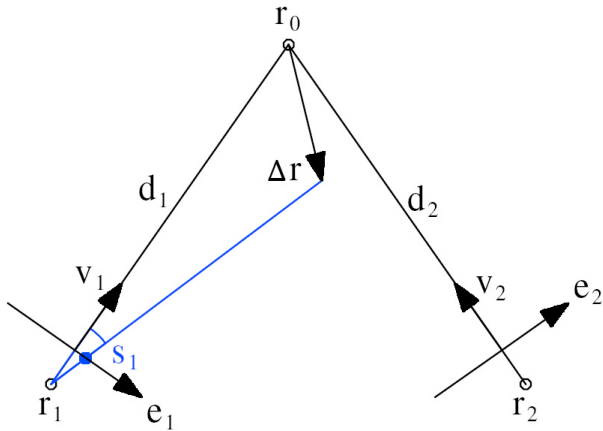
Figure 2.6: One example of how one 3D point $\triangle\mathbf{r}$ is reconstructed with the projective geometry on one epipolar plane which intersects with the epi_z axis at $\mathbf{r_0}$. $\mathbf{r_1}$ and $\mathbf{r_2}$ stand for the two observers (Inhester 2006a).
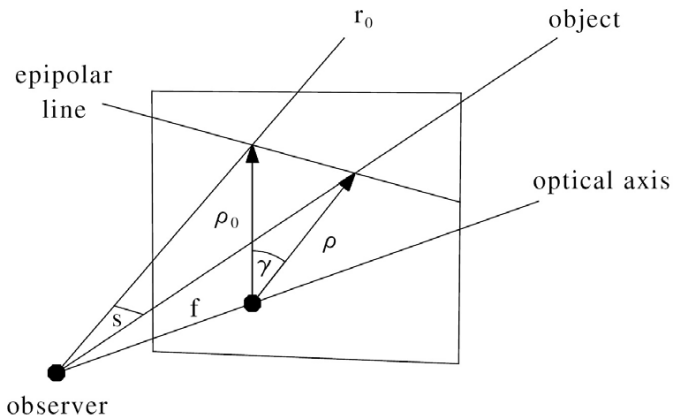
Figure 2.7: Derivation of the angle s from the image coordinates for a projective geometry camera model. The parallelogram indicates the image plane (Inhester 2006a).
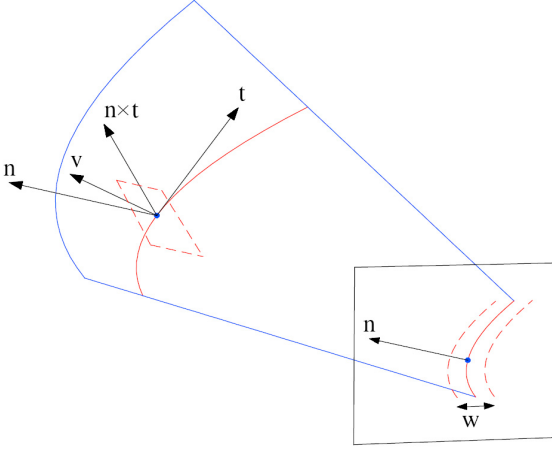
Figure 2.8: Local orthogonal coordinate system at one point along the reconstructed 3D curve indicated in red. $\mathbf{v}$ is the local view direction, $\mathbf{t}$ is the local tangent direction along the reconstructed curve. The local normal of the projection surface is $\mathbf{n} = \mathbf{t} \times \mathbf{v}/|\mathbf{t} \times \mathbf{v}|$. The three unit vectors framing the local orthogonal coordinate system are $\mathbf{n}$, $\mathbf{t}$ and $\mathbf{n} \times \mathbf{t}$. The positional uncertainty w_i at one point in two images leads to an error trapezoid indicated by the red dashed square. For clarity the projection surface of the second image is not shown here (Inhester 2006a).

where f is the camera's focal length, ρ_0 and ρ are the image distances of $\mathbf{r_0}$ and object projections from the image center, respectively, and γ is the azimuth difference. For $\rho/f \to 0$, $\rho_0/f \to 0$, Equation 2.3 can be approximated by

$$s^2 \approx \left(\frac{\rho_0}{f}\right)^2 + \left(\frac{\rho}{f}\right)^2 - 2\frac{\rho_0\rho}{f^2}\cos\gamma. \qquad (2.4)$$

For EUVI images, s is rather small, of the magnitude of 0.005 radian. The projective geometry can be simplified to the affine geometry. While for HI images, due to the much larger field-of-view, projective geometry is unavoidable.

2.2.1.2 Reconstruction uncertainty

In reality, the width of an object in one image is not infinitely narrow. It has a finite thickness due to the spatial resolution or noise. Consequently, the reconstructed 3D curve becomes a 3D tube with a trapezoidal cross section within which the 3D curve position cannot be resolved when the 2D positional uncertainty is considered. In Figure 2.8, the error trapezoid at one point along the reconstructed 3D curve is indicated by the red dashed square normal to the local tangent direction $\mathbf{t}$. The local orthogonal coordinate system at this point for one view direction is determined by $\mathbf{t}$, $\mathbf{n}$ and $\mathbf{n} \times \mathbf{t}$. We sketch the
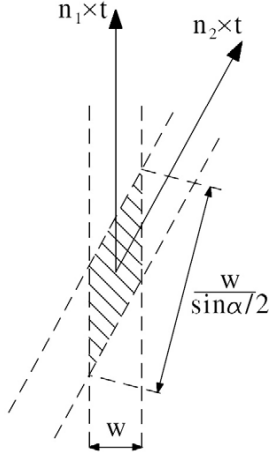
Figure 2.9: An error trapezoid in the plane normal to the 3D curve. α is the angle between $\mathbf{n_1}$ and $\mathbf{n_2}$ (Inhester 2006a).

details on the error trapezoid in Figure 2.9. The four points of the error trapezoid can be expressed as

$$\delta\mathbf{r} = \pm a_1 \mathbf{t} \times \mathbf{n_1} \pm a_2 \mathbf{t} \times \mathbf{n_2} \tag{2.5}$$

The projection of this trapezoid onto image 1 and 2 has to yield the curve width w_1 and w_2, respectively. Then, $\delta\mathbf{r} \cdot \mathbf{n_1} = w_1/2$ and $\delta\mathbf{r} \cdot \mathbf{n_2} = w_2/2$. Inserting Equation 2.5 into it, we obtain the coefficients a_1 and a_2:

$$a_1 = \frac{w_2}{2\sin\alpha} \quad \text{and} \quad a_2 = \frac{w_1}{2\sin\alpha} \tag{2.6}$$

where α is the angle between two normals of the projection surfaces $\mathbf{n_1}$ and $\mathbf{n_2}$ and is always smaller or at most equal to the spacecraft separation angle. The upper limit is reached when the loop intersects an epipolar line perpendicularly. For features parallel to epipolar lines α is zero and the reconstruction uncertainty is infinite.

2.2.2   Optically-thin emission lines and plasma diagnostics

In the outer solar atmosphere, the transition region (TR) and the corona, the most important emissions are at Ultraviolet (UV) and Extreme Ultraviolet (EUV) wavelengths. The continuum emission is generated by the thermal bremsstrahlung (free-free transition) where a free electron is scattered off an ion and escapes as a free electron. What we are more interested in is the line emission as it provides us with the temperature, density and velocity information of the plasma. Moreover, in this thesis the data we use are obtained from EUV imaging telescopes (EUVI, TRACE) and the EUV spectrograph (SUMER).

Therefore, in this subsection, we will present how to calculate the observed flux of the optically-thin emission lines formed in the TR and the corona, followed by the plasma diagnostic techniques summarized from Chapter 2 in Mariska (1992).

2.2.2.1 Optically-thin emission lines

In Chapter 2 of Aschwanden (2005b), different atomic processes are listed for the solar atmosphere. Due to the weak radiation field in the TR and the corona, radiative induced absorption and stimulated emission are rare. Thus, collisional excitation and deexcitation, as well as spontaneous radiative decay are important in establishing level populations. Considering the ionization and recombination, photo-ionization can be neglected for the same reason. The density in the TR and the corona is very low, the three-body recombination proceeds at too slow a rate to be important. Therefore, the important processes of ionization are either a direct impact ionization by an electron or the auto-ionization from two unstable excited states after the collision. For recombination, the collision induced recombination is important and can happen either radiatively or dielectronically.

Each atomic species contained in the TR or coronal plasma has many different bound energy levels. For any emission line formed by the transition from an upper level j to a lower level i, the volume emissivity in the transition is

$$\varepsilon_{ji} = h\nu_{ji}A_{ji}n_j \tag{2.7}$$

where A_{ji} is the Einstein probability coefficient of the spontaneous emission and n_j is the population at the upper level j. If we assume the emission is optically thin, then the flux observed at the Earth (or a satellite) from a volume of plasma ΔV is

$$F_{ji} = \frac{1}{4\pi R^2} \int_{\Delta V} \varepsilon_{ji}\mathrm{d}V = \frac{h\nu_{ji}A_{ji}}{4\pi R^2} \int_{\Delta V} n_j\mathrm{d}V \tag{2.8}$$

in which R is the Sun-Earth (Sun-satellite) distance. Practically, ΔV is defined by the spatial resolution of the instrument multiplied by the path length along the line-of-sight. If we express the number density of ions in the excited level i in terms of other parameters, we have

$$n_i = \frac{n_i}{n_{ion}} \frac{n_{ion}}{n_{el}} \frac{n_{el}}{n_H} \frac{n_H}{n_e} n_e \tag{2.9}$$

where $\frac{n_i}{n_{ion}}$ is the relative population of the excited level, $\frac{n_{ion}}{n_{el}}$ is the relative abundance of the ionic species, $\frac{n_{el}}{n_H} = A_{el}$ is the abundance of a element relative to hydrogen, and $\frac{n_H}{n_e}$ is the ratio of the number densities of hydrogen to electrons.

Generally, populations of electrons at each level are calculated by the statistical equilibrium equations (SEEs), $\mathrm{d}n_i/\mathrm{d}t = 0$, which are coupled with the radiative transfer equations, like the case in the photosphere where induced absorption, stimulated emission and photon-ionization are important and related to the radiation field. In the case of the TR and the corona, the background radiation is so weak that the mentioned transitions are negligible. Therefore only the SEEs are required to obtain the information of n_i. As the characteristic time of excitation and deexcitation is much shorter than the time scale of ionization and recombination, we split the SEEs by dealing with excitation and ionization separately to obtain $\frac{n_i}{n_{ion}}$ and $\frac{n_{ion}}{n_{el}}$ in Equation 2.9, respectively.

Excitation

For each level in an ion, the self-contained excitation rate equations can be written as

$$\frac{dn_i}{dt} = \sum_{j\neq i} n_j n_e C_{ji} - n_i \sum_{j\neq i} n_e C_{ij} + \sum_{j>i} n_j A_{ji} - n_i \sum_{j<i} A_{ij} = 0$$

$$n_{ion} = \sum_i n_i \qquad (2.10)$$

Here the first two terms on the right side are related to collision and the last two terms are the spontaneous emission rate from and to the level i. The latter can be obtained from the atomic physics and is independent of the plasma. Writing the collision rate term $n_i n_e C_{ij}$ in detail, we have

$$n_i n_e C_{ij} = n_i n_e \int_{v_0}^{+\infty} \sigma_{ij}(v_e) f(v_e) v_e dv_e \qquad (2.11)$$

where $\sigma_{ij}(v_e)$ is the electron collision cross section as a function of the electron speed, v_0 is the speed corresponding to the threshold of the electron kinetic energy ΔE_{ij} for the transition, and $f(v_e)$ is the electron speed distribution. Though the system deviates from the local thermal equilibrium, electron speeds can still be approximated by the Maxwellian distribution because in the TR and the corona, in the life time of electrons the elastic collisions among electrons are sufficient to establish a thermal equilibrium among them. By applying the Maxwellian distribution of the electron speed and introducing the collision strength $\Omega_{ij}(E)$ as a function of the electron kinetic energy E, we obtain

$$C_{ij} = \frac{8.63 \times 10^{-6}}{g_i k T_e^{3/2}} \int_{\Delta E_{ij}}^{+\infty} \Omega_{ij}(E) \exp\left(\frac{-E}{kT_e}\right) dE. \qquad (2.12)$$

where g_i is the statistical weight of level i. Collisional deexcitation rates are obtained using the principle of detailed balance in thermodynamic equilibrium, $n_i n_e C_{ij} = n_j n_e C_{ji}$. By applying the Boltzmann equation, we have

$$C_{ji} = \frac{g_i}{g_j} C_{ij} \exp\left(\frac{\Delta E_{ij}}{kT_e}\right) \qquad (2.13)$$

With the calculated collision coefficient C_{ij} and C_{ji} depending on T and the Einstein probability coefficient A_{ij} independent of the plasma property, we can solve the excitation rate equations, the population at each level n_i are consequently derived.

Ionization

For any given ion z of an element of nuclear charge Z, the self-contained equations of ionization balance are

$$\frac{dn_z}{dt} = n_e(n_{z-1}q_{z-1} + n_{z+1}\alpha_{z+1}) - n_e n_z(q_z + \alpha_z) = 0$$

$$n_{el} = \sum_{z=0}^{Z} n_z. \qquad (2.14)$$

The first term on the right is the rate at which ion n_z is formed by ionization from ion $z-1$ and recombination from ion $z+1$, the second term is the rate at which ion n_z is destroyed by the ionization to ion $z+1$ and the recombination to ion $z-1$. The calculations and experimental measurements of ionization and recombination rate coefficients are really scattered throughout the fields of astrophysics, plasma physics and atomic physics and out of the scope of this thesis, for the references see Mariska (1992). In some cases when the time scales of ionization and recombination are longer than the time scales of plasma evolution, the ionization balance is broken ($\frac{dn_z}{dt} \neq 0$). The equations in 2.14 have to be solved together with an atmospheric model including the information of T, n_e and v. While in some other simpler cases, we often reduce the ionization balance to ionization equilibrium where for each ion z,

$$n_z q_z = n_{z+1} \alpha_{z+1}. \tag{2.15}$$

After obtaining all the coefficients, the relative abundance of the ionic species $\frac{n_{ion}}{n_{el}}$ can be calculated accordingly.

Contribution functions

Generally, in Equation 2.9 the element abundance relative to hydrogen A_{el} and the ratio of the number densities of hydrogen to electrons $\frac{n_H}{n_e}$ can be obtained additionally from other approaches. Here we define the frequently used contribution function in units of erg cm^3 s^{-1} as

$$G(T_e, \lambda_{ij}, n_e) = h\nu_{ji} \frac{A_{ji}}{n_e} \frac{n_i}{n_{ion}} \frac{n_{ion}}{n_{el}} \tag{2.16}$$

in which all the atomic parameters related to n_i and n_{ion} are included.

By using the contribution function, the observed flux can be written accordingly in the form of

$$F_{ji} = \frac{0.83 A_{el}}{4\pi R^2} \int_{\Delta V} G(T_e, \lambda_{ij}, n_e) n_e^2 dV \tag{2.17}$$

if we assume $\frac{n_H}{n_e} = 0.83$. In this form the line flux is easily related to differential emission measure (DEM) defined as

$$\frac{dEM(T_e)}{dT_e} = n_e^2 \frac{dV}{dT_e} \tag{2.18}$$

which is a measure of the amount of plasma in a certain volume that contributes to the emission in the temperature range T_e to $T_e + dT_e$. From the observed flux and the contribution functions calculated with the code CHIANTI, we can obtain a best fit DEM distribution. Or the other way round, from simulations we get temperature, density and synthesize the flux of a particular line we are interested in. By the comparison with the observed flux, the free parameters in simulations can be investigated and further physical implications will be obtained.

2.2.2.2   Plasma diagnostics

In the following, the electron density and temperature diagnostics using emission line ratios from SUMER observations are introduced. It is important to remember that any such line ratio provides an average value along the line of sight.

For the plume study from SUMER observations, we analysed the density-sensitive line pair Si VIII at 1440 Å and 1446 Å and the temperature sensitive line pair Mg IX at 706 Å and 750 Å. Both the Si VIII and Mg IX lines are formed at temperatures around 1 MK which is proper for plume observations (Wilhelm 2006). If we consider two spectral lines, one comes from the transition $u \rightarrow l$, the other from $j \rightarrow i$, the ratio of these two lines is defined by

$$\frac{F_{ul}}{F_{ji}} = \frac{n_u A_{ul} h\nu_{ul}}{n_j A_{ji} h\nu_{ji}} \tag{2.19}$$

The only term in this equation related to the electron temperature and density is n_u/n_j. It can be computed by solving the statistical equilibrium equations (SEEs). Because T_e and n_e enter SEEs via collisional terms, finally n_u/n_j will be a function of T_e or n_e depending on the lines we choose. Here we have two simple cases showing how to derive the electron temperature and density with the line-ratio method taken from Mariska (1992).

Temperature diagnostics

Suppose we have an ion with two upper excited levels 2 and 3, and the ground level 1. Two emission lines are both formed by collisions to the excited levels and spontaneous decays to the ground level. Then the ratio of fluxes from these two lines is given by

$$\frac{F_{31}}{F_{21}} = \frac{n_3 A_{31} h\nu_{31}}{n_2 A_{21} h\nu_{21}} = \frac{n_1 n_e C_{13} h\nu_{31}}{n_1 n_e C_{12} h\nu_{21}} \tag{2.20}$$

Using the collision rate coefficient in Equation 2.12 and assuming the collision strengths are energy independent, we have

$$\frac{F_{31}}{F_{21}} = \frac{h\nu_{13}\Omega_{13}}{h\nu_{12}\Omega_{12}} \exp\left(\frac{h\nu_{12} - h\nu_{13}}{kT_e}\right) \tag{2.21}$$

If $(h\nu_{12} - h\nu_{13})/kT_e \geq 1$, this flux ratio will be temperature sensitive.

Density diagnostics

As an illustration of obtaining electron densities using line ratios, we consider a simple three-level ion. Level 1 is ground state and level 3 is metastable. The level 2 to 1 transition forms an allowed line and the collision deexcitation is negligible comparing to the spontaneous radiative decay. The level 3 to 1 transition forms a forbidden line and level 3 is populated by collisions and depopulated by both collisions and spontaneous radiative decays. If we ignore the collisional excitation from level 2 to 3, the SEEs for level 2 and 3 can be written as

$$n_2 A_{21} = n_1 n_e C_{12} + n_3 (A_{32} + n_e C_{32}) \tag{2.22}$$

and

$$n_3 (A_{32} + A_{31} + n_e C_{32} + n_e C_{31}) = n_1 n_e C_{13}. \tag{2.23}$$
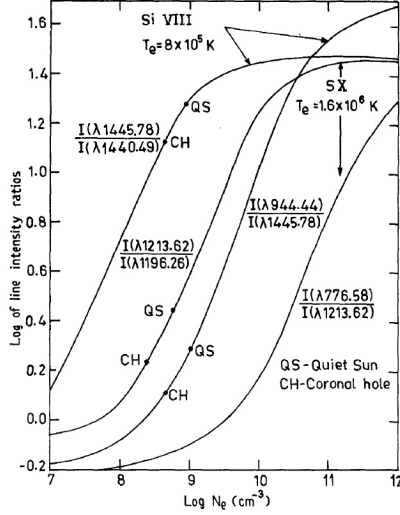
Figure 2.10: Density dependence of Si VIII and S X line ratios (adapted from Dwivedi (1991)).

The flux ratio R of the forbidden line 3 to 1 and the allowed line 2 to 1 is obtained by combining these two equations and using $A_{32} \ll A_{31}$,

$$R = \frac{n_3 A_{31} h\nu_{31}}{n_2 A_{21} h\nu_{21}} = \frac{h\nu_{31}}{h\nu_{21}} \frac{A_{31}}{\frac{C_{12}+C_{13}}{C_{13}} n_e C_{32} + \frac{C_{12}}{C_{13}} (A_{31} + n_e C_{31})}. \tag{2.24}$$

When n_e is low, the collision related terms C_{31} and C_{32} can be neglected. The levels 2 and 3 are populated by the collision excitation and depopulated by the spontaneous decay. The flux ratio simplifies to

$$R \propto \frac{C_{13}}{C_{12}}. \tag{2.25}$$

When n_e is larger enough that $A < n_e C$, We have

$$R \propto \frac{A_{31}}{n_e \left(\frac{C_{12}+C_{13}}{C_{13}} C_{32} + \frac{C_{12}}{C_{13}} C_{31}\right)}. \tag{2.26}$$

This ratio is now inversely proportional to n_e. If R can be obtained from the observations, n_e can then be derived accordingly.

We have shown two simplified cases above, for real line-ratio calculations the full set of SEEs need to be solved. In Figure 2.10 and Figure 2.11, we present the computed line ratios as a function of T_e or n_e for Si VIII and Mg IX. Both lines are formed at coronal
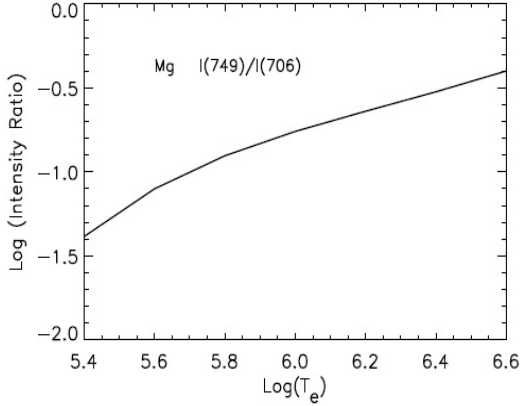
Figure 2.11: Intensity line ratios of Mg IX at 706 Å and 750 Å as a function of electron temperature (adapted from Raymond and Wood (2000)).

temperatures around 1 MK. Once we have the line ratios from observations, the corresponding electron densities and temperatures could be calculated from these two figures. Detailed plasma density and temperature measurements in coronal holes can be found in Wilhelm (2006).

More plasma parameters can be deduced from the spectral line profiles. The observed Doppler shifts of the emission lines are used to measure the LOS bulk velocities according to

$$v \simeq c\frac{\nu - \nu_0}{\nu_0},\tag{2.27}$$

where ν_0 is the rest frequency of the photon and c is the light speed.

Furthermore, the observed line width gives us an upper limit of the ion temperature as it should theoretically vary as

$$\Delta \nu_D = \frac{\nu_0}{c}\sqrt{\frac{2kT}{m} + v_u^2 + \sigma_I^2}.\tag{2.28}$$

Here v_u is the most probable non-thermal turbulent speed and σ_I is the equivalent Doppler broadening contributed by instrumental effects.

2.2.3 Magnetic field models

As introduced in Chapter 1, both coronal loops and polar plumes outline the magnetic field lines in the corona. In this section the related magnetic field models are introduced for the cases of global Sun and active regions.

Dipole field
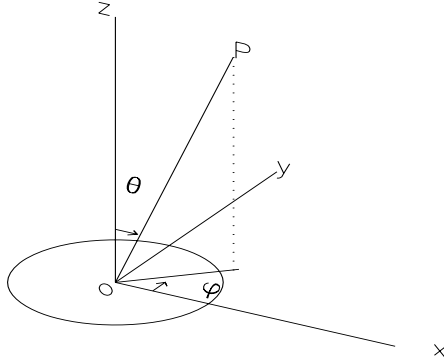
Figure 2.12: The circular current system lying on the *xoy* plane and the definition of θ and φ related to the spherical coordinate system.

A dipole field is the lowest order approximation of the magnetic field for the global Sun. It is generated at large distances by localized current distributions. As an illustration of the derivation of the dipole magnetic field we consider a circular current loop of radius a centered at the origin and lying in the *xoy* plane (Figure 2.12). In a spherical coordinate system, assuming a current of I the current density $\mathbf{j}(\mathbf{r}')$ could be expressed as:

$$\mathbf{j}(\mathbf{r}') = j_{\varphi'}\mathbf{e}_{\varphi'} = (I/a)\delta(r' - a)\delta(\theta' - \pi/2)\mathbf{e}_{\varphi'}. \tag{2.29}$$

The vector potential $\mathbf{A}(\mathbf{r})$ generated can be defined as

$$\mathbf{A}(\mathbf{r}) = \frac{\mu}{4\pi} \iiint \frac{\mathbf{j}(\mathbf{r}')}{|\mathbf{r} - \mathbf{r}'|}d\tau'. \tag{2.30}$$

This definition satisfies $\mathbf{B} = \nabla \times \mathbf{A}$ and $\nabla \cdot \mathbf{A} = 0$. Inserting Equation 2.29 into Equation 2.30, we come to

$$\begin{aligned} \mathbf{A}(\mathbf{r}) &= \frac{I\mu}{4\pi a} \int_0^{+\infty} \delta(r' - a)r'^2 dr' \int_0^{\pi} \delta(\theta' - \pi/2)\sin\theta' d\theta' \int_0^{2\pi} \frac{\mathbf{e}_{\varphi'}}{|\mathbf{r} - \mathbf{r}'|}d\varphi' \\ &= \frac{I\mu a}{4\pi} \int_0^{2\pi} \frac{\mathbf{e}_{\varphi'}}{|\mathbf{r} - a\mathbf{e}_{\mathbf{r}'}|}d\varphi'. \end{aligned} \tag{2.31}$$

Since the geometry is cylindrical symmetric, $\mathbf{A}(\mathbf{r})$ only has the component in direction of $\mathbf{e}_{\varphi}$, therefore $\mathbf{A}(\mathbf{r}) = A_{\varphi}\mathbf{e}_{\varphi}$ in which

$$\begin{aligned} A_{\varphi}(r, \theta, \varphi) &= \mathbf{A}(\mathbf{r}) \cdot \mathbf{e}_{\varphi} \\ &= \frac{I\mu a}{4\pi} \int_0^{2\pi} \frac{\mathbf{e}_{\varphi'} \cdot \mathbf{e}_{\varphi}}{|\mathbf{r} - a\mathbf{e}_{\mathbf{r}'}|}d\varphi'. \end{aligned} \tag{2.32}$$

37

Again due to the cylindrical symmetry, $A_\varphi(r, \theta, \varphi) = A_\varphi(r, \theta)$. For simplicity of calculation, we choose $\varphi = 0$, thus (Jackson 1975)

$$
\begin{aligned}
A_\varphi(r, \theta) &= \frac{I\mu a}{4\pi} \int_0^{2\pi} \frac{\cos \varphi'}{(a^2 + r^2 - 2ar \sin \theta \cos \varphi')^{1/2}} d\varphi' \\
&= \frac{I\mu a}{\pi \sqrt{a^2 + r^2 + 2ar \sin \theta}} \left[\frac{(2 - k^2)K(k) - 2E(k)}{k^2} \right],
\end{aligned}
\tag{2.33}
$$

where K and E are elliptic integrals and

$$
k^2 = \frac{4ar \sin \theta}{a^2 + r^2 + 2ar \sin \theta}.
\tag{2.34}
$$

If we consider the case that $k \ll 1$, then the square bracket in Equation 2.33 reduces to $\pi k^2 / 16$ (Jackson 1975). Accordingly the vector potential becomes

$$
A_\varphi(r, \theta) = \frac{\mu I a^2}{4} \cdot \frac{r \sin \theta}{(a^2 + r^2 + 2ar \sin \theta)^{3/2}}
\tag{2.35}
$$

The three components of magnetic field can finally be calculated by using $\mathbf{B} = \nabla \times \mathbf{A}$ in the spherical coordinate system, the results are shown in the following:

$$
\begin{aligned}
B_r(r, \theta) &= \frac{1}{r \sin \theta} \frac{\partial}{\partial \theta} (\sin \theta A_\varphi) \\
&= \frac{\mu I a^2}{4} \cos \theta \frac{2a^2 + 2r^2 + ar \sin \theta}{(a^2 + r^2 + 2ar \sin \theta)^{5/2}}
\end{aligned}
\tag{2.36}
$$

$$
\begin{aligned}
B_\theta(r, \theta) &= -\frac{1}{r} \frac{\partial}{\partial r} (r A_\varphi) \\
&= \frac{\mu I a^2}{4} \sin \theta \frac{2a^2 + 2r^2 + ar \sin \theta}{(a^2 + r^2 + 2ar \sin \theta)^{5/2}}
\end{aligned}
\tag{2.37}
$$

$$
B_\varphi(r, \theta) = 0.
\tag{2.38}
$$

For the magnetic field far from the current loop, that is, $a \ll r$, we have

$$
B_r = \frac{\mu I a^2}{4} \cos \theta \frac{2}{r^3}
\tag{2.39}
$$

$$
B_\theta = \frac{\mu I a^2}{4} \sin \theta \frac{1}{r^3}
\tag{2.40}
$$

Taking the example of our Sun and assuming the circular current loop lying in the solar equatorial plane, we can derive a relation between the latitude λ and the magnetic inclination i defined as the angle between $\mathbf{B}$ and $\mathbf{e}_\theta$ (Figure 2.13). If we divide Equation 2.39 by Equation 2.40, we obtain

$$
\tan i = \frac{B_r}{B_\theta} = \frac{2}{\tan \theta} = 2 \tan \lambda
\tag{2.41}
$$

This relationship will be used to test how well a dipole field approximates the magnetic field of the Sun at the polar caps by comparing it with the inclination of the reconstructed 3D polar plumes in Chapter 5.
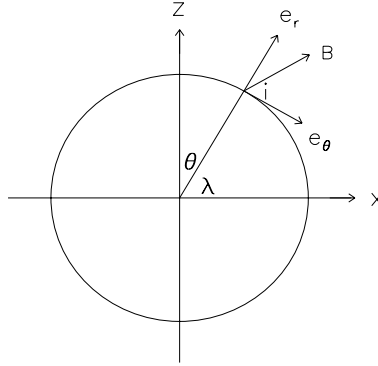
Figure 2.13: A cross section of the Sun with the indicated dipole field direction at a given point. **B** only has components in $\mathbf{e_r}$ and $\mathbf{e}_\theta$. i is the magnetic inclination.

From Equation 2.35, we can demonstrate that in the case of $a \ll r$, the vector potential can be written as

$$A_\varphi(r, \theta) = \frac{\mu IS}{4\pi} \frac{\sin\theta}{r^2}, \tag{2.42}$$

where $S = \pi a^2$ is the area of the circular current loop. If we rewrite **A** in the form of a vector, then

$$\mathbf{A} = \frac{\mu}{4\pi} \frac{\mathbf{m} \times \mathbf{e_r}}{r^2}, \tag{2.43}$$

in which $\mathbf{m} = IS\,\mathbf{n}$ is the magnetic moment with **n** being the unit vector of the surface s. Accordingly, following $\mathbf{B} = \nabla \times \mathbf{A}$ we come to

$$\mathbf{B} = -\frac{\mu}{4\pi} \nabla \left(\frac{\mathbf{m} \cdot \mathbf{e_r}}{r^2} \right). \tag{2.44}$$

That is to say, the magnetic field far away from the circular current loop is a potential field which is a specific case of the force-free magnetic field described below.

Force-free magnetic field

In magneto-statics, a magnetic field is said to be force-free when the Lorentz force is zero, that is,

$$\mathbf{j} \times \mathbf{B} = 0. \tag{2.45}$$

Combining with the Maxwell equation $\nabla \times \mathbf{B} = \mu\mathbf{j}$, we can obtain the force-free magnetic field condition entirely expressed by **B**,

$$(\nabla \times \mathbf{B}) \times \mathbf{B} = 0. \tag{2.46}$$

Therefore,

$$\nabla \times \mathbf{B} = \mu \mathbf{j} = \alpha(\mathbf{r})\mathbf{B}, \tag{2.47}$$

where $\alpha(\mathbf{r})$ is a scalar function of position. If $\alpha(\mathbf{r})$ is simply a constant, the magnetic field satisfying Equation 2.47 is called the linear force-free magnetic field. For the case of varying α, the magnetic field is a nonlinear force-free field. Specifically when $\alpha(\mathbf{r})$ equals zero, there is no current flowing along the magnetic field lines and this case corresponds to the potential case. In this thesis we will concentrate on the linear force-free field. It is used in Chapter 4 to identify the loop correspondence in active regions. And it has been proved that the linear force-free field is sufficient for this purpose (Wiegelmann and Inhester 2006).

Based on the Zeeman splitting effect, the magnetic field in the photosphere can be measured. However, in the corona the low plasma density, high temperature and weak magnetic field strength make measurements of the Zeeman splitting very difficult. An alternative way of estimating the magnetic field in the corona is to extrapolate it from photospheric measurement, such as MDI observations. The extrapolation method we introduce here is similar to the one described in Seehafer (1978).

By taking the curl on both sides of Equation 2.47 and considering $\alpha(\mathbf{r})$ as a constant, we derive the Helmholtz equation

$$\nabla^2 \mathbf{B} + \alpha^2 \mathbf{B} = 0. \tag{2.48}$$

We first consider the B_z component. It is the solution of the boundary value problem in the domain $0 \leq x \leq L_x,\ 0 \leq y \leq L_y,\ 0 \leq z < +\infty$. Assuming B_z vanish at the vertical planes $x = 0$, $x = L_x$, $y = 0$, $y = L_y$, the boundary value problem can be formulated as below:

$$\begin{aligned}
\nabla^2 B_z + \alpha^2 B_z &= 0 \\
B_z(0, y, z) = 0 &\quad,\quad B_z(L_x, y, z) = 0 \\
B_z(x, 0, z) = 0 &\quad,\quad B_z(x, L_y, z) = 0 \\
B_z(x, y, 0) = B_{obs} &\quad,\quad B_z(x, y, +\infty) = 0.
\end{aligned} \tag{2.49}$$

where B_{obs} is the measured LOS field in the photosphere.

We use the Fourier Transform to solve the boundary problems. Taking Fourier Transform of $B_z(\mathbf{r})$, we have

$$\widehat{B_z}(\mathbf{k}) = \iiint B_z(\mathbf{r}) e^{-i\mathbf{k}\cdot\mathbf{r}} d\mathbf{r}^3 \tag{2.50}$$

According to the differentiation property of the Fourier Transform,

$$\mathbf{FT}(\nabla^2 B_z(\mathbf{r})) = (i\mathbf{k})^2\, \mathbf{FT}(B_z(\mathbf{r})) \tag{2.51}$$

If we take the Fourier Transform on both sides of the first equation in (2.49), we have

$$(-k^2 + \alpha^2)\widehat{B_z}(\mathbf{k}) = 0, \tag{2.52}$$

then the dispersion equation is derived as

$$k_x^2 + k_y^2 + k_z^2 = \alpha^2. \tag{2.53}$$

The solution of $B_z(\mathbf{r})$ can be obtained by the inverse Fourier Transform as

$$B_z(\mathbf{r}) = \frac{1}{(\sqrt{2\pi})^3} \iiint \widehat{B_z}(\mathbf{k}) e^{i\mathbf{k}\cdot\mathbf{r}} d\mathbf{k}^3. \tag{2.54}$$

We separate $B_z(\mathbf{r})$ as $B_z(\mathbf{r}) = T(x,y)Z(z)$. Because of the zero values of B_z on the four lateral boundaries at $x = 0$, $x = L_x$, $y = 0$, $y = L_y$, we can obtain the solution $T_{mn}(x,y)$ for one combination of m and n

$$T_{mn}(x,y) = a_{mn} \sin(k_{xm}x) \sin(k_{yn}y) \tag{2.55}$$

where

$$k_{xm} = \frac{m\pi}{L_x} \quad \text{and} \quad k_{yn} = \frac{n\pi}{L_y}. \tag{2.56}$$

According to the dispersion relation

$$k_{zmn}^2 = \alpha^2 - (k_{xm}^2 + k_{yn}^2) = \alpha^2 - \left(\left(\frac{m\pi}{L_x}\right)^2 + \left(\frac{n\pi}{L_y}\right)^2 \right). \tag{2.57}$$

If we want to have a solution of $Z_{mn}(z)$ decaying from the bottom, k_{zmn} should be imaginary. Therefore, $|\alpha| < \pi \sqrt{\frac{1}{L_x^2} + \frac{1}{L_y^2}}$ has to be satisfied. Assuming that the source of the magnetic field is mainly from the bottom boundary, this limited value of α is necessary, otherwise the magnetic field will start oscillating in the vertical direction. Considering the boundary condition at the top boundary, we obtain

$$Z_{mn}(z) = b_{mn} e^{ik_{amn}z} \quad \text{and} \quad k_{zmn} = i\sqrt{\left(\frac{m\pi}{L_x}\right)^2 + \left(\frac{n\pi}{L_y}\right)^2 - \alpha^2} \tag{2.58}$$

Combining Equations 2.55 and 2.58 and denoting $r_{mn} = -ik_{zmn}$ we arrive

$$B_{zmn}(\mathbf{r}) = C_{mn} e^{-r_{mn}z} \sin\left(\frac{m\pi x}{L_x}\right) \sin\left(\frac{n\pi y}{L_y}\right) \tag{2.59}$$

and the complete solution considering all the combinations of m and n is

$$B_z(x,y,z) = \sum_{m,n=1}^{+\infty} C_{mn} e^{-r_{mn}z} \sin\left(\frac{m\pi x}{L_x}\right) \sin\left(\frac{n\pi y}{L_y}\right). \tag{2.60}$$

where the coefficient C_{mn} is determined by the boundary conditions at the bottom, that is, $B_z(x,y,0)$ which can be obtained by the photospheric magnetograph like MDI. When $z = 0$,

$$B_z(x,y,0) = \sum_{m,n=1}^{+\infty} C_{mn} \sin\left(\frac{m\pi x}{L_x}\right) \sin\left(\frac{n\pi y}{L_y}\right) \tag{2.61}$$

By multiplying $\sin\left(\frac{k\pi x}{L_x}\right) \sin\left(\frac{l\pi y}{L_y}\right)$ on both sides of Equation 2.61 and integrating in the domain from 0 to L_x and from 0 to L_y, we obtain the Fourier coefficient C_{mn} according to the orthogonality of the trigonometric functions,

$$C_{mn} = \frac{4}{L_x L_y} \int_0^{L_x} \int_0^{L_y} B_z(x,y,0) \sin\left(\frac{m\pi x}{L_x}\right) \sin\left(\frac{n\pi y}{L_y}\right) dxdy. \tag{2.62}$$

As we know MDI magnetograms always give us the magnetic field directions along the line-of-sight, while here $B_z(x, y, 0)$ is the vertical component. To make them consistent we prefer to choose active regions close to the disk center.

After deriving the B_z component, we are going to obtain the other two components B_x and B_y by decompositing **B** into toroidal and poloidal fields as Seehafer (1978)

$$\mathbf{B} = \alpha \mathbf{r} \times \nabla P + \nabla \times (\mathbf{r} \times \nabla P), \quad \mathbf{r} = (0, 0, 1)^T \tag{2.63}$$

Then the three components of **B** are

$$B_x = -\frac{\partial^2 P}{\partial x \partial z} - \alpha \frac{\partial P}{\partial y} \tag{2.64}$$

$$B_y = -\frac{\partial^2 P}{\partial y \partial z} + \alpha \frac{\partial P}{\partial x} \tag{2.65}$$

$$B_z = \frac{\partial^2 P}{\partial^2 x} + \frac{\partial^2 P}{\partial^2 y} \tag{2.66}$$

From Equation 2.66 it is obvious that the solution to $P(x, y, z)$ for a given combination of m and n has the form

$$P_{mn}(x, y, z) = k_{mn} e^{-r_{mn}z} \sin\left(\frac{m\pi x}{L_x}\right) \sin\left(\frac{n\pi y}{L_y}\right). \tag{2.67}$$

Inserting it into Equation 2.66 and assuming $\lambda_{mn} = r_{mn}^2 + \alpha^2$, we find $k_{mn} = -C_{mn}/\lambda_{mn}$. It leads to

$$P_{mn} = -\frac{C_{mn}}{\lambda_{mn}} e^{-r_{mn}z} \sin\left(\frac{m\pi x}{L_x}\right) \sin\left(\frac{n\pi y}{L_y}\right). \tag{2.68}$$

According to Equations 2.64 and 2.65, we obtain

$$
\begin{aligned}
B_{xmn} &= \frac{C_{mn}}{\lambda_{mn}} e^{-r_{mn}z} \left\{ \alpha \frac{\pi n}{L_y} \sin\left(\frac{m\pi x}{L_x}\right) \cos\left(\frac{n\pi y}{L_y}\right) \right. \\
&\quad \left. - r_{mn} \frac{\pi m}{L_x} \cos\left(\frac{m\pi x}{L_x}\right) \sin\left(\frac{n\pi y}{L_y}\right) \right\}, \\
B_{ymn} &= -\frac{C_{mn}}{\lambda_{mn}} e^{-r_{mn}z} \left\{ \alpha \frac{m\pi x}{L_x} \cos\left(\frac{m\pi x}{L_x}\right) \sin\left(\frac{n\pi y}{L_y}\right) \right. \\
&\quad \left. + r_{mn} \frac{n\pi y}{L_y} \sin\left(\frac{m\pi x}{L_x}\right) \cos\left(\frac{n\pi y}{L_y}\right) \right\}.
\end{aligned}
\tag{2.69}
$$

Finally the complete solutions to the three components of magnetic field **B** for all the combinations of m and n can be written as

$$
\begin{aligned}
B_x &= \sum_{m,n=1}^{+\infty} \frac{C_{mn}}{\lambda_{mn}} e^{-r_{mn}z} \left\{ \alpha \frac{\pi n}{L_y} \sin\left(\frac{m\pi x}{L_x}\right) \cos\left(\frac{n\pi y}{L_y}\right) \right. \\
&\quad \left. - r_{mn} \frac{\pi m}{L_x} \cos\left(\frac{m\pi x}{L_x}\right) \sin\left(\frac{n\pi y}{L_y}\right) \right\},
\end{aligned}
\tag{2.70}
$$

$$B_y = -\sum_{m,n=1}^{+\infty} \frac{C_{mn}}{\lambda_{mn}} e^{-r_{mn}z} \left\{ \alpha \frac{m\pi x}{L_x} \cos\left(\frac{m\pi x}{L_x}\right) \sin\left(\frac{n\pi y}{L_y}\right) \right.$$

$$\left. + r_{mn} \frac{n\pi y}{L_y} \sin\left(\frac{m\pi x}{L_x}\right) \cos\left(\frac{n\pi y}{L_y}\right) \right\}, \tag{2.71}$$

$$B_z = \sum_{m,n=1}^{+\infty} C_{mn} \sin\left(\frac{m\pi x}{L_x}\right) \sin\left(\frac{n\pi y}{L_y}\right). \tag{2.72}$$

The advantage of linear force-free field extrapolations is its simplicity in mathematics and it requires only the LOS photospheric magnetic field measurements as input. The free parameter α can be determined by comparing the extrapolated field lines with the observed coronal loops from one viewpoint (Wiegelmann et al. 2005a) or two viewpoints (Feng et al. 2007a). However, linear force-free field does not make sense on a large scale. It can therefore only yield a local approximation. There are many papers, e.g. Wiegelmann et al. (2005b), showing that in many cases linear force-free or potential field is insufficient. Moreover, the constant α has the disadvantage that all field lines carry a current, even the open field lines which does not make sense. In this thesis, the extrapolated linear force-free field lines are used only for matching loop pairs in two EUVI images. As revealed by Wiegelmann et al. (2005b) for active regions the nonlinear force-free field is more suitable to describe the magnetic properties. However, to compute the nonlinear force-free field, we need vector magnetograms as the input and on the other hand, it is more expensive to compute.

3 Coronal Loop detections from EUV images

This chapter is mainly based on the papers by Inhester et al. (2008) and Inhester (2006b) with more extended explanations of the ridge detection method. We extract bright loop structures from solar EUV images which are elongated ridge-like maxima in terms of image intensities. The method is a derivative based method and can be separated into three steps. First the location and orientation of a point on the ridge is detected according to the first and second derivatives of the image intensity at that point, then detected ridge points are connected to chains, finally these chains are fitted by smooth curves. Unfortunately, image processing cannot distinguish between structures resulting from coronal loops, moss and some other bright features. Therefore we append in the end a user interactive tool to eliminate unwanted structures or split and merge some apparent loop structures. This ridge detection method can be applied to the EUV images observed by EIT/SOHO, TRACE, EUVI/SECCHI and in the future by AIA/SDO (Solar Dynamic Observatory) which will provide huge number of images, a motivation of the research on the automated feature detection. A review on different coronal loop tracing methods can be found in Aschwanden et al. (2008a).

3.1 Ridge location and orientation

Loop structures are elongated ridge-like intensity maxima, if we plot the image intensity as a surface $I(x, y)$ in the coordinate system of (x, y, I) where (x, y) is the 2D image coordinate and I is the intensity. To identify the local maxima, we need to calculate the spatial derivatives of the image intensity which are strongly affected by image noise.

We denote by $\mathbf{i} \in \mathbb{I}^2$ the integer coordinates of the center of each pixel in the image and by $\mathbf{x} \in \mathbb{R}^2$ the 2D continuous coordinates around the pixel center $\mathbf{x} = \mathbf{i}$. If the image intensity varies sufficiently smoothly, the intensity $I(\mathbf{x})$ in the neighbourhood of $\mathbf{i}$ can be well approximated by the Taylor expansion at the pixel center $\mathbf{i}$, that is (for details see Appendix A),

$$I(\mathbf{x}) \simeq \tilde{I}(\mathbf{x}) = I(\mathbf{i}) + \mathbf{g}^T (\mathbf{x} - \mathbf{i}) + \frac{1}{2}(\mathbf{x} - \mathbf{i})^T \mathbf{H} (\mathbf{x} - \mathbf{i}). \tag{3.1}$$

If we diagonalize the second derivative term $\mathbf{H}$ by means of

$$\mathbf{U^T H U} = diag(h_\perp, h_\parallel), \tag{3.2}$$

where matrix $\mathbf{U} = (\mathbf{u}_\perp, \mathbf{u}_\parallel)$ is composed of two eigenvectors of $\mathbf{H}$, and $h_\perp$ and $h_\parallel$ are the corresponding eigenvalues which represent the principal directions and principal second

45

derivatives on the local surface. Ordering $h_\perp$ and $h_\parallel$ so that $h_\perp < h_\parallel$, a point on the ridge is then defined in differential geometry by the criteria in the following (Appendix B):

$$\mathbf{u}_\perp^T \nabla I = \mathbf{u}_\perp^T \mathbf{g} = 0 \qquad (3.3)$$

$$(\mathbf{u}_\perp^T \nabla)^2 I = h_\perp < 0 \qquad (3.4)$$

$$|(\mathbf{u}_\perp^T \nabla)^2 I| = |h_\perp| \gg |h_\parallel| = |(\mathbf{u}_\parallel^T \nabla)^2 I|. \qquad (3.5)$$

The latter two inequalities are assumed to also hold in the neighbourhood of the ridge and are used to find out whether a pixel center $\mathbf{i}$ is close to a ridge or not. To estimate the Taylor coefficients $\mathbf{g}$ and $\mathbf{H}$ we will introduce two methods described below.

3.1.1 Taylor coefficients via linear least square fitting

The first method to obtain the Taylor coefficients is based on a local fit of $\tilde{I}(\mathbf{x})$ from Equation 3.1 to $I(\mathbf{x})$ within a pixel box of $(2m + 1) \times (2m + 1)$ centered around the cell center $\mathbf{i}$:

$$(\mathbf{g}, \mathbf{H})(\mathbf{i}) = \operatorname{argmin} \sum_{\mathbf{j}-\mathbf{i}\in[-m,m]\times[-m,m]} w(\mathbf{i} - \mathbf{j})(\tilde{I}(\mathbf{j}) - I(\mathbf{j}))^2 \qquad (3.6)$$

where w is a weight function in the pixel box separable in their x and y dependence and can be chosen as triangle, cosine and cosine^2 tapers .

Define $f(g_x, g_y, H_{xx}, H_{xy}, H_{yy}) = \sum_{\mathbf{j}-\mathbf{i}\in[-m,m]\times[-m,m]} w(\mathbf{i} - \mathbf{j})(\tilde{I}(\mathbf{j}) - I(\mathbf{j}))^2$, then $\mathbf{g}$ and $\mathbf{H}$ at f_{min} are derived by solving the equations (Bjoerck 1996) :

$$\frac{\partial f}{\partial g_x} = 0, \frac{\partial f}{\partial g_y} = 0, \frac{\partial f}{\partial H_{xx}} = 0, \frac{\partial f}{\partial H_{xy}} = 0 \text{ and } \frac{\partial f}{\partial H_{yy}} = 0.$$

3.1.2 Taylor expansions of a Gaussian filtered image

As we said before the spatial derivatives are strongly affected by image noise, to reduce the noise influence the second method is to calculate the Taylor coefficients from a filtered image instead of the original one:

$$\bar{I}(\mathbf{x}) = \sum_{\mathbf{j}} w_d(\mathbf{x} - \mathbf{j})I(\mathbf{j}) \qquad (3.7)$$

Here the window function w_d is a normalized Gaussian of width d and the distant pixels where w is small are omitted. The summation in Equation 3.7 is therefore carried out over a limited box of $(2m+1) \times (2m+1)$ where m depends on d in such a way that $w(m)m^2 < \epsilon$ for a small ϵ, like $\epsilon = 10^{-2}$.

To normalize the window function we introduce a coefficient c_0

$$w_d(\mathbf{x}) = w_d(x, y) = c_0 e^{-\left(\frac{\mathbf{x}}{d}\right)^2} = \sqrt{c_0} e^{-\left(\frac{x}{d}\right)^2} \sqrt{c_0} e^{-\left(\frac{y}{d}\right)^2}. \qquad (3.8)$$

It can be found from

$$1 = \sum_{\mathbf{j}} w_d(\mathbf{j}) = c_0 \left(\sum_{j=-m}^{m} e^{-\left(\frac{j}{d}\right)^2} \right)^2 \qquad (3.9)$$

hence

$$c_0^{-1/2} = \sum_{j=-m}^{m} e^{-\left(\frac{j}{d}\right)^2} \rightarrow \sqrt{\pi}d \quad \text{for large } d \ll m \rightarrow \infty \tag{3.10}$$

The Taylor coefficients $\mathbf{g}$ and $\mathbf{H}$ can then be calculated explicitly by taking the derivatives of $\bar{I}(\mathbf{x})$ (see Appendix B):

$$\mathbf{g} = -c_1 \sum_{\mathbf{j}} (\mathbf{x} - \mathbf{j}) w_d(\mathbf{x} - \mathbf{j}) I(\mathbf{j}) \tag{3.11}$$

$$\mathbf{H} = \sum_{\mathbf{j}} [c_2(\mathbf{x} - \mathbf{j})(\mathbf{x} - \mathbf{j})^T - c_3 \mathbf{I_2}] w_d(\mathbf{x} - \mathbf{j}) I(\mathbf{j}) \tag{3.12}$$

where $\mathbf{I_2}$ is a second-order unit matrix and

$$
\begin{aligned}
c_1 &= \frac{s_0}{s_1} \rightarrow \frac{2}{d^2} \quad \text{for large } d \ll m \rightarrow \infty \\
c_2 &= \frac{s_0^2}{s_1^2} \rightarrow \frac{4}{d^4} \quad \text{for large } d \ll m \rightarrow \infty \\
c_3 &= \frac{s_0}{s_1} \rightarrow \frac{2}{d^2} \quad \text{for large } d \ll m \rightarrow \infty
\end{aligned}
\tag{3.13}
$$

and

$$s_n = \sum_{j=-m}^{m} j^{2n} e^{-\left(\frac{j}{d}\right)^2} \rightarrow \begin{cases} \sqrt{\pi}d & n = 0 \\ \frac{1}{2}\sqrt{\pi}d^3 & n = 1 \end{cases} \quad \text{for large } d \ll m \rightarrow \infty \tag{3.14}$$

The gray scale plot of the Gaussian summation kernels is shown in Figure 3.1. From Equations 3.11 and 3.12, we can immediately find the first-order derivative kernel $-c_1 \mathbf{x} w_d(\mathbf{x})$ and the second-order derivative kernel $(c_2 \mathbf{x}\mathbf{x}^T - c_3 \mathbf{I_2}) w_d(\mathbf{x})$. These two derivative based kernels are very useful in image processings.

3.1.3 Some applications of the Gaussian summation kernels

In §3.1.2 we have derived the mathematical formula of the Gaussian summation kernels. Actually they are often used to detect edges locally which are the places of local transition from one object to another. Most edge detectors are based in some way on measuring the intensity gradient at a point in the image, like $\nabla = (\partial/\partial x, \partial/\partial y)$. However, it is sensitive to noise. A method to reduce noise effects is first convolving the image with a Gaussian filter then taking the gradient, which is exactly the Taylor coefficient $\mathbf{g}$ mentioned previously. This first-derivative-of-Gaussian kernel is the so-called Sobel kernel which is used frequently to enhance edges. We here present three examples of the applications of Sobel kernels in Figure 3.3. The original image taken by EUVI/SECCHI and the image convolved with the Gaussian filter are shown in Figure 3.2. For the three Sobel kernels (only two are independent, g_x and g_y), one takes gradient in x direction, one in y direction, and one in the counter-clockwise direction $45°$ to the x axis. Generally we need to choose the direction of the gradient according to the image we analyse. g_x is designed to identify vertical structures while g_y is often used to detect horizontal edges.
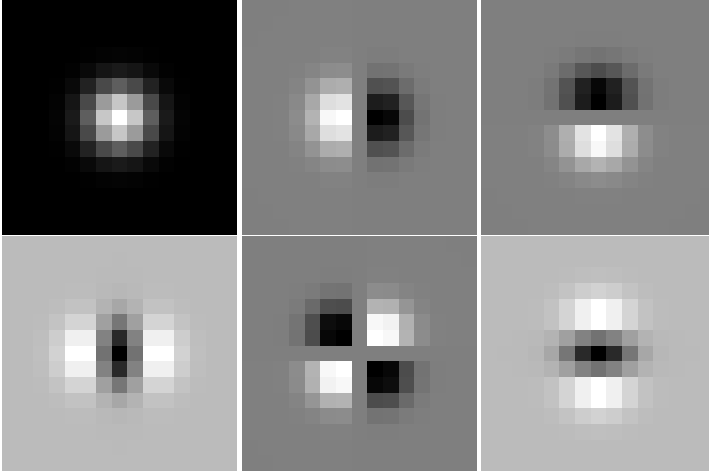
Figure 3.1: Gray scale plot of the summation kernels used to derive the Taylor expansion coefficients for a width $d = 2$ and window size $m = 7$. The upper panels are w, g_x, g_y, respectively from left to right. The lower panels are H_{xx}, $H_{xy} = H_{yx}$, H_{yy} from left to right.
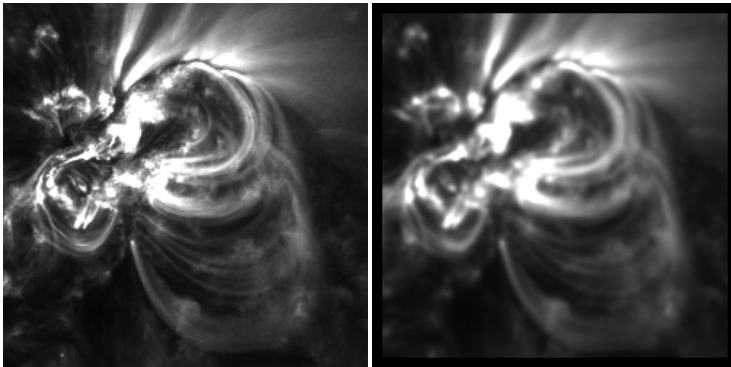
Figure 3.2: Left: the original image of the active region NOAA 10930 taken by EUVI/SECCHI on December 12 2006 at 20:43 UT and at the wavelength of 17.1 nm. Right: the convolved image by a Gaussian filter with a width $d = 2$ and window size $m = 7$.
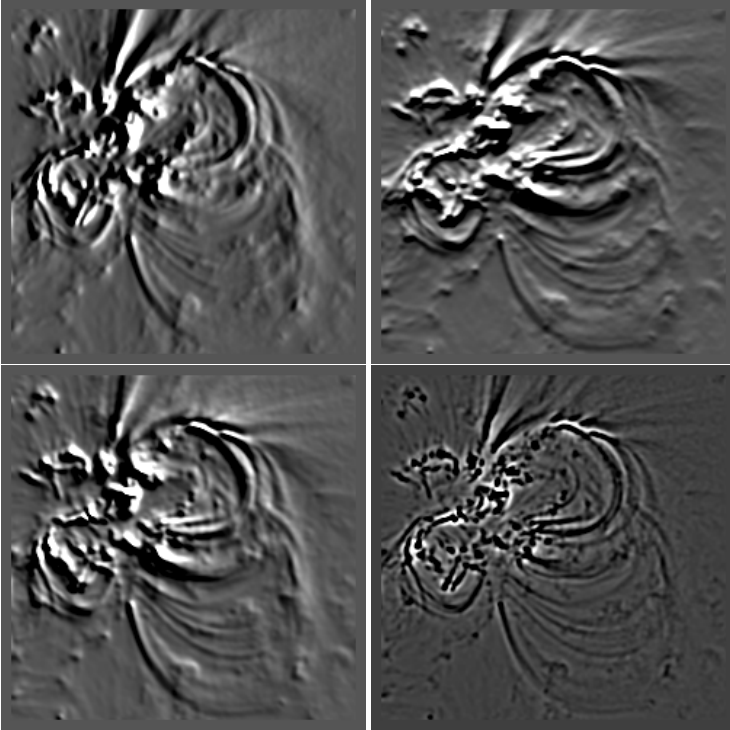
Figure 3.3: Upper left: the original image (left panel in Figure 3.2) convolved with the Sobel kernel g_x. Upper right: the original image convolved with the Sobel kernel g_y. Lower left: the original image convolved with the Sobel kernel $g_x \cos(45°) + g_y \sin(45°)$. Lower right: the original image convolved with the kernel $H_{xx} + H_{yy}$ which is the isotropic mexican hat wavelet. All these kernels have a Gaussian width $d = 2$ and window size $m = 7$.
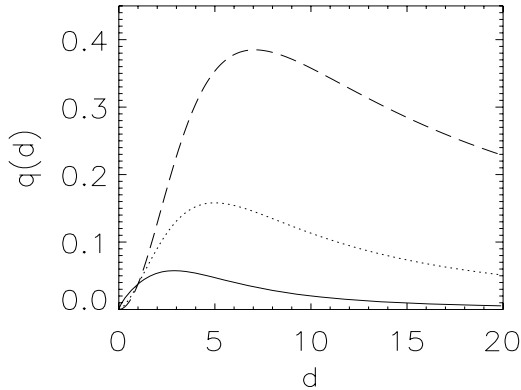
Figure 3.4: The quality as a function of d for $\gamma = 0.75$ (solid line), $\gamma = 1.5$ (dotted line) and $\gamma = 2.0$ (dashed line). In this figure we choose $d_\perp = 5$ as an example. γ can be chosen between 0 to 3.

Most edges are ,however, not sharp dropoffs and often gradually change from one intensity to another. What we usually get is a rising, a peak then a falling gradient magnitude. Therefore finding optimal edges (maxima of gradient magnitude) is thus equivalent to find places where second-order derivative (Laplacian operator) is zero. As we know, this derivative is even more noisy than the first-order one. Consequently, a smooth kernel is necessary here. The result of the image processed by the Laplacian of the Gaussian filter is presented in the lower right panel in Figure 3.3.

3.1.4   Automated scale selection of Gaussian width

It is obvious that in the EUVI image different loops have different width. Even one single loop might have variations in width. For this reason, different Gaussian widths are required for individual pixels. A common problem is to properly choose the parameter d. Lindeberg (1998) has devised a scheme for how this parameter can be optimally chosen. The idea is to apply method two (§3.1.2) for each pixel repeatedly with increasing scales d, thereby estimating the ridge's second-order derivative eigenvalues $h_\perp$ and $h_\parallel$, each as a function of the scale d.

The true intrinsic width of the ridge is calculated by $d_\perp = |(\mathbf{u}_\perp^T \nabla)^2 \log I|^{-1/2} \approx (I/h_\perp)^{1/2}$. In the case of $d \ll d_\perp$, the convolution with a Gaussian filter is equivalent to the convolution with a δ function, hence the filtered image intensities remain almost unchanged, that is, $\bar{I}(\mathbf{x}) \approx I(\mathbf{x})$. we have

$$h_\perp \approx -\frac{I_{max}}{d_\perp^2} \quad \text{for} \quad d \ll d_\perp \tag{3.15}$$

where I_{max} is the intensity at the ridge point in the direction of $\mathbf{u}_\perp$. In the opposite case of $d \gg d_\perp$, $h_\perp$ reflects the second-order derivative of the window shape rather than the original image intensity. Similarly we obtain

$$h_\perp \approx -\frac{\bar{I}_{max}}{d^2}. \tag{3.16}$$

Since the image is convolved with a normalized Gaussian, $\bar{I}_{max}d \approx I_{max}d_\perp$. Therefore,

$$h_\perp \approx -\frac{I_{max}d_\perp}{d^3} \quad \text{for} \quad d \gg d_\perp. \tag{3.17}$$

For $d \approx d_\perp$, we extend $h_\perp$ from the two limiting cases and obtain as approximation for $h_\perp(d)$

$$h_\perp \propto \frac{-d_\perp}{(d_\perp^2 + d^2)^{3/2}} \quad \text{for} \quad d \approx d_\perp. \tag{3.18}$$

For each pixel we establish a quality function

$$q(d) = d^\gamma(|h_\perp(d)| - |h_\parallel(d)|); \quad 0 < \gamma < 3 \tag{3.19}$$

which is shown in Figure 3.4. q first increases as d^γ for small $d \ll d_\perp$, then reaches a maximum where the Gaussian width d matches approximately the local width $d_\perp$ of the ridge, and finally decreases as $d^{\gamma-3}$ for $d \gg d_\perp$. The result of the ridge detection is much less sensitive to variations in γ than to variations in d. Smaller values of γ just shift the position of maximal q to smaller values of d and therefore favour narrower loop structures. In this automated scale selection method, we keep γ constant, but the optimal Gaussian width d is chosen individually for each pixel to be at the scale where $\partial q(d)/\partial d = 0$ which yields

$$d = \sqrt{\frac{\gamma}{3-\gamma}}d_\perp, \quad 0 < \gamma < 3. \tag{3.20}$$

In Figure 3.5, we present the image of quality q for the same example as shown in the lower left in Figure 3.2 obtained with $\gamma = 0.75$ and width d in the range from 0.6 to 4 pixels. As expected, in regions close to loops q has higher values. The probability density function of the optimal Gaussian width d is shown in Figure 3.6. We find that 1/3 of the pixels have an optimal scale less than one pixel, many of which are from the local elongated noise and moss features. For loop structures, the optimal width was about 1.5 pixels with a wide distribution.

3.1.5 Interpolation of ridge positions

We have obtained a number of points which passes the criteria $h_\perp < 0$ and $q > q_{min}$. To reach to the position exactly on the ridge, we need to interpolate across the ridge to arrive at the local maximum. In the neighbourhood of a ridge, along a line across the ridge $\mathbf{x} = \mathbf{i} + \mathbf{u}_\perp t$, the image intensity varies as

$$I(t) \simeq I(\mathbf{i}) + \mathbf{u}_\perp^T \mathbf{g}t + \mathbf{u}_\perp^T \mathbf{u}_\perp h_\perp t^2. \tag{3.21}$$

51

logqlty
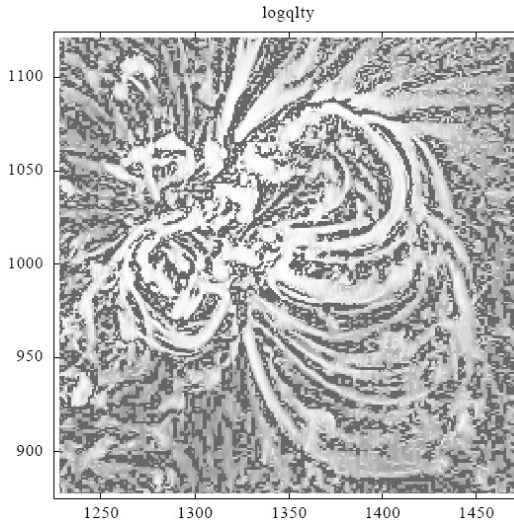
Figure 3.5: The image of the quality factor q obtained from the automated scale selection method (Inhester et al. 2008).

occurence of max quality at width d
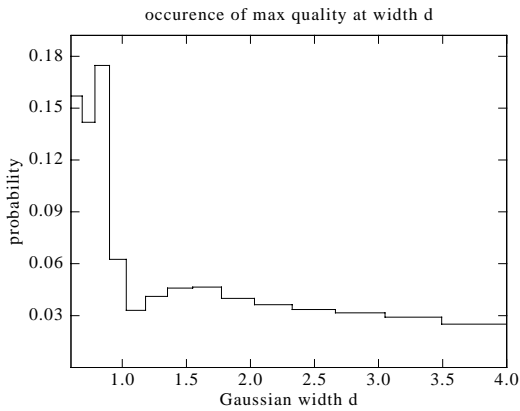
Figure 3.6: Probability distribution of the optimal Gaussian widths d for each image pixel with $h_\perp < |h_\parallel|$ when applied to the image in Figure 3.2 (Inhester et al. 2008).
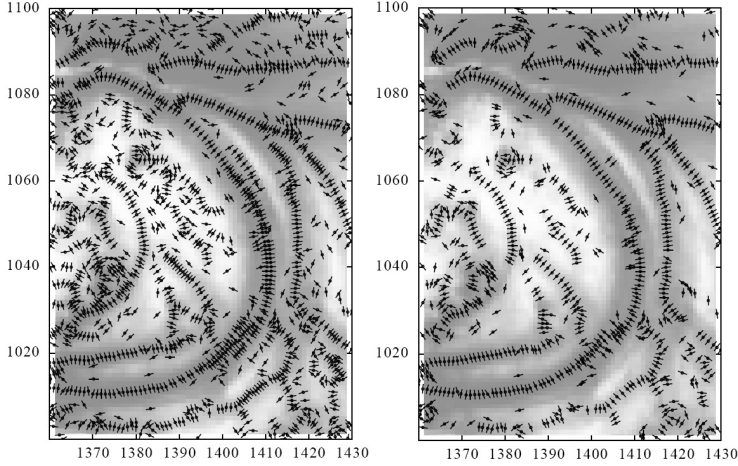
Figure 3.7: The interpolated ridgel positions and orientations for the upper part of the image in the left panel of Figure 3.2 by two methods described in Equations 3.23 and 3.25, respectively. A ridgel is indicated by a dot for position and a small stick for orientation (Inhester et al. 2008).

It can be easily shown that the local maximum is at

$$t_{max} = -\frac{\mathbf{u}_\perp^T \mathbf{g}}{2\mathbf{u}_\perp^T \mathbf{u}_\perp h_\perp} \tag{3.22}$$

and the tangent to the actual ridge curve closer to $\mathbf{i}$ is

$$\mathbf{r}(s) = \mathbf{i} - \frac{\mathbf{u}_\perp \mathbf{u}_\perp^T \mathbf{g}}{2\mathbf{u}_\perp^T \mathbf{u}_\perp h_\perp} + s\mathbf{u}_\parallel \quad \text{for} \quad s \in R. \tag{3.23}$$

The other method to locate the ridge position does not use the perhaps noisy estimate of second-order derivative $h_\perp$ but to interpolate the first-order derivative across the ridge between neighbouring pixel centers $\mathbf{i}$ and $\mathbf{j}$. Define $c = \mathbf{u}_\perp^T(\mathbf{i})\mathbf{u}_\perp(\mathbf{j})$, if $\mathbf{u}_\perp(\mathbf{i})$ and $\mathbf{u}_\perp(\mathbf{j})$ are sufficiently parallel (or antiparallel), that is, $|c|$ is larger than one threshold c_{min}, and $sign(c)(\mathbf{g}^T\mathbf{u}_\perp)(\mathbf{j})(\mathbf{g}^T\mathbf{u}_\perp)(\mathbf{i}) < 0$, then we can determine the ridge position by

$$\mathbf{r} = \mathbf{i} + t(\mathbf{j} - \mathbf{i}) \tag{3.24}$$

where

$$t = \frac{(\mathbf{g}^T\mathbf{u}_\perp)(\mathbf{i})}{(\mathbf{g}^T\mathbf{u}_\perp)(\mathbf{i}) - sign(c)(\mathbf{g}^T\mathbf{u}_\perp)(\mathbf{j})}. \tag{3.25}$$

In Figure 3.7, we compare the interpolated ridge points (ridgels hereafter) obtained with these two methods for the same image. In general, the second method produces fewer ridgels along a loop but the distance among the ridgels is relatively constant. As
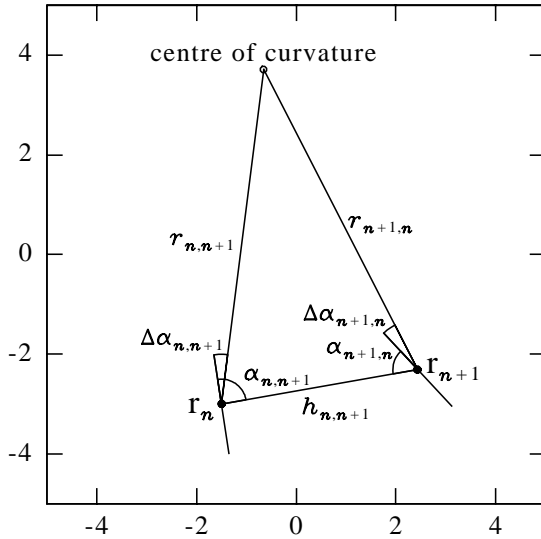
Figure 3.8: Illustration of the cocircularity condition proposed by Parent and Zucker (1989). The ridgel positions are indicated by two small dots, the orientations of $\mathbf{u}_\perp$ at these two ridgels are shown by two short lines centered at ridgel dots (Inhester et al. 2008).

already mentioned before, the second method has the advantage of avoiding the noisy second-order derivatives. However, it has a few disadvantages at the same time. For example, it needs at least two points to interpolate the ridge position. Consequently, it can not detect faint ridgels that are just one pixel wide. Moreover, with the second method, we can only detect the ridge points at the intersections of the ridge with the grid lines connecting $\mathbf{i}$ and $\mathbf{j}$. For ridges oriented obliquely to the grid lines, the distance between neighbouring ridge points may vary by some amount.

3.2   Ridgel connections to chains

After detecting the individual ridgels, the next step is to connect them into chains of ridgels. In this section we will first decide whether two neighbouring ridgels $\mathbf{i}$ and $\mathbf{j}$ can be connected or not by calculating an associated weight proposed by Parent and Zucker (1989). Then the allowed connections are stored, ordered and combined to chains.

For two ridgels at $\mathbf{r}_n$ and $\mathbf{r}_{n+1}$ with the distance of $h_{n,n+1}$, we construct an isosce-

les triangle with two symmetrical sides as shown in Figure 3.8. One side is formed by connecting two ridgels. The vertex opposite to this side is defined such that the two symmetrical sides of the isosceles triangle make the square of the angles $\Delta\alpha_{n,n+1}^2 + \Delta\alpha_{n+1,n}^2$ (see Figure 3.8) minimal, the cocircularity condition suggested by Parent and Zucker (1989). The resulting vertex is called the center of curvature. If we assume the angles are positive in clockwise direction from $\mathbf{u}_\perp$, we have $\alpha_{n,n+1} - \Delta\alpha_{n,n+1} = -\alpha_{n+1,n} + \Delta\alpha_{n+1,n}$ due to the property of the isosceles triangle. Thus,

$$\min \, (\Delta\alpha_{n,n+1}^2 + \Delta\alpha_{n+1,n}^2) = \min_{\Delta\alpha_{n,n+1}} \, (\Delta\alpha_{n,n+1}^2 + (\alpha_{n,n+1} + \alpha_{n+1,n} - \Delta\alpha_{n,n+1})^2), \qquad (3.26)$$

Then we can easily find that, the minimum is achieved when

$$\Delta\alpha_{n,n+1} = \frac{1}{2}(\alpha_{n,n+1} + \alpha_{n+1,n}) = \Delta\alpha_{n+1,n}. \qquad (3.27)$$

The local radius of curvature $r_{n,n+1} = r_{n+1,n}$ can be calculated from

$$r_{n,n+1} = r_{n+1,n} = \frac{\frac{1}{2}h_{n,n+1}}{\cos(\frac{1}{2}(\alpha_{n,n+1} - \alpha_{n+1,n}))} \qquad (3.28)$$

With each connection between one pair of ridgels we associate one weight, named a binding energy defined by the parameter $\Delta\alpha_{n,n+1}$, $r_{n,n+1}$ and $h_{n,n+1}$:

$$e_{n,n+1} = (\frac{\Delta\alpha_{n,n+1}}{\alpha_{max}})^2 + (\frac{r_{min}}{r_{n,n+1}})^2 + (\frac{h_{n,n+1}}{h_{max}})^2 - 3 \qquad (3.29)$$

As proved above that $\Delta\alpha_{n,n+1}^2 = \Delta\alpha_{n+1,n}^2$, thus we have $e_{n,n+1} = e_{n+1,n}$. The right side of Equation 3.29 measures three types of distortions and can be regarded as three corresponding energies of an elastic line element. The first term measures the deviation of the two ridge orientations from the cocircularity condition; the second and the third ones measure the bending and stretching, respectively. α_{max}, r_{min} and h_{max} are three free parameters needed to be set by users and give us control on the relative weight of the three terms. α_{max} is the upper limit of the deviation from cocircularity, r_{min} the smallest acceptable curvature radius, h_{max} the largest acceptable distance. Therefore, only connections with negative energy are allowed.

In practice, the energy in Equation 3.29 has some problems because it tends to discard ridgel pairs with small $h_{n,n+1}$. As is seen in Equation 3.28, $r_{n,n+1}$ is proportional to $h_{n,n+1}$ which makes $r_{n,n+1}$ go down below r_{min} very easily for a nearby ridgel pair. For this reason we allow for measurement errors in $\mathbf{r}$ and $\mathbf{u}_\perp$. The binding energy is modified accordingly to the minimum within these given error ranges.

In the next step all the allowed ridgel connections with a negative energy are stored, ordered with respect to energy and combined to reach a global energy minimum. We started from the connection with the lowest energy and connect ridgels to chains by searching the allowed connections. Each ridgel has two sides divided by $\mathbf{u}_\perp$ and we only allow at most one connection on either side. Connections to one side of a ridgel which has already been occupied by a lower energy connection before are simply discarded. The connections in this way reach an energy state close to global minimum. However, we might miss a lower global energy state by always searching the next ridgel according to a relative lower energy locally. It might happen that a connection between ridgels i - j with some energy $e_{i,j}$
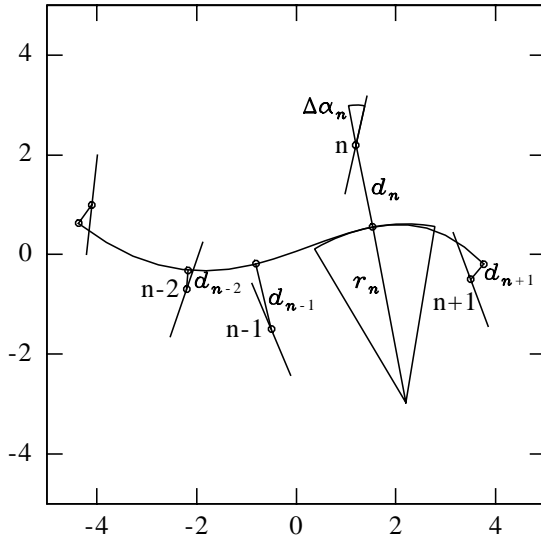
Figure 3.9: Sketch of the curve fit parameters d_i, $\Delta\alpha_i$ and r_i. The ridgels are indicated by their locations and orientations. For each ridgel i, $d_i = |\mathbf{d}_i|$ is the distance, $\Delta\alpha_i$ the angle between the direction of $\mathbf{d}_i$ and the ridgel orientation, r_i the curvature radius (Inhester et al. 2008).

prevents a bypass i - k - j with energy $e_{i,k} + e_{k,j} < e_{i,j}$ but $e_{i,k}$, $e_{k,j} > e_{i,j}$ because connection i - j was introduced earlier. Since $e_{n,n+1} = e_{n+1,n}$ this global minimum problem can be considered a minimizaion problem of undirected graphs. Some improvements should be found from graph theory.

3.3 Curve fits to the ridgel chains

The final step is to fit the connected ridgel chains to smooth curves. What we use here are the higher-order polynomials from third to fifth order since the curvature of coronal loops does not change much along them. We tried high-order spline functions as well. However, they are too flexible for the curves we aim at. For a 2D polynomial curve we have the parametric form

$$\mathbf{p}(t) = \sum_{n=0}^{5} \mathbf{q}_n t^n \quad \text{for} \quad t \in [-1, 1]. \tag{3.30}$$

The polynomial coefficients q are determined by minimizing

$$\sum_{i \in \text{chain}} (\mathbf{d}_i^T \mathbf{d}_i) + \mu(\mathbf{p}''^T \mathbf{p}'')(t_i) \tag{3.31}$$

with respect to $\mathbf{q}_n$ for a given μ. Here,

$$\mathbf{d}_i = \mathbf{r}_i - \mathbf{p}(t_i) \tag{3.32}$$

are the distances of the ridgels from the curve fit. The distribution of node points t_i is initially ordered in the interval $[-1, 1]$ so that $t_i - t_{i-1}$ is proportional to the geometrical distances $|\mathbf{r}_i - \mathbf{r}_{i-1}|$. By making the derivative of 3.31 with respect to $\mathbf{q}_n$ zero and solving the resulting linear algebra equations of $\mathbf{q}_n$, we obtain the corresponding coefficients $\mathbf{q}_n(\mu)$. Once a new set of $\mathbf{q}_n(\mu)$ for a given μ is calculated, the curve nodes t_i are replaced by the exact closest point to $\mathbf{r}_i$

$$t_i = \text{argmin}_t (\mathbf{r}_i - \mathbf{p}(t))^2. \tag{3.33}$$

The second-order derivative $\mathbf{p}''$ is introduced to control the curvatures of the polymonial curve. For different μ, the minimum 3.31 generates fit curves with different curvatures. To find an optimal μ, we set up a scheme in Figure 3.9 and minimize the equation with respect to μ below:

$$E_{\text{chain}}(\mu) = \sum_{i \in \text{chain}} \frac{d_i^2}{d_{\text{max}}^2} + \sum_{i \in \text{chain}} \frac{\Delta \alpha_i^2}{\alpha_{\text{max}}^2} + r_{\text{min}}^2 \int_{-1}^{1} \frac{1}{r(t)^2} \, dt \tag{3.34}$$

The first two terms generally require a large curvature which is balanced by the third term. Because E depends on μ nonlinearly we cannot obtain the optimal μ as we did for the polynomial coefficients $\mathbf{q}_n$. Alternatively, we compute it in an iterative way with μ starting from a large numerical value. The parameters d_{max}, α_{max} and r_{min} are chosen to tune the relative weights between the mean square of spatial and angular deviations of the fit from a chain of ridgels and the integrated curvature of the fit.

The final curve fits of fifth-degree polynomials to the connected ridgel chains are presented in the left panel of Figure 3.10. The ridgels are detected by the automated scale selection method and then interpolated with the first interpolation method described in Equation 3.23. However, from this image we have segmented not only loop structures but some other bright structures, for example, moss. The image processing scheme itself cannot distinguish between them. Therefore in the last step, we interactively clean unwanted loop-irrelated structures and split and merge some obvious loop features. On the right side of Figure 3.10 the result from this last step of modification is shown.

3.4 Discussions

In an EUV image of the Sun we can identify plenty of structures including coronal loops. For some specific loop studies, it is required to extract their shape from the EUV image. One of such applications is to compare the traced loops with the projected magnetic field lines since coronal loops should outline magnetic field lines due to the high electric
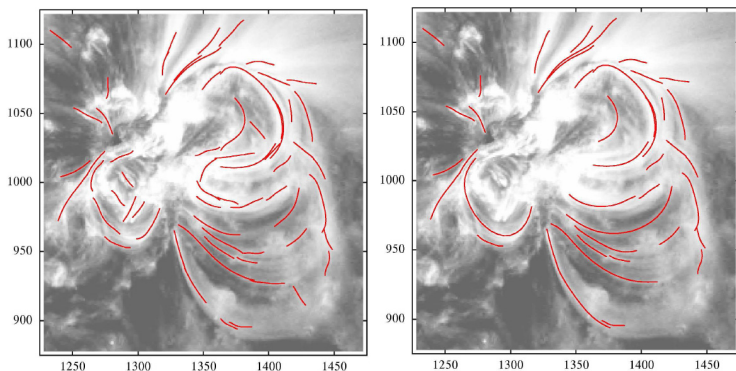
Figure 3.10: Left: curve fits to ridgel chains by the fifth-order polynomials. Right: Results from cleaning, splitting and merging of loop structures by a user interactive tool (Inhester et al. 2008).

conductivity in the coronal plasma. This comparison could serve as a validity test for the underlying field-extrapolation methods. The comparison could be done either with loops traced from a one-view EUV image or with loops identified from two images taken simultaneously from two view directions.

Inhester et al. (2008) compared the loops extracted from the EUVI image taken on December 12 2006 at 23:43:11 UT with the magnetic field lines extrapolated from linear force-free field models with the force-free parameter α varied in the range from -0.0427 Mm^{-1} to 0.0356 Mm^{-1}. The results of the comparison show that each identified loop is associated with a field line with different α values. It indicated that a linear force-free field model is not sufficient for this active region. Actually an X-class flare occurred in this active region next day. Therefore the time when the traced loops were observed in Inhester et al. (2008) was in the preflare period. According to the nonlinear force-free field extrapolations in the same active region, we find that the magnetic field lines are highly sheared in the core field region in this period (Guo et al. 2008).

Due to the projection effect, the optimal force-free parameter α inferred by comparing the projected field lines with loops observed from only one view point is problematic, because several field lines with different α values might produce the same projection. The best-fit magnetic field line to a given loop might not be unique. This problem could be solved if we compare the extrapolated field lines with the loops identified from two simultaneously recorded images from two view directions. The details will be presented in the next chapter where the extracted loops are used for the tie point stereoscopic reconstructions in order to obtain their 3D geometry.

The SDO mission in the future will have very high time cadence of observations and a huge number of images will be recorded. Therefore, automated feature detection tools will be quite helpful to study the time evolution of structures. In the case of coronal loops, loop oscillations will be a very interesting application of our tool.

4 Stereoscopic Reconstruction of coronal Loops

STEREO provides us with the first opportunity to observe the Sun-Earth system simultaneously from two different viewpoints. Three dimensional information of quiescent coronal structures as well as of dynamic phenomena such as Coronal Mass Ejections (CMEs) can be inferred. A fundamental 3D reconstruction task is to reconstruct coronal loops, the building blocks of the solar corona. Before STEREO data become available, all the stereoscopy work made use of the solar rotation and had to be based on the assumption that the magnetic structures are stable within the time interval used for stereoscopy. In this chapter, we will first present the stereoscopic reconstruction of the loops observed one day apart by TRACE which serves as a preparation for the real EUVI/SECCHI data from STEREO. In the second section of this chapter, 3D reconstructions of the loops observed by EUVI on board STEREO are detailed. The EUVI image pairs are recorded simultaneously and no assumption on the time evolution of loops is required for the stereoscopic technique we use.

4.1 Stereoscopy of the loops observed by TRACE

Assuming stationary loop structures, a triangulation method has been applied to Skylab/XUV data by Berton and Sakurai (1985) and to SOHO/EIT data by Portier-Fozzani and Inhester (2001). Aschwanden et al. (1999b) and Aschwanden et al. (2000) generalized the concept of solar-rotation stereoscopy to dynamic stereoscopy which allows the loop structures to evolve dynamically. They traced out individual loops from two EIT images observed one day apart. For each of these loops they determined a circular fit and allowed the fit parameters to smoothly vary in time.

For the STEREO mission, Wiegelmann and Inhester (2006) developed a tool of magnetic stereoscopy which combines pure geometrical stereoscopy with estimations of the local magnetic field orientation from different magnetic field models. Their work showed that the extrapolated field lines can help to remove the ambiguities inherent in classical stereoscopy. They applied their method only to a model active region from which they computed artificial loops as seen from two different viewpoints. In this work we apply this magnetic stereoscopy to real TRACE and SOHO/MDI data. This represents a test of the method to solar data affected by noise, instrumental artifacts, etc.
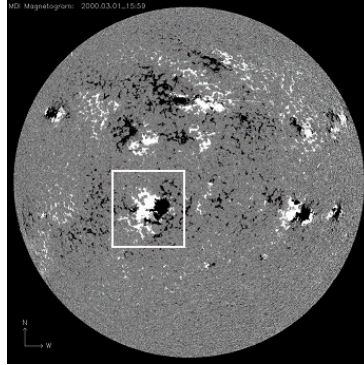
Figure 4.1: SOHO/MDI line of sight magnetogram observed on 1 March, 1535UT with NOAA 8891 located in the white square (Feng et al. 2007b).

4.1.1   Observations and Loop Identification

The investigated long-lived active region NOAA 8891 was visible on the disc from February 26 2000 to March 9 2000. The TRACE Flare Catalog, http://hea-www.harvard.edu/ trace/flare_catalog/index.html, lists no M or X class flares occurring in this active region during the above time. For the stereoscopy work we concentrate here on the data observed on March 1 and March 2 when the active region was close to solar center. A first task is to identify one dimensional curves out of the 2D EUV images. In the following we call these 1D structures "loops". Projected 3D magnetic field lines (which are 1D structures as well) are called "projected field lines". There was no flare happening in this active region during these two days, so we can assume that the magnetic field was slowly evolving and can be considered as invariant over short time scales (say during one day or so). The active region we concentrate on is marked by the white square in Figure 4.1 observed by SOHO/MDI.

Figure 4.2 shows two EUV images of this active region recorded by TRACE in the 171 Å waveband about one day apart, one on March 1, 1422UT and the other on March 2, 1744UT. We can regard TRACE image on March 2, 1744UT as an approximation of the EUVI image from STEREO A, and TRACE image on March 1, 1422UT as from STEREO B. To correct the TRACE pointing, the two TRACE images are calibrated separately with the SOHO/EIT data closest in time (March 1, 1300UT and March 2, 1900UT). The sun rotated about 17 degrees during the above time.

Coronal loops are often visible only as faint structures, even in TRACE images which at present have the highest spatial resolution. To enhance the loop structures in the two TRACE observations, high-pass filtered images are created by subtracting a 5×5 boxcar smoothed image from the original image. Figure 4.3 shows the filtered results. Subsequently the loops are traced out in the filtered images and marked in Figure 4.4. Because the right part of Loop 0 in the left panel of Figure 4.3 is invisible, a white line is shown
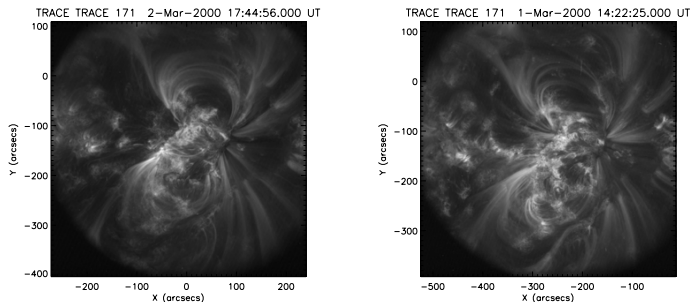
Figure 4.2: TRACE 171 Å data of AR 8891 on March 1, 1744UT (left) which can be looked as an image taken by EUVI on board STEREO A and March 2, 1422UT (right) as an image observed by EUVI B (Feng et al. 2007b).

in the left panel of Figure 4.4 as a reference of the direction of Loop 0. It is segmented out from another TRACE image which was observed on March 1, 1351UT, about 30 min earlier, Its coordinates were then transformed onto March 1, 1422UT by aligning both images to the EIT image observed on March 1, 1300UT. Loop identification is not straight forward. Here the loops are traced by hand. Efforts towards developing an automated loop tracing tool have been made and an overview about the current developments is given in Aschwanden et al. (2008a), Lee et al. (2006) and Inhester et al. (2008) (See Chapter 3).

4.1.2   Magnetic Field Extrapolation and Field Line Projection

The coronal magnetic field usually cannot be measured directly. Therefore one has to extrapolate it from photosphere magnetic observations (line of sight or vector magnetograms). Because of low β values in the lower corona, the magnetic field can be considered force-free. In this work we use the linear force-free field extrapolation method (Seehafer 1978) described in Chapter 2 to match loop pairs from two TRACE images. The required accuracy of the field lines which is needed to associate loops depends both on the resolution of the image and on the average distance between the individually identified loops in the image. The distance of the projected field lines to the loops should be smaller than the distance between neighbouring loops.

Combined with the divergence-free condition, the force-free equations are written as:

$$\nabla \times \mathbf{B} = \alpha \mathbf{B} \tag{4.1}$$

where α is a constant for linear force-free field. The input of the extrapolation code is the SOHO/MDI line-of-sight magnetogram observed on March 1 1535UT. The model has one free parameter "α" which is a priori unknown. Several authors (e.g. Carcedo et al.
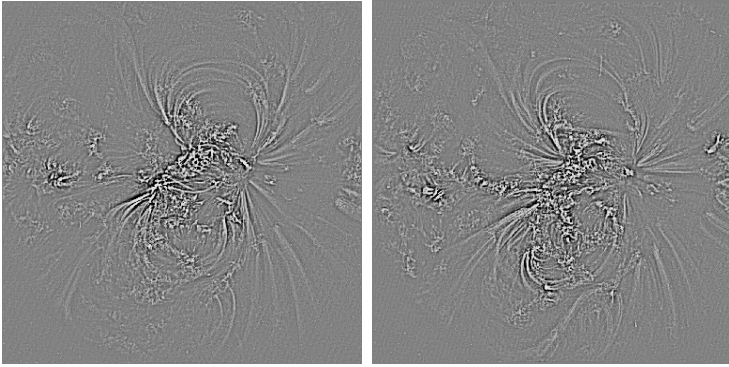
Figure 4.3: High-pass filtered TRACE 171 Å images on March 1, 1744UT (left) and March 2, 1422UT (right) (Feng et al. 2007b).
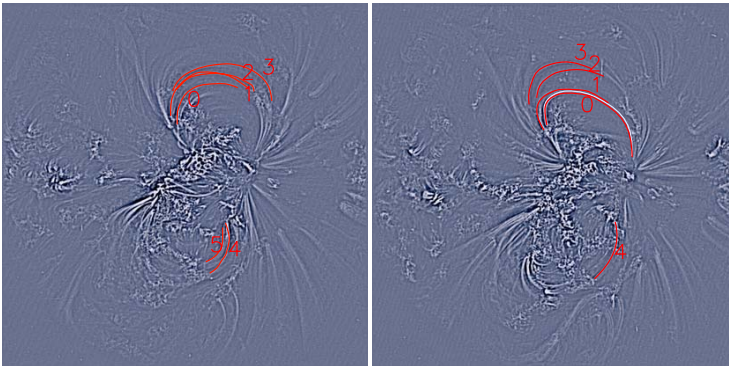
Figure 4.4: Hand-traced loops (red lines) marked with numbers on the filtered TRACE 171 Å images observed on March 1, 1744UT (left) and March 2, 1422UT (right). In the right image, the white line is segmented out from another TRACE image which is observed on March 1, 1351UT and then tranformed its coordinate onto March 1, 1422UT (Feng et al. 2007b).
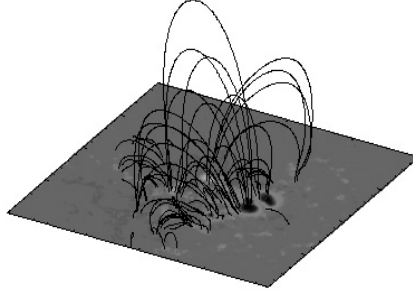
Figure 4.5: Three dimensional potential magnetic field of NOAA 8891 extrapolated from SOHO/MDI data. Only closed field lines are plotted (Feng et al. 2007b).

2003, Marsch et al. 2004) used coronal images in EUV, X-ray and Hα to compute the optimal linear force-free parameter α by comparing magnetic field line plots with images from a single viewpoint (e.g. SOHO, Yohkoh).

The Seehafer solution is computed on a rectangular grid 0 - L_x and 0 - L_y and contains the free force-free parameter α. To normalize α, we choose the harmonic mean L of L_x and L_y defined by

$$\frac{2}{L^2} = \frac{1}{L_x^2} + \frac{1}{L_y^2}.$$

(4.2)

The force-free parameter αL is limited by - $\sqrt{2}\pi \leq \alpha L \leq \sqrt{2}\pi$ in the Seehafer solution. Potential fields correspond to $\alpha = 0$. We have computed the linear force-free field model with $L_x = L_y = L = 285Mm$ for 45 different values of α varied from -0.0156 Mm^{-1} to 0.0156 Mm^{-1} (for convenience of calculation, the value of αL increases by 0.2 at every step). For each field line, the starting point is chosen randomly in the photosphere in the region where the magnetic field strength is larger than 20 G. In total, 4183 field lines have been computed. We show as example the potential field (*i.e.* the case $\alpha = 0$) in Figure 4.5. Here only the closed field lines are plotted as we are only interesting in closed coronal loops.

The extrapolated 3D magnetic field lines should be projected onto both TRACE images to be compared with identified loop structures. To facilitate the projection, we convert the position of points (x_i, y_i, z_i) on a 3D field line from the coordinate system of the extrapolation respectively to the two heliocentric coordinate systems established for the
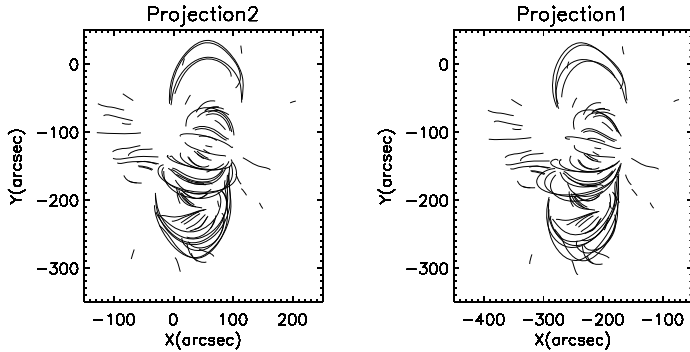
Figure 4.6: Projection results of the extrapolated 3D potential field lines along two TRACE view directions. The left image is for the viewpoint B on March 1, 1744UT and the right one for the viewpoint A on March 2, 1422UT (Feng et al. 2007b).

TRACE observations (details of the coordinate transformation are described in Appendix C). The projection results for the potential field lines are given in Figure 4.6 as an example. The left image shows the projection along the TRACE view direction on March 1, and the right one along the view direction on the next day, March 2. Comparing these two projection images with the two TRACE images, we can see that generally the potential field lines indicate the directions of the identified loops. A quantitative analysis will be discussed later and shown that potential and even linear force-free field is not sufficient.

4.1.3   Magnetic Stereoscopy

In two TRACE images we have five identified loop structures for viewpoint A, six loop structures for viewpoint B; On the other hand we have 4183 projected field lines for both viewpoints. They form the necessary materials to reconstruct the 3D geometry of coronal loops. In a first step, we quantify the distance of the projected field lines to each loop. Two loops in different images (later we call the TRACE image observed on March 1 TRACE Image A, and the other one TRACE Image B) are defined to form a pair if there is a common field line which projects closely to both loops. Then the stereoscopic reconstruction is performed with the identified loop pairs.

4.1.3.1   Loop pair identification

The faint, diffuse coronal plasma and the "jungle" of nested loops do not allow a clear association of loops in two TRACE images with each other. However, this is an important step before the stereoscopic reconstruction. If the problem of loop association is not solved properly, the stereoscopic reconstruction can fail or lead to incorrect results.
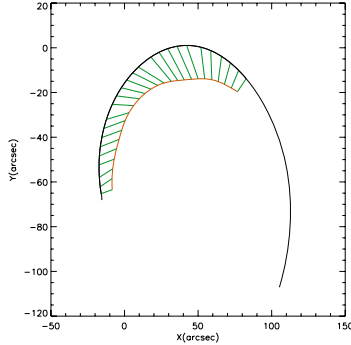
Figure 4.7: This figure illustrates how the parameter $C_l(b)$ is calculated. Red line is one traced loop, black line is one projected magnetic field line and Green sticks show the area between the loop and the part of the field line corresponding to the loop (Feng et al. 2007b).

To quantify how good the correspondence is between a loop combination from both TRACE images, we introduce three quantities $C_{l_A l_B}(b)$, $C_{l_A}(b)$ and $C_{l_B}(b)$. $C_{l_A}(b)$ measures the average distance between the loop l_A in TRACE Image A and a certain projected field line b and shows how well the loop and field line agree with each other. $C_{l_B}(b)$ is similar to $C_{l_A}(b)$ but for TRACE Image B. Both are defined as the area between the traced loop and the projected field line divided by the loop length (see Figure 4.7). $C_{l_A l_B}(b)$ is the average of $C_{l_A}(b)$ and $C_{l_B}(b)$. Two points should be mentioned here. At first, for the case that the field line is much shorter than the loop, they do for obvious reasons not match well. We penalize $C_{l_A}(b)$ or $C_{l_B}(b)$ by a large number (1000 arcsec in our calculation). Conversely, if the observed loop is shorter than the projected field line, this match is accepted. Secondly, because it is difficult to trace the exact positions of the loop footpoints, the section near the footpoints of the loops is omitted to get a more precise average distance (see Figure 4.7 as an example).

For each loop pair combination, that is one loop picked from Image A and the other loop picked from Image B, we can find a certain field line from the total of 4183 field lines which minimize $C_{l_A l_B}(b)$. It is easy to understand that the smaller $C_{l_A l_B}(b)$ is, the better the loop pair associate with each other. For a better visualization, we plot $1/C_{l_A l_B}(b)$ in Figure 4.8 (left). The left panel shows the initial results of loop matching. The loop pairs found in this way and their best fit field lines are used later as references to obtain further results.

Because the starting footpoints of all the 4183 field lines we calculated here are randomly selected on the photosphere and the interval of the 45 α values is not small enough, we might have missed some more precise candidates which fit the loop pairs even better. To find these improved candidates, for each possible loop pair found from the initial results, we calculate additional field lines with smaller steps in α and with their footpoints
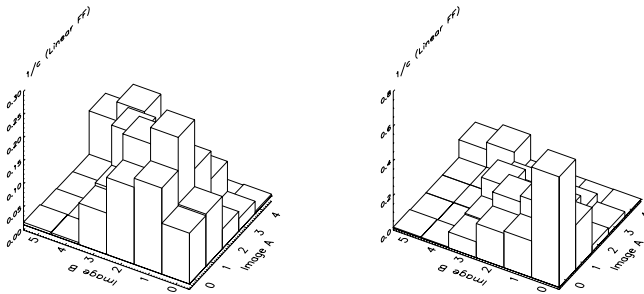
Figure 4.8: Loop association with linear force-free field model. The matrix $C_{l_A l_B}(b)$, where C is in units of arcsecond, shows how well each loop in Image A associates with each loop in Image B. The horizontal axes are the loop numbers from Figure 4.4 . Higher value corresponds to better association. The left panel shows the initial results of loop matching found by a coarse field line group. The right panel is the final results identified through the comparison with a more refined field line group. The maximum value of the vertical axis increases from 0.3 arcsec to 0.8 arcsec (Feng et al. 2007b).

focussed near the footpoint of the optimal field line found so far. The starting points on the photosphere of the new field lines are regularly distributed on a 10 arcsec wide circle centered at the starting point of the old optimal field line associated with the respective loop pair. Moreover, the αL in steps of 0.1 are varied around the value of the old optimal field line. Now comparing all the 2585 new field lines gathered from every group with the loops traced from Image A and Image B, we obtain a more precise result (see the right panel of Figure 4.8). The most probable loop pair which has the smallest value of $C_{l_A l_B}(b)$ has now changed from loop pair (1-1) (C = 3.71 arcsec) to loop pair (0-0) (C = 1.54 arcsec). From Figure 4.8 we can see the maximum value of the vertical axis increases from 0.3 arcsec to 0.8 arcsec.

All the possible loop pairs we have found are listed in Table 4.1 with the αL value of the field line that best fits each loop pair. The obtained fits suffer from the non-simultaneous recording of the two TRACE images, so that, the loop structures may have evolved from one day to the other due to the lifetime of EUV loops. This problem does not exsit for the STEREO data. Table 4.1 demonstrates that there need not be a one-to-one correspondence between loops and field lines. Loop pairs 2 and 3 both contain loop No. 1 in Image A. $C_{l_A l_B}(b)$ is relatively similar in both cases, so that, it can only formally be used to favour loop pair 2. In view of the non-uniqueness of loop pair combinations and loop evolution, we only reconstruct the 3D loop for the most probable loop pair (0-0) in the next subsection. This loop pair and its best fit field line are shown in Figure 4.9. The correspondence is surprisingly good, considering the uncertainties inherent in magneto-
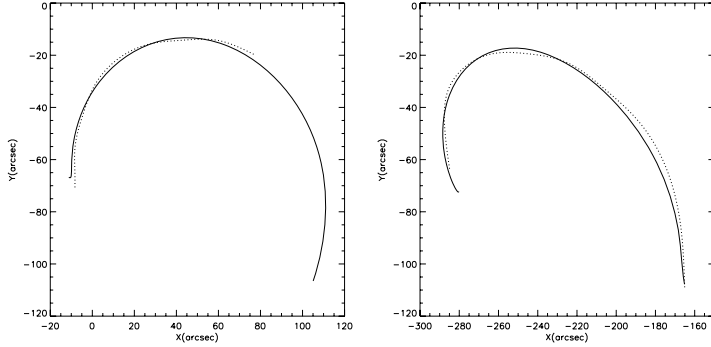
Figure 4.9: Dotted lines: loop No.0 in Image B (left) and loop No.0 in Image A (right); Solid lines: projections of the best fitting field line onto the respective image, we use b(0,0) as the notation for this field line (Feng et al. 2007b).

Table 4.1: List of the possible loop pairs and α values of the field line best fit with each loop pair (Feng et al. 2007b).

Loop pair	Loop No.(Image A)	Loop No.(Image B)	$C_{l_A l_B}$(b)(arcsec)	$\alpha(10^{-3}Mm^{-1})$
1	0	0	1.54	-4.2
2	1	1	3.08	-5.3
3	1	2	3.45	-5.3
4	2	3	4.63	-4.2
5	4	4	6.36	2.8

graph measurements (which do not compensate for the unknown properties of magnetic elements, Solanki (e.g. 1993)).

In this work we extrapolate the magnetic field with the linear force-free field model which assumes constant α value in this active region. However, from Table 4.1 we find negative α values for the loop pairs in the northern part of this active region, while in the southern part, positive α value is obtained. This is in contradiction with the linear force-free assumption and indicates that this magnetic field model is not a perfect approximation of the loops in NOAA 8891. It should be noted that the magnetic field lines which were calculated cannot be considered to represent a valid field model because their α value differs. We here use the field lines only as a mean to associate loops. Wiegelmann and Neukirch (2002) also investigated whether the linear force-free field model is good enough to approximate the loops in active region NOAA 7986. They found similar results to this work: different α values are needed to describe different subgroups of loops. So the nonlinear force-free field model would be a better field model for this active region (cf. Wiegelmann et al. 2005b).
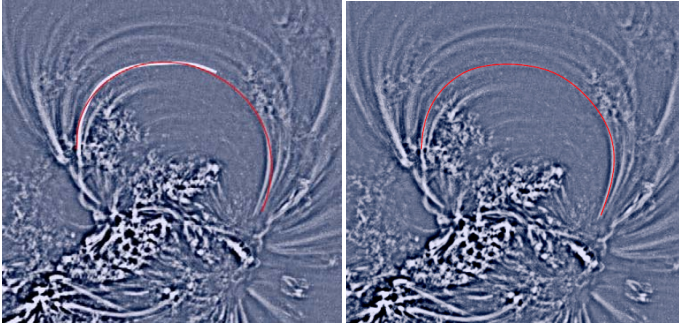
Figure 4.10: Left: the white line shows the traced partial Loop 0 in Image B and the red line is the best fit field line b(0,0) with this loop. Right: the red line shows the extended complete loop following the guide of the field line b(0,0) (Feng et al. 2007b).

4.1.3.2   Complete loop feature identification

One problem for the stereoscopy of loops is that not always the same segments of a loop are well visible and clearly identified in the two images. As can be seen from Figure 4.9, this is clearly the case for loop pair 1. We employ the best-fit magnetic field line $b(0,0)$ as a guide to extend the loops 0 in Image A and B. The originally identified loop and the field line $b(0,0)$ are overplotted on Image B in the left panels of Figure 4.10; the traced complete loop is shown in the right panels.

Lee et al. (2006) introduced a method to automatically segment solar loops based on the oriented connectivity and used the potential magnetic field model to guide the loop orientation. As they pointed out, sometimes the simplicity of the physical model could cause the segmentation process to fail. Therefore, computed field lines lying as close as possible to the true loops should be combined to extract reliable loop structures. Without additional information it is hard to clearly identify loops in plasma images. A projection of computed magnetic field lines can help to achieve this aim. Magnetic field lines do, of course, exist space filling in the corona and might depend additionally on *a priori* unknown parameters, *e.g.* the force-free parameter α. For the identification of a plasma loop we choose the field line, which is (in 2D projection) closest to the loop in the image to guide the loop direction.

4.1.3.3   Stereoscopic reconstruction

In this subsection we show as an example the stereoscopic reconstruction from the loop pair (0-0) and we demonstrate how the best fit field line $b(0,0)$ helps with this reconstruction.

For the stereoscopy method test, we at first reconstruct the 3D curve from the two projections of the field line $b(0,0)$ to check whether the result is the original 3D field
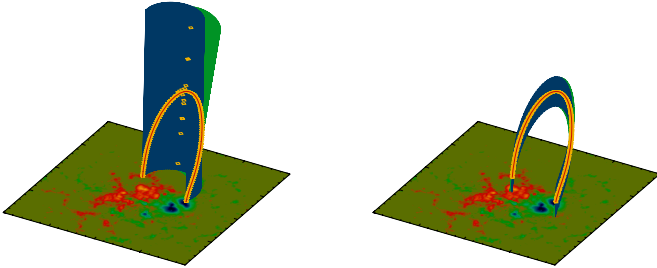
Figure 4.11: Geometrical stereoscopy from two projections of field line $b(0, 0)$. The blue surface is generated by back projection along the view direction of Image A, and the green surface is along the view direction of Image B. Yellow points are the solutions of 3D reconstruction. Left: the results of purely geometrical stereoscopy, right: the results of magnetic stereoscopy. Two red lines: 3D field line $b(0, 0)$ (Feng et al. 2007b).

line or not. The basic idea of our geometrical stereoscopy is given in the left panel of Figure 4.11. The 1D curves (projected field line or identified loop) can be projected back along the view direction which generates a 3D solution surface on which the real 3D curve must lie. From two view directions, we obtain two such surfaces and their intersection must be the 3D solution (Wiegelmann et al. 2005a, Wiegelmann and Inhester 2006).

In the case of the two projections of $b(0, 0)$, classical stereoscopy gives two solutions: one is the correct original 3D field line, the other consists of some yellow points strung out nearly in the vertical direction. Considering the epipolar geometry, since the epipolar lines for STEREO and TRACE observation are only slightly inclined with respect to the ecliptic, loops in north-south direction which intersect epipolar lines only once are reconstructed straight. For the loops in an east-west orientation, two-time intersection usually yields two solutions that cross each other (Inhester 2006a). Obviously the second solution is a ghost 3D feature introduced by the fact that the coronal plasma is optically thin and we should find a way to remove it. The presence of such ghosts is particularly annoying since most loops are expected to be oriented roughly in the east-west direction.

To get rid of the ghost feature we add the information of the best fitting magnetic field line $b(0, 0)$ to the purely geometrical stereoscopy. This is achieved by limiting the Z range (*i.e.* normal coordinate) of the two back projection surfaces to ± 8 arcsec (the exact value is not important to the results) of Z values of the field line $b(0, 0)$. The stereoscopic reconstruction result using this additional constraint is shown in the right panel of Figure 4.11. Now the ghost feature has disappeared.

Now we apply this magnetic stereoscopy method to the TRACE data, loop pair 0-0. The 3D reconstruction of this loop pair (Figure 4.12) is marked by the yellow dotted
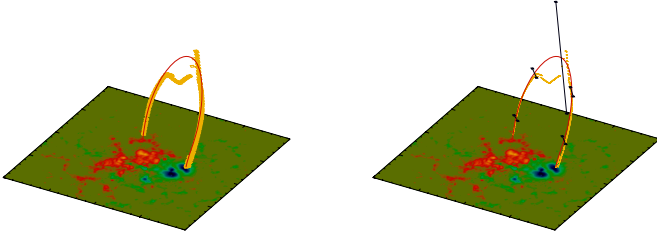
Figure 4.12: Magnetic stereoscopy of loop pair 0-0. Yellow points give the solution of the 3D reconstruction, the red line is the best fitting 3D magnetic field line. The right panel shows the reconstruction error bars at five points along the 3D magnetic field line (Feng et al. 2007b).

features, and the best fit 3D field line is marked by the red line. Generally the yellow dotted features form a reasonable outline of the 3D loop except the part near the loop top. As shown by Inhester (2006a), the positional error of the 3D curve reconstruction can be estimated by $w/(2\sin(\gamma/2))$, where γ is the angle between the local projection surface normals and w is the width of the loop cross section in the EUV image. The difference in heliographic longititude of the spacecraft between two days is about 17 degree. The angle γ can not be larger than this stereo base angle. The two normal unit vectors of the projection surfaces become almost parallel near the loop top. Hence the loop top is the most difficult part to be reconstructed by stereoscopy. Our reconstruction lies within the error bars shown in the right panel of Figure 4.12. Since the two STEREO spacecraft remain in the ecliptic the loop top will be the most uncertain part for any stereoscopic reconstruction of loops in the east-west orientation.

4.2 Stereoscopy of loops observed by EUVI/SECCHI

With the launch of NASA's STEREO mission in October 2006, a new dimension of solar coronal observations has been opened. For the first time, objects above the solar surface can be perceived in three dimensions by analysing the stereo image pairs observed with the SECCHI instruments onboard the STEREO spacecraft and without making a-priori assumptions about their shape. The two STEREO spacecraft orbit the Sun at approximately 1 AU near the ecliptic plane with a slowly increasing angle of about 45 degrees/year between STEREO A and STEREO B. Each spacecraft is equipped with, among other instruments, an EUV telescope (SECCHI/EUVI). For the objectives of the mission and more

STEREO probe	B	A
Helioc. dist. (AU)	1.068788	0.958071
Sun's app. rad. (arcsec)	897.866	1001.625
Longitude (degrees)	-4.277	7.524
Latitude (degrees)	-0.293	0.095

Table 4.2: STEREO spacecraft coordinates at the time of the observations. Spacecraft longitude and latitude are given in the Heliocentric Earth Ecliptic (HEE) coordinate system (Feng et al. 2007a).

details about the EUVI telescopes see Wuelser et al. (2004) and Howard et al. (2008).

The major building blocks of the solar corona are loops of magnetic flux which are outlined by emissions at, e.g., EUV wavelengths. In principle, the magnetic field in the lower corona can be derived from surface magnetograms by way of extrapolations (e.g. Wiegelmann 2007). However, missing boundary values and measurement errors may introduce considerable uncertainties in the extrapolation results so that there is an obvious need for an alternative three-dimensional determination of the coronal magnetic field geometry. Among other goals of the mission, this requirement has been one of the drivers for STEREO.

Attempts for a three-dimensional reconstruction of the coronal magnetic field from EUV observations have started long before STEREO data was available and date back more than a decade (Berton and Sakurai 1985, Kouchmy and Molodensky 1992). Here, we for the first time use two simultaneously observed EUVI images observed by the two STEREO probes and rigorously reconstruct loop shapes without any further assumption about their temporal or spatial behaviour from which earlier reconstructions employing consecutive images from a single spacecraft suffered. We compare the reconstruction results with field lines derived from linear force-free magnetic field models with variable α, the ratio of field-aligned current density to field strength (Seehafer 1978).

4.2.1   The data

For our reconstruction we used EUV images at $\lambda = 171$Å taken by the almost identical SECCHI/EUVI telescopes onboard the two STEREO spacecraft at 2007-06-08 03:21 UT when the well isolated active region NOAA 0960 was close to solar disk centre. The line $\lambda = 17.1$ nm is emitted by the Fe IX ion which forms at about 1.1 million K. At the time of these observations, the two STEREO spacecraft had a heliocentric separation of 11.807 degrees. The precise spacecraft positions at the time of the observation are listed in table 4.2.

For a comparison of our reconstruction with magnetic field lines we made use of a SOHO/MDI magnetogram taken only 9 seconds prior to the EUVI images. The active region is well isolated from neighbouring field sources so that an extrapolation of the surface field is possible. MDI, however, provides only the line-of-sight field component, which for this bipolar region close to the disk centre is almost identical to the radial field component on the solar surface. For this reason we can employ here only a linear force-free field model for the extrapolation of the magnetogram (Seehafer 1978).
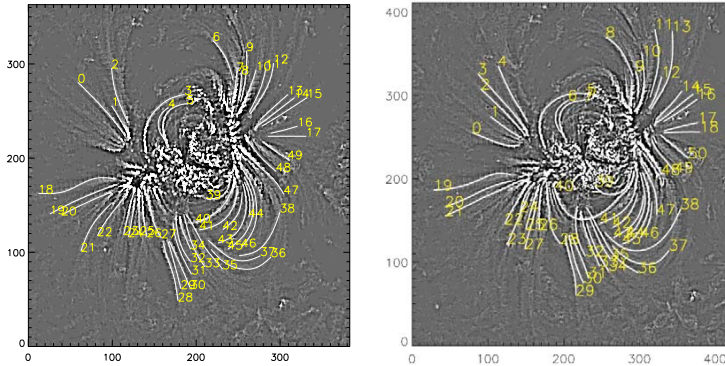
Figure 4.13: Contrast enhanced zoom of the EUVI images B (left) and A (right) of the active region NOAA 0960. Heliographic north is upward. The axes are scaled according to the image pixel size. Individual loop structures are emphasized by white curves and enumerated. Equal numbers do not imply a correspondence across the images (Feng et al. 2007a).

4.2.2   The reconstruction

The first step in the stereoscopic reconstruction scheme is the isolation and identification of individual loops in each of the EUV images. In Figure 4.13 we show the portion of the EUV images containing the active region. The EUV structures were contrast enhanced by an unsharp mask filter. Next, individual loop structures were detected by a loop segmentation program described in Chapter 3. This program detects individual bright loops in an image by treating them as elongated intensity ridges (Inhester et al. 2008). For identification, the loop curves were enumerated. These assignments, e.g. a number l_A for a loop curve in image A, were made independently in each image.

To establish correspondences of projections $l_A \rightleftarrows l_B$ of the same loop across the images is the hardest part in the stereoscopy procedure. For isolated loops they can sometimes be guessed by visual comparison of the image pair. Also, some guidance is provided by matching constraints which corresponding pairs of loop projections have to obey (Inhester 2006a). Often, however, the visual comparison of loop structures does not yield unique correspondences. To disentangle the typically crowded active region loop ensembles we have developed a systematic scheme which determines correspondences with the help of magnetic field model calculations (Wiegelmann and Inhester 2006, Feng et al. 2007b). The idea is to find three dimensional field lines from a more or less accurate model of the active region magnetic field as a first approximation to the final loops whose projections are close to the loop projections identified in the images from spacecraft A and B. If a field line can be found with projections sufficiently close to a loop in both images, this is strong evidence that these loop curves represent projections of the same three-dimensional loop.

The probability of a correspondence between a pair (l_A, l_B) of loop curves in image
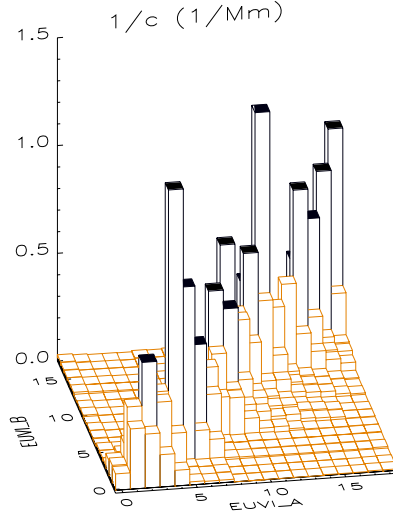
Figure 4.14: Proximity of loops identified in images A and B in figure 4.13. The proximity is expressed by the inverse of a distance measure C (see text). The loops from image A and B are arranged along axes 'EUVI_A' and 'EUVI_B' according to their respective identification number l_A and l_B. For each pair (l_A, l_B) the inverse of C is displayed by a column at the location of the loop pair in this matrix representation. Columns exceeding 0.5 Mm^{-1} have a black top. Here, only loops from the northern half of the active region were considered (Feng et al. 2007a).

A and B is measured by $C = \frac{1}{2}\min_b(C_{l_A}(b) + C_{l_B}(b))$ as introduced in the section of loop correspondence from two TRACE images. Here, the set of possible field lines b comprised all possible foot point locations and a wide range of α values from -0.0156 to +0.0156 Mm^{-1} and only serve as a mean to establish the correspondence, they are not intended to represent a consistent field model of the active region. The linear force-free field model used is only consistent if α is a global constant. Strictly speaking, the field lines $l_{\min}$ for which C attains the minimum are each from a different field line model as α turned out to differ for each loop pair.

In Figure 4.14 the inverse of C is shown for the loops in the northern half of the active region, $l_A = 0$ to 18 and $l_B = 0$ to 17. Some few loop combinations show a clearly enhanced $1/C$ and are thus much more probable than the majority of combinations (l_A, l_B). We accepted for a reconstruction only loop pairs with a value of C below 2 Mm. This corresponds to an average distance between the field line projection and the loop curves in each image of 2 pixels or less. When more than one combination was possible for one loop, the most probable one was taken such that each loop receives no more than one partner and the sum of C of all selected correspondences was minimised (Wiegelmann and Inhester 2006). In all, 20 pairs from Figure 4.13 could thus be identified.
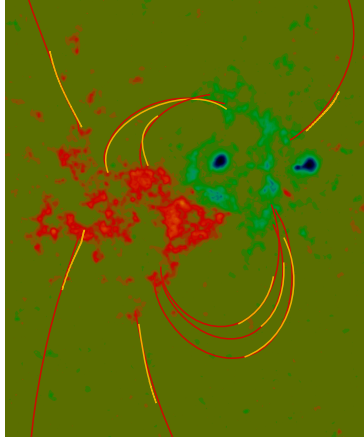
Figure 4.15: Vertical View of the three-dimensional reconstruction results from a view-point within a degree from the STEREO A spacecraft. Heliographic north is upward. The reconstructed loop sections are drawn in yellow, the closest fit field lines in red. The loop pairs (l_A, l_B) drawn are: 4-2, 12-12, 5-3, 7-5 (northward part of this AR) and 45-45, 44-43, 42-42, 24-23, 30-29 (southward part) (Feng et al. 2007a).
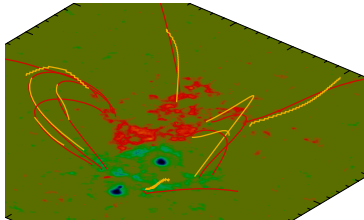
Figure 4.16: Same as Figure 4.15, but seen from a view point NE of the active region. Heliographic north points to the lower left corner. The SECCHI instruments observed from approximately above (Feng et al. 2007a).

The last step is the stereoscopic reconstruction of the three-dimensional loop from each accepted pair (l_A, l_B). This purely geometrical step often yields multiple solutions (Inhester 2006a). They were discarded by retaining only the three-dimensional reconstruction closest to the best fit field line $l_{\min}$.

4.2.3   Results

In Figures 4.15 and 4.16 we present two views of a set of reconstructed loops. Figure 4.15 shows the reconstructed loops (yellow) and the associated closest fit field lines(red) ob-
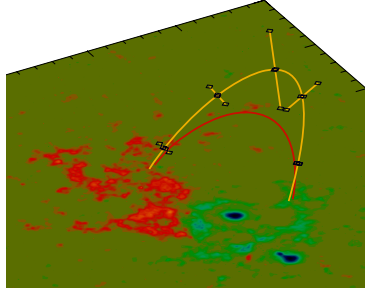
Figure 4.17: Example of a reconstructed loop with error estimates. The reconstruction is shown in yellow along with error bars. The associated best-fit linear force-free field line (red curve) is much lower in height (Feng et al. 2007a).

Loop pair i_A, i_B	$\|\alpha\|$ $(10^{-3} Mm^{-1})$	height (Mm)	length (Mm)
5, 3	1.8	71.9	229
7, 5	8.3	20.6	105
45,45	2.3	58.2	253
44,43	2.8	27.3	188
42,42	2.8	57.2	210

Table 4.3: Best fit field line parameters for a representative list of closed loops of active region NOAA 0960 (Feng et al. 2007a).

tained by extrapolation from a position within a degree from the STEREO A spacecraft. As expected, loops and field lines agree relatively well from this perspective because they were chosen to be close in this projection. Figure 4.16 therefore provides a completely different view of the active region. This view shows that most of the loops cannot easily be approximated by planar curve segments. This geometrical simplification was often used for loop reconstructions in the past because a more involved shape could only rarely be resolved from previous observations. This figure also reveals deviations between the loops and field lines. E.g., the loops on presumably open field lines appear to be more strongly curved than the corresponding field lines from the extrapolation.

We attribute this disagreement to a deficiency of the linear force-free field line extrapolation. For the closed field lines, the best fit $|\alpha|$ values derived above fell in the range from 1.8 to 8.3 10^{-3} Mm^{-1} (see table 4.3). For the open field lines, these values turned out to be smaller in magnitude, with values $|\alpha|$ <2.5 10^{-3} Mm^{-1}. As α is a global constant for the linear force-free field model, the influence of the stronger currents on the closed active-region field lines is not accounted for on the open field lines. This may explain why the open field lines were calculated with less curvature than the corresponding stereoscopically reconstructed loops.

The loop reconstruction is also prone to errors, however. These may occur whenever a projected loop section in the images are directed tangentially to an epipolar line (Inhester

2006a). For the viewing geometry of our observations, epipolar lines are nearly horizontal in the images and the critical part for closed, E-W orientated loops therefore lies more or less near their apex. Also the open loop structures 16-19 in image B and 17-20 in image A (see Figure 4.13) suffer from this problem as they are orientated almost entirely horizontally in the images. We have therefore not attempted to reconstruct them even though a correspondence could well be identified.

In Figure 4.17 we display the reconstruction of loop (5,3) (yellow curve) which shows by far the largest deviation to its best fit linear force-free field line (red curve). For most other loops, this discrepancy is much less although the agreement is rarely perfect. For some points along the loop (5,3), we also show error bars which represent the geometrical reconstruction error when the uncertainty for the loop projection in the images is assumed to be 1.5 pixels. In this case, the height of the loop top turns out to be ∼ 1.5 times above that of the corresponding field line. This field line (the first entry in table 4.3) again shows a relatively small value $|\alpha|$. Since this α value gave the best fit of linear force-free field lines to the loop projection in the images, we conclude that the linear force-free assumption is often not adequate (*c.f. Wiegelmann et al. 2005b*).

4.2.4   Discussion and outlook

We demonstrated that EUV data from the new STEREO spacecraft allows for the first time to make a reliable stereoscopic reconstruction of the spatial distribution of hot, magnetically confined coronal plasma and, by inference, provide a full three dimensional view of the arrangement of coronal field lines. We found that linear force-free field models are helpful to establish correspondences between the loops observed in the STEREO image pairs. The field lines from these linear force-free models need not be physical but only serve as a first order approximation to the final loops. Realistic magnetic field models of the corona will have to be judged by their capability to yield field lines in agreement with the stereoscopically reconstructed loops. Our scheme to determine correspondences will become even more valuable when the stereo base angle grows and loop structures become more difficult to be identified in the image pairs.

The reconstructions will also allow more precise analyses of emissions from loops. The observed brightness of EUV loops is, e.g., strongly modified by the cosine of the angle between the line of sight and the loop's local tangent. This may, besides other effects, contribute to the enhanced EUV brightness of the lower loop segments commonly observed on the solar disk: these loop segments close to the loop's foot points are more aligned with the radial direction and they make a small angle with the view direction. This may cause them to appear brighter than the loop top which is viewed at more or less right angles.

Other applications have been proposed (Aschwanden 2005a, Aschwanden et al. 2008b). e.g., the amount of twist of a reconstructed loop indicates how close the flux tube is to a kink instability. Török et al. (2004) found a threshold of about 3.5π in numerical simulations for the twist $\Phi = LB_\phi/rB_\parallel$. Here L is the length of the flux tube, $B_\parallel$ the toroidal field along its axis and $B_\phi \simeq \alpha B_\parallel r/2$ the poloidal field at a radius r from the flux tube centre. In some cases it may be possible to resolve the number of turns n which a field line makes about the flux tube centre from stereoscopic reconstruction and thus to determine the twist from $\Phi = 2\pi n$. Likewise, the twist is also related to α and L by $\Phi = \alpha L/2$. For the active

region observed here, table 4.3 gives values of $\Phi < 0.5$ well below the kink instability threshold.

Another perspective for stereoscopic loop reconstruction is the analysis of loop oscillations from a series of image pairs. The reconstructed loops will allow us to determine the transverse polarisation of these oscillations (Aschwanden et al. 2002, Wang and Solanki 2004). Since the coronal magnetic field has a complicated geometry without symmetries, the frequency of these oscillations will significantly depend on this polarisation. Note that these phenomena are invisible in the magnetic surface data and therefore cannot be retrieved from field extrapolations, which in addition require a stationary magnetic field.

5 Stereoscopic reconstruction of polar plumes

We have reconstructed the 3D geometry of the polar plumes by analysing the simultaneously observed EUVI images for two data sets, April 7 and June 1 in 2007. Preliminary results of the 3D plume coordinates obtained on one of the studied days, April 7, are shown in Curdt et al. (2008). In this chapter which is mainly based on the paper of Feng et al. (2009), we describe an improved method of stereoscopic reconstruction in detail. Furthermore, based on the 3D coordinates, we have calculated the inclination of plumes to the LOS of the Earth and to their local radial direction for both date sets. We have compared the 3D orientation of plumes with the local direction of a dipole magnetic field. The dipole field is the lowest order approximation of the coronal magnetic field at times of low solar activity when the plume observations were made. Additionally, we have calculated the footpoint positions of the reconstructed plumes and projected them onto the EUVI images to investigate their relationship to EUV bright points. For the first data set, *SOHO*/SUMER observations were also available. We have used them to determine physical parameters, including the temperature, density and LOS (Line-Of-Sight) Doppler shift. By projecting a 3D plume onto the SUMER density map, its density scale height could be calculated. The temperature corresponding to this scale height and the temperature derived spectroscopically from SUMER has been compared.

5.1 The data

STEREO was launched somewhat after the solar activity minimum which provides us with good opportunities to observe polar plumes. We selected two data sets for this study, one in the south polar cap on 2007-04-07 22:01:17 UTC and the other in the north polar cap on 2007-06-01 00:09:00 UTC. Both were recorded by the two almost identical SECCHI/EUVI telescopes at $\lambda = 171$ Å corresponding to a formation temperature of roughly 1 MK. The position information of both spacecraft, the exposure time and the compression mode are given in Table 5.1.

On April 7, the separation of the two spacecraft was 3.6°. The HEEQ (Heliocentric Earth EQuatorial coordinate system; Thompson (2006)) latitudes of the two spacecraft were well below the Sun's equatorial plane. At that time the solar south pole was tilted towards the spacecraft which was very appropriate for observing as much as possible of the southern polar area. In addition, to improve the signal to noise ratio of the EUVI images, a longer exposure time and a smaller compression were applied. The image pairs chosen in this work have 20 s exposure time, compared to the normal exposure time of 2

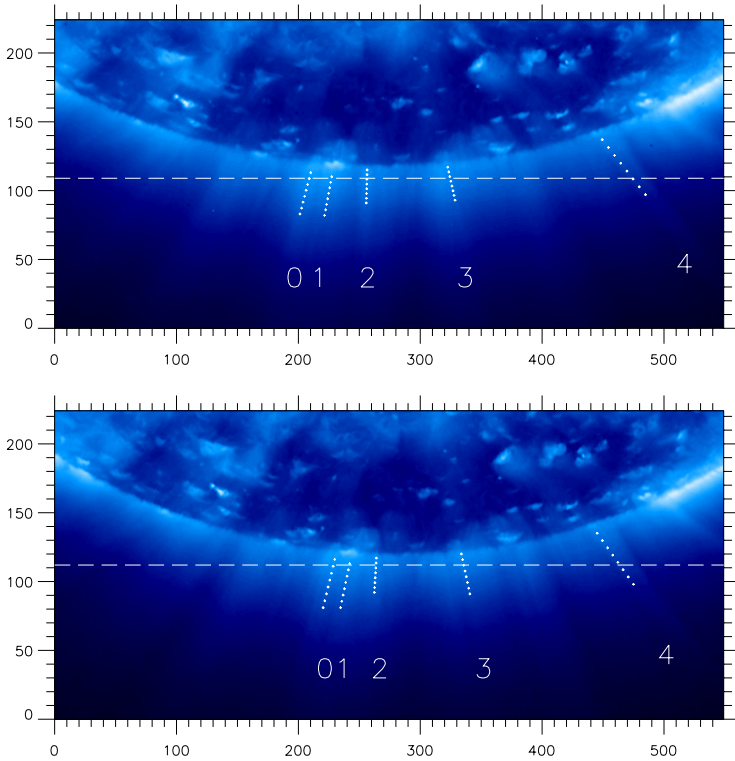Figure 5.1: The south polar cap observed on 2007-04-07 22:01:17 UTC at λ = 17.1 nm by EUVI A (upper) and B (bottom). The corresponding epipolar lines are approximated by the two long-dashed lines. The dotted lines are the identified plumes (see Section 3 for details) (Feng et al. 2009).
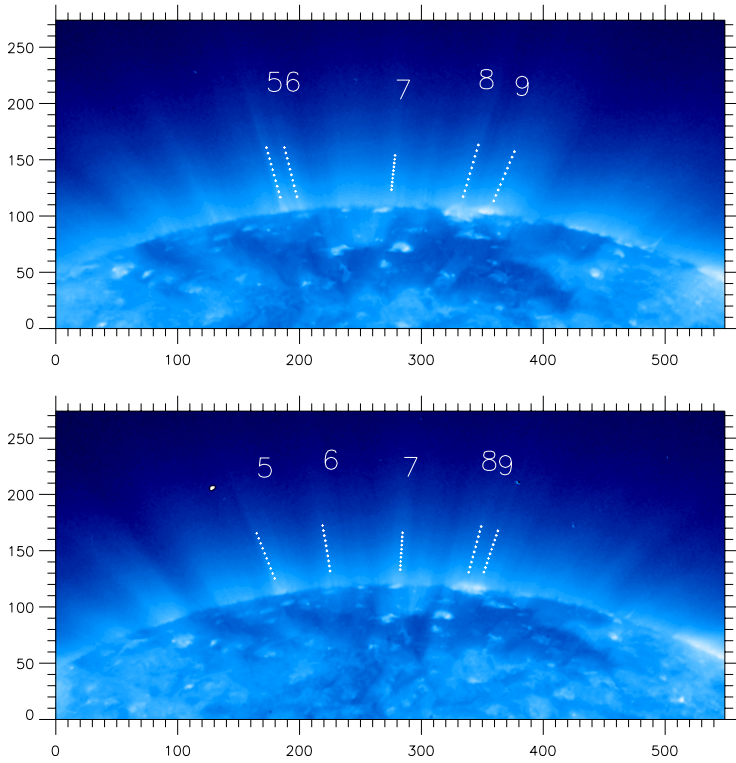
Figure 5.2: The north polar cap observed at 2007-06-01 00:09:00 UTC by EUVI A (upper) and B (bottom) (Feng et al. 2009).

Date	April 7, 2007		June 1, 2007	
STEREO spacecraft	B	A	B	A
Sun-Earth. dist.(d/au)	1.0277777	0.9640101	1.0647322	0.95860281
Sun's app. rad.($R_\odot$/")	933.69200	995.45200	901.28300	1000.3757
HEEQ longitude(φ/°)	-0.918945	2.697643	-3.6847666	6.7788499
HEEQ latitude(θ/°)	-6.404608	-5.999570	-1.4801556	0.2276848
resolution(Δx/("/pix))	1.5900000	1.5877700	1.5900000	1.5877740
Separation (α/°)	3.62		10.6	
Exposure time (T/s)	20		16	
Compression mode	ICER4		ICER4	

Table 5.1: The positions of the two *STEREO* spacecraft given in HEEQ coordinate system, exposure time of the observation and compression mode of the recorded data on 2007-04-07 22:01:17 UTC and on 2007-06-01 00:09:00 UTC.

s. The images were compressed by the format ICER (a wavelet-based image compression file format) 4 which requires two times the storage of images obtained after applying the usual ICER 6 compression used ordinarily for EUVI images at 171 Å . In Figure 5.1, the southern polar cap in both EUVI views is presented with five plume pairs marked by numbers below them.

In parallel, SUMER which was introduced in § 1.1.1.3 in Chapter 2 performed a raster scan from 2007-04-07 01:01 UTC to 2007-04-08 12:19 UTC in the southern corona. The scan direction was from solar west to east. To combine with 3D plume geometry, we derived the electron density map from the emission line pair Mg IX at 70.6 nm and 75.0 nm, the electron temperature map from line pair Si VIII at 144.0 nm and 144.6 nm, and the LOS Doppler shift map from the O VI at 103.2 nm and 103.8 nm. The details of the SUMER observations can be found in Curdt et al. (2008).

The second analysed EUVI data set was recorded on June 1, when the separation angle between the spacecraft was 10.6°. This increased separation angle reduced the reconstruction uncertainty considerably. At the same time, this separation angle is still sufficiently small so that the correspondence between individual plumes in both EUVI images can still be unambiguously identified. The related spacecraft positions, observation and compression parameters are listed on Table 5.1.

5.2 The reconstruction

To reconstruct the 3D geometry of the plume, the first step is to identify the points along the plume axis and associate the corresponding plume pair in the two simultaneous EUVI images. To establish this correlation between the plumes, we extracted from each image the intensity profiles along corresponding epipolar lines (Inhester 2006a) in both images. Figure 5.3 gives an example for the April 7 data. The intensity distributions along the corresponding epipolar lines, which are approximated by the two long-dashed lines in Figure 5.1, were smoothed by taking the average over three pixels. The plume centers were selected according to the local intensity maxima and marked by the corresponding numbers.
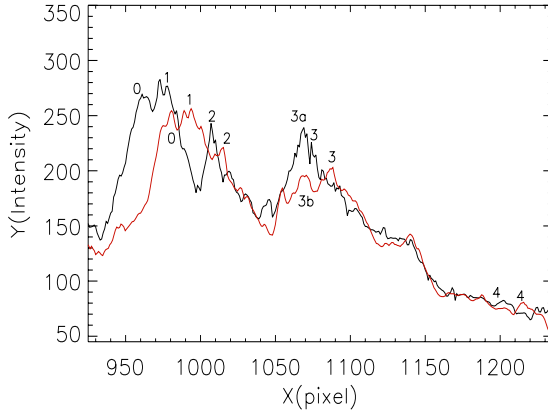
Figure 5.3: The intensity distributions smoothed over three pixels along the corresponding epipolar lines in each EUVI image observed in April. The black and red lines are for EUVI A and B, respectively. The x coordinate of the solar center in A and B lies at 1020.62 and 1035.52 in units of pixels, respectively. The numbers refer to the plumes in Figure 5.1 (Feng et al. 2009).
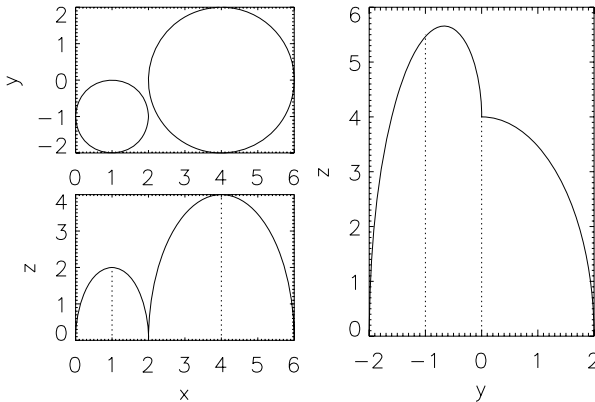
Figure 5.4: A schematic explanation of why a different number of peaks might be visible from different perspectives. The upper left panel shows the assumed cross section of two plumes. The lower left panel displays the LOS integrated intensity as seen in the y-direction, The right panel exhibits the intensity as seen along the x-direction (Feng et al. 2009).

For plumes 0, 1, 2 and 4 the association is clear. However for plume 3 there is some uncertainty due to the complicated superposition of probably several plumes along the line of sight. The intensity distribution around plume 3 in EUVI A is dominated by one prominent peak (marked as 3a in Figure 5.3) with a smaller peak (3) on the right side, whereas in EUVI B two distinct peaks (3b and 3) appear. There are four possible ways to associate the two plume signatures in the two images. Trying all combinations, we judged their likelihood from the inclination of the resulting 3D plumes. When a point on the 3D plume leaves from its footpoint on the solar surface, its distance to the solar rotation axis should increase as well. The second criterion is that the angle between the plume and the local meridian plane passing through the plume footpoint should be as small as possible (see Figure 5.7). In this way, we find that the combination of peak 3 in image A and peak 3 in image B gave the most reasonable result. In Figure 5.4, we sketch the situation which we think yields the different peaks in the two images for plume 3. Here we assumed a circular shape and a uniform intensity distribution within the cross section of two plumes of different radii. Figure 5.4 shows the resulting intensity distributions from two different perspectives.

Finally, the axes of the five plumes were traced by repeating the procedure for each plume at eight different heights above the solar limb. Since in EUV images plumes are shaped as nearly straight lines, each plume axis was approximated by a linear function and plotted as a dotted line in Figure 5.1. The identification of the plumes for the second data set observed in June 2007 is similar and the results are overplotted on the corresponding EUVI A and B images shown in Figure 5.2.

From these linear 2D plume positions in both EUVI images, we reconstruct the 3D plume locations based on epipolar geometry in the frame of the HEEQ coordinate system. The reconstructed plumes are straight lines in 3D. In order to obtain an error estimate, we here assume a maximal uncertainty of 3 Mm, corresponding to an positional error in the images of 4.3″ in EUVI A and 4.0″ in EUVI B, in the estimated plume position along the epipolar line due to the three-pixel smoothing as mentioned before. We shall see in the next section that this uncertainty is propagated to an analogous uncertainty of the stereoscopic reconstruction.

5.3   Results

We present the different perspectives of plumes for two data sets derived from stereoscopic reconstructions in Section 5.3.1, as well as the plume orientation analyses, plume width calculations and the relationship between plumes and EUV bright points. In section 5.3.2 the results obtained by combining stereoscopic reconstructions and the plume density and temperature deduced from SUMER observations are shown. The density scale height and its corresponding temperature are calculated by assuming the plume in our study is in hydrostatic equilibrium.

5.3.1 Stereoscopic results

5.3.1.1 Side view and top view

In Figure 5.5, we present a view of the 3D placement and direction of polar plumes from a perspective that is 90° to the left and 20° up compared to the view direction of *STEREO A*. Of the five reconstructed plumes in April, three are in front of the solar limb as seen from *STEREO A*, the other two are behind the limb. For the data set in June, only plume 6 lies in front of solar limbs as seen by both spacecraft. The black solid lines indicate the reconstruction uncertainties calculated following the methods described in Chapter 2 by assuming a maximal 3 Mm variation of the plume axis position. The resulting uncertainties are directed mainly half way between the view directions of *STEREO A* and *B*, and are considerable for the data set in April since the spacecraft separation angle was small at that time. With the increased separation angle in June, the uncertainties are greatly reduced for the same assumption of 3 Mm uncertainty in 2D.

The polar view of the ten plumes projected onto the solar equatorial plane is shown in Figure 5.6. Larger symbols indicates the plume positions at greater heights above the solar surface. All ten plumes oriented close to their local meridian planes and inclined away from the rotation axis.

5.3.1.2 Plume's orientation analysis

In Figure 5.7 a sketch of the 3D plume geometry is presented to analyse the plume orientation. The relevant results is shown in Table 5.2. Concerning the latitudes and longitudes of the plume footpoints, all the plumes are located within a latitude cone of 20° around the pole. For a better estimate of the outflow speeds along the plumes from FUV (Far Ultraviolet)/ EUV spectral observations by SUMER and UVCS on board SOHO, the angle β between the LOS from the Earth and the plumes' orientation were calculated. They range from 65.7° to 128.6° for plume 3 and 8 being almost perpendicular to the view direction of the Earth. For the angle γ off the meridian plane, we found for all ten plumes a maximum departure of 14.2°. This indicates that the magnetic azimuthal component B_φ was very small on the polar cap during the time of our observations. The deviation of the plume projection to the solar radial direction $\widehat{\mathbf{e_r}}$ is calculated and represented by the angle ψ. This angle in general becomes larger with increasing distance of the footpoint from the pole as shown in the upper panel of Figure 5.8. This means that the plumes do not converge to the solar center, which is consistent with the 2D results (Deforest et al. 1997, Fisher and Guhathakurta 1995). They found the plumes/rays appear to diverge radially from a point between the solar center and the respective pole.

In addition, we compared the 3D plume structure which outlines the coronal magnetic field with the assumption of a dipole with its axis along the solar rotation axis. In this case the plume's inclination angle i and the footpoint latitude λ should be related by $\tan(i) = 2\tan(\lambda)$ (see Page 50 of Fowler (2005) and also §2.2.3 in Chapter 2). From the related two rows in Table 5.2 we find that this relation is not well satisfied for each plume and $|\tan(i)| < 2|\tan(\lambda)|$ in all cases. Therefore the magnetic field is not well approximated by this dipole field and is more horizontal, as also shown in the middle panel of Figure 5.8. In the bottom panel we check how much plumes deviate from the dipole field and how this deviation changes with the latitude. We find that at lower latitudes, the plumes are more
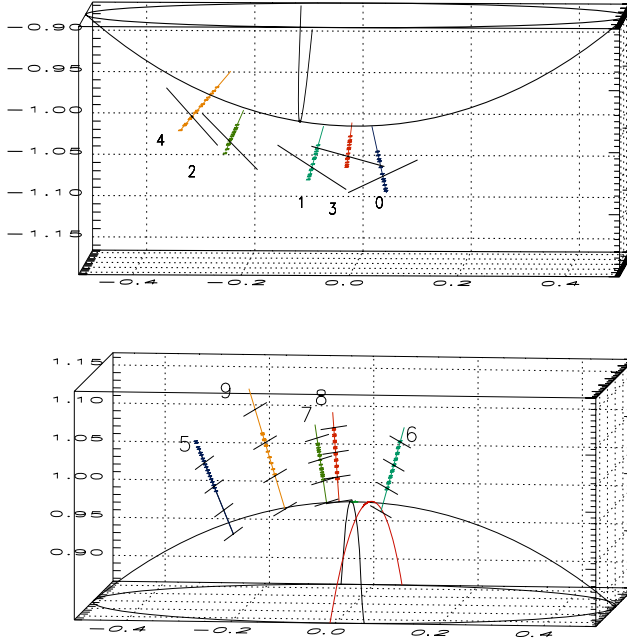
Figure 5.5: Side view of the south polar cap on April 7 (upper panel) and the north polar cap on June 1 (lower panel): a perspective that is 90° to the left, and 20° up relative to the view direction of *STEREO* A. The coordinates x and y range from $-0.5\ R_\odot$ to $0.5\ R_\odot$, z ranges from $-0.87\ R_\odot$ to $-1.17\ R_\odot$ for the south polar cap and from $0.87\ R_\odot$ to $1.17\ R_\odot$ for the north cap. The long curve is a circular segment crossing the pole. The shorter curves are the solar limbs as seen from the two spacecraft (black from *STEREO A* and red from *STEREO B*. The dotted points are the reconstructed 3D plume axes. The solid lines are the extrapolations back to $r = 1\ R_\odot$. The uncertainties are indicated by the black solid lines which are perpendicular to the plume directions in 3D (Feng et al. 2009).
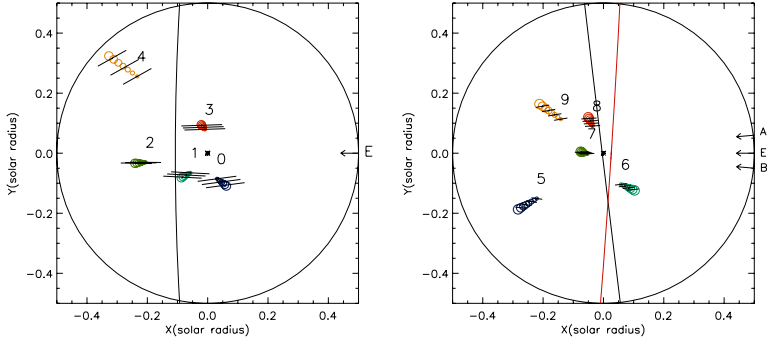
Figure 5.6: Top view: projections of the reconstructed 3D plumes onto the solar equatorial plane in April (left) and June (right) together with the associated uncertainties (black solid lines). For each plume, the size of the circle is proportional to the distance of the 3D point to the solar surface. In the left panel, the solar limb as seen from the Earth is indicated by the curve near the pole which is marked by a star symbol. The view direction from the Earth indicated by the arrow marked E at the right edge of the figure is also shown. In the right panel, the solar limb as seen from *STEREO A* is indicated by a black curve and seen from *STEREO B* is indicated in red. The view directions of the two spacecraft and the Earth are marked on the right side (Feng et al. 2009).

| Date	April 7					June 1				
Plume	0	1	2	3	4	5	6	7	8	9
$\lambda/°$	-84.7	-85.0	-78.0	-85.4	-69.7	74.5	83.2	86.9	84.4	79.6
$\varphi/°$	-69.9	-131.3	-171.6	96.9	132.5	-145.6	-60.7	-177.9	111.7	141.3
$\beta/°$	65.7	106.7	117.4	94.4	128.6	118.8	68.6	103.2	97.6	114.8
$\gamma/°$	12.2	-8.61	-1.70	8.67	9.85	-2.25	14.2	-4.48	1.10	1.62
$\psi/°$	-15.0	-19.9	-21.9	-10.4	-37.0	17.4	13.2	9.35	10.4	19.6
$\tan(i)$	-3.73	-2.77	-2.52	-5.45	-1.32	3.19	4.26	6.07	5.43	2.80
$2\tan(\lambda)$	-21.9	-22.3	-9.40	-24.9	-5.42	7.20	16.7	37.5	20.4	10.9
$(i-i')/°$	12.4	17.3	15.8	8.10	26.5	-9.49	-9.77	-7.82	-7.59	-14.4

Table 5.2: Footpoint position and inclination of the reconstructed plumes on April 7 and on June 1. The relevant angle symbols are the same as defined in Figure 5.7. The first two rows are the footpoint latitudes and longitudes of the plumes. β gives the angle between a plume orientation and the LOS direction of the Earth. γ measures how much a plume deviates from the local meridian plane and its sign depends on the sign of $\widehat{\mathbf{e}}_{plume}{}^T \cdot \widehat{\mathbf{e}}_{\varphi}$. ψ is the complementary angle of magnetic inclination i and its sign is the same as the sign of $\widehat{\mathbf{e}}_{plume}{}^T \cdot \widehat{\mathbf{e}}_{\theta}$. All angles are given in units of degrees. The last three rows are the tangent of magnetic inclination, two times the tangent of the latitude, the difference of the magnetic inclination i with the dipole magnetic inclination i' corresponding to $\arctan(2\tan(\lambda))$.
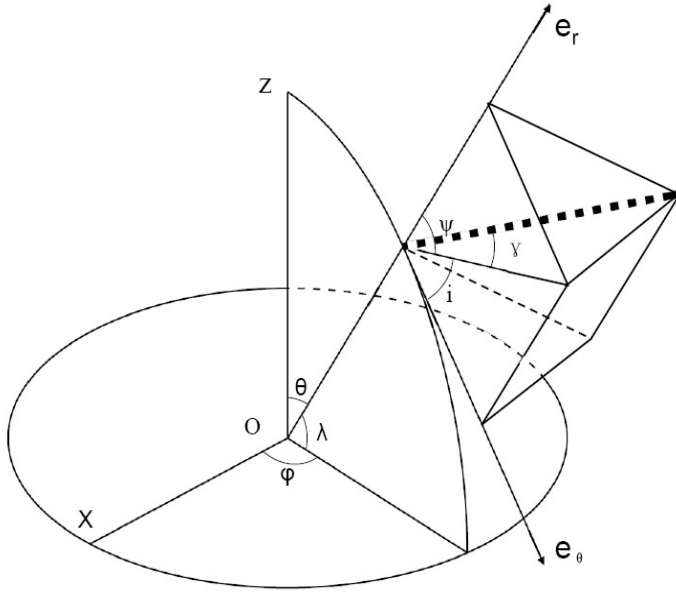
Figure 5.7: A schematic illustration of 3D plume geometry in the HEEQ coordinate sys-
tem. The 3D plume is indicated by the thick dashed line started from the solar surface.
The plume footpoint is parameterized with the longitude φ and latitude λ (the colatitude
is denoted as θ). We establish the local coordinate framed by $\widehat{\mathbf{e_r}}$, $\widehat{\mathbf{e}_\theta}$ and $\widehat{\mathbf{e}_\varphi}$ (for clearness
of this figure $\widehat{\mathbf{e}_\varphi}$ is not shown) which originates from the footpoint. The projection of the
3D plume onto the local meridian plane spanned by $\widehat{\mathbf{e_r}}$ and $\widehat{\mathbf{e}_\theta}$ makes two angles: ψ is the
angle between the projection and $\widehat{\mathbf{e_r}}$, i is the angle between the projection and $\widehat{\mathbf{e}_\theta}$ and is
the so-called magnetic inclination. γ is the angle between the 3D plume and its projection
mentioned above (Feng et al. 2009).

horizontal than the dipole field. This was already noted by Saito (1965) who used a bar magnet of finite length to fit the plumes/rays at different distances from the Sun observed during a solar eclipse. Banaszkiewicz et al. (1998) described a simple analytic model for the magnetic field at solar activity minimum. A dipole and a quadruple field were added to construct the coronal magnetic field in the solar minimum. The reconstructed 3D plumes could be used as a reference in the polar region to test other, more sophisticated magnetic field models (Neukirch 1995, Ruan et al. 2008).

5.3.1.3   Plume's width analysis

Besides the orientation, we calculated the width of the isolated and prominent plume 4 from viewpoints of EUVI A and B by fitting the intensity profiles around this plume with Gaussian distributions. For the plume width w at a given height h we use the definition of Aschwanden et al. (2008c)

$$w(h) = \frac{\int_{x_{b1}}^{x_{b2}} [I(h, x) - b(h, x)] dx}{max[I(h, x) - b(h, x)]},$$ (5.1)

where x_{b1} and x_{b2} are the x coordinates of the two plume boundary points determined by the two local minima on either side of the plume (Figure 5.9). Here, $b(h, x)$ is the linearly varying background intensity between x_{b1} and x_{b2}. $I(h, x) - b(h, x)$ then denotes the background subtracted plume intensity distribution as a function of height h. The intensities associated with this plume along two epipolar lines are shown in Figure 5.9 as an example. By using the epipolar geometry, we identify the corresponding plume point in two images and calculate the plume width from EUVI A and EUVI B, respectively. Subsequently the plume widths along the corresponding epipolar lines are transformed to the widths perpendicular to the plume direction within the frame of the epipolar geometry.

For this plume, we found from both viewpoints that the width very slightly decreases by around 10 % in the height range from 20 Mm to 90 Mm in 3D. The mean width and standard deviation from EUVI B is 14.0 ± 0.86 Mm, while from A it is 12.7 ± 1.22 Mm. The two widths differ by less than 1.5σ so that this measurement is consistent with a circular plume cross section. However, given the small separation angle, a more curtain-like structure cannot be ruled out either. More isolated and prominent plumes need to be analysed at large separation angles to come to a conclusion regarding the cross section of the plumes. It should be mentioned here that we have only considered the circular or simple noncircular cross sections for plumes and we have not taken into account the substructure that is known to exist within plumes (e.g., DeForest 2007, Deforest et al. 1997). Unresolved morphology can mimic a surprising range of other effects including modifying the inferred density (both from photometric density estimates and from line-ratio estimates, in different ways for the two techniques) and the observed scale height.

5.3.1.4   Plume and EUV bright points

To investigate the relationship between plumes and EUV bright points, we projected the reconstructed 3D plumes onto two EUVI images. For the data in April, given the small separation angle, only the projection onto EUVI A is plotted in Figure 5.10. Only plume 1 is associated with a bright point. Plumes 0 and 3 were rooted in the brighter part of the
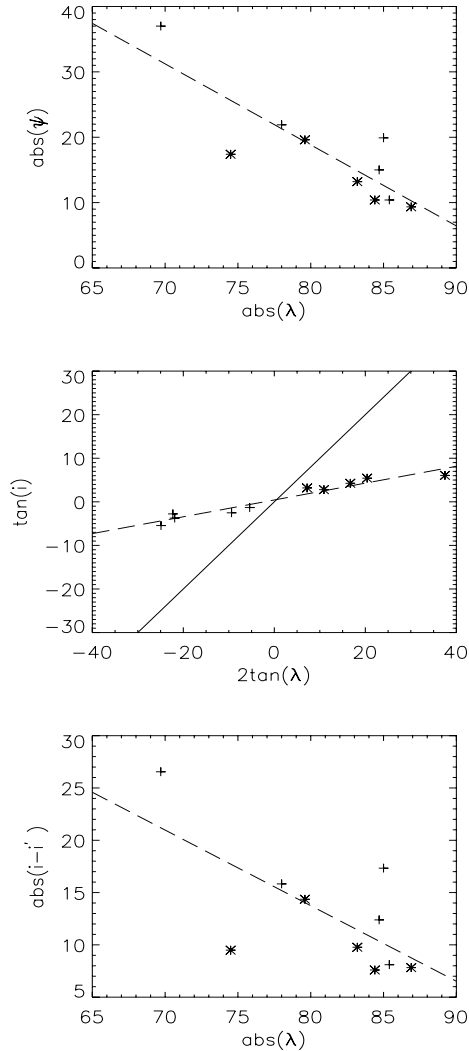
Figure 5.8: Upper: the absolute value of ψ as a function of the absolute value of λ. The plus signs are for the data in April and star signs for the data in June. Middle: the plot of $\tan(i)$ versus $2\tan(\lambda)$. The solid line corresponds to $\tan(i) = 2\tan(\lambda)$. Bottom: The difference of the magnetic inclination i from the dipole field inclination i' as a function of the absolute latitude (Feng et al. 2009).
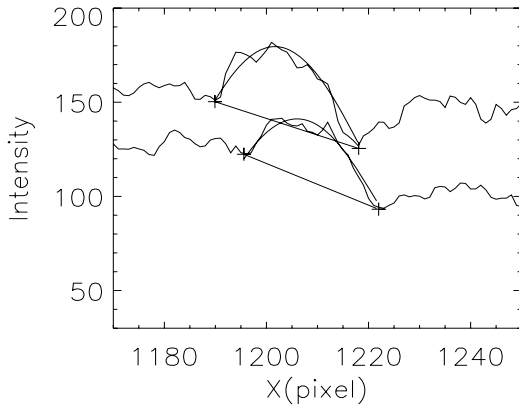
Figure 5.9: The intensity profile around plume 4 along two epipolar lines in EUVI B. On each line the two plus signs indicated the plume boundary and the connected straight line shows the plume background. Within the range between the two boundary points, the intensity is fit by the Gaussian distribution (Feng et al. 2009).
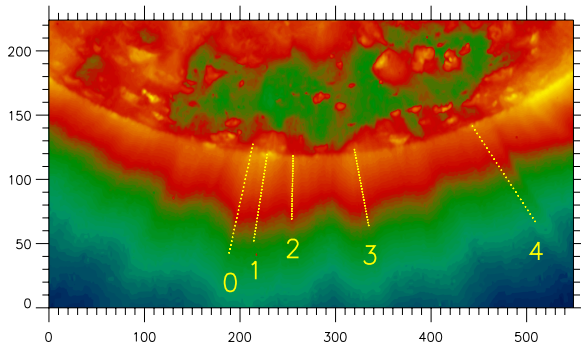
Figure 5.10: Projection of the 3D plumes onto the image of EUVI A observed on April 7 (Feng et al. 2009).
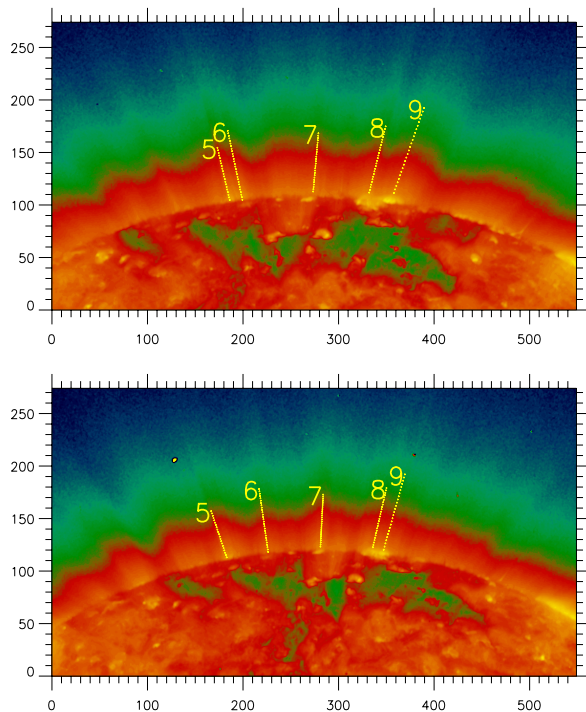
Figure 5.11: Projections of the 3D plumes on EUVI A and B recorded on June 1 (Feng et al. 2009).

coronal hole, but not on a bright point. Considering the evolution of polar plumes (Wang 1998, Raouafi et al. 2008), plumes 0 and 3 were observed perhaps in the decaying phase in which the bright points have already disappeared but the two plumes were still visible. For the big bright point close to the limb between plumes 3 and 4, we tried to find a plume pair but none of the possible peaks in the two plume intensity profiles (e.g., Figure 5.3) produced a reasonable result with a footpoint close to this bright point and an orientation roughly along the diverging direction of the magnetic field around the pole.

For the data in June, Figures 5.5 and 5.6 reveal that of the five reconstructed plumes only plume 6 lies in front of the solar limbs as seen by *STEREO A* and *B*, the footpoints of the other four are hidden by the limb. By projecting the reconstructed plumes onto two simultaneous EUVI images (see Figure 5.11) and taking into account Figures 5.5 and 5.6, the spatial relationship between plumes and bright points can be inferred. The plume in front of both limbs, that is, plume 6 could be associated with a very faint bright point. Plume 7 presents a nice example of the importance of having 3D information when

associating plumes with bright points. If we consider only EUVI B, then plume 7 seems to be related to a bright point right in front of the limb. However, when we check both Figures 5.5 and 5.6 we find this plume is rooted just behind the limbs seen by EUVI A and B. Therefore, the association to the bright point near the limb is probably spurious. For plumes 8 and 9, it is difficult to reach a firm conclusion. We see two bright points in both images close to the plume roots. The association is possible if the bright point relevant to plume 8 is big enough and the height of the bright point relevant to plume 9 is large enough that it could be seen from EUVI A and B, even though it is behind the limb.

5.3.2 Results combining stereoscopy and SUMER observations

For the data set in April, SUMER observations are available. To obtain the electron density and electron temperature along a plume, we assume that the geometry of a plume does not change during its evolution, and then project it onto the density and temperature maps deduced from the line ratio of the Mg ix line pair and the Si viii line pair, respectively (Wilhelm 2006, Wilhelm et al. 2009). Consistent with the previous results, the plumes are denser and cooler than the interplume regions. The Doppler shift measurements, we deduced from the O vi lines based on the method outlined in Wilhelm et al. (1998).

SUMER scanned the relevant region from April 7 01:01 UTC to April 8 12:19 UTC continuously moving from west to east. To compare these data with the EUVI observations of a 3D plume, we need to first rotate the Sun from the EUVI observations to the time at which SUMER scanned it. An example is shown in the density map in the upper panel of Figure 5.12. The inclined lines are the projected positions of three plumes. The vertical line corresponds to the position of the SUMER slit at April 8 01:00 UTC. Consider plume 1, the plotted location was obtained by first rotating the Sun to this time and then projecting plume 1 onto the density map. From Figure 5.12 we can see that the projected plume 1 and the corresponding slit position are consistent.

The time at which the SUMER slit passes through the centers of the three plumes 0, 1 and 2 are April 8 02:00 UTC, April 8 01:00 UTC and April 7 22:00 UTC, is less than four hours after the EUVI observations. Due to the inclination of these three plumes, they are scanned by SUMER for about 2.5, 2 and 1 hours, respectively. We have checked the EUVI images at April 8 02:00 UTC, April 8 01:00 UTC and found that plume 0 and 1 were still present though the plumes appeared more diffuse at 02:00 UTC. For plume 3, we could not make a comparison because the time difference between the EUVI observation and the corresponding time at which it was scanned by SUMER is too large. Plume 4 in the EUVI observation lies outside the field of view of the SUMER scan. In Figure 5.12, the plus signs are the projections of the 3D plumes reconstructed from two EUVI images, the solid lines are their extrapolations outwards. We somewhat arbitrarily choose the upper end of height profile where the temperature by SUMER does not dramatically deviate from 0.9 MK. It makes the plumes more or less isothermal, which is an assumption for the later calculations. Furthermore, above $\approx$ 120 Mm the temperature plot is too noisy for a quantitative analysis. For the density, $\approx$ 150 Mm to 170 Mm might be an approximate limit.

We projected a 3D plume onto LOS Doppler shift map as well to get a more precise outflow velocity along the plume by dividing the SUMER velocity with the cosine of the plume inclination angle to the LOS. However, we did not find any significant Doppler shift
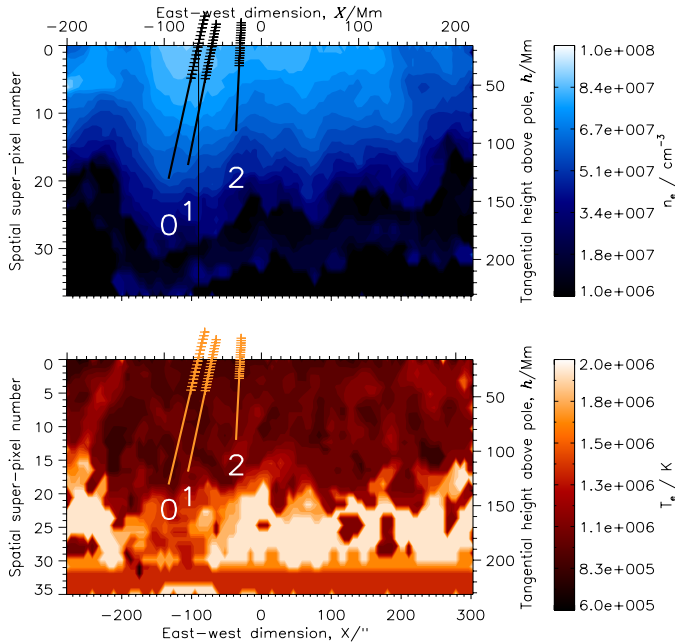
Figure 5.12: Projections of the 3D plumes 0, 1 and 2 onto the SUMER electron density (upper) and temperature (lower) map with the marked plume numbers. The vertical solid line in the density map corresponds to the position of SUMER slit at April 8 01:00 UTC. The plus signs are the projections of the 3D plumes reconstructed from two EUVI images recorded on April 7 and solid lines are the extrapolations downwards to the point where the standard deviation of the temperature along the plume is around 0.1 MK (Feng et al. 2009).

from SUMER observations, the maximum of the Doppler velocities is around 3 km/s. If we take this number as a reference to estimate the outflow velocities along the plumes 0, 1 and 2, we found that they are quite small with a maximum of 10 km/s which is too low to make plumes be a dominant contributor to the fast solar wind. This speed is much smaller than the sound speed $c_s \approx 140\,\text{km s}^{-1}$ for a temperature of ≈ 0.9 MK.

Similar to Gabriel et al. (2003), we have made an estimate of the plume contribution to the fast solar wind. The proton flux density for the high-latitude fast solar wind observed during the solar minimum from Ulysses at $r_E = 1$AU is 2.05×10^8 $\text{cm}^{-2}\,\text{s}^{-1}$ (McComas et al. 2000). We take the cross sectional area of the coronal hole from Munro and Jackson (1977) that matches the observed values extremely well,

$$A(r) = A_0 \left(\frac{r}{r_0}\right)^2 f(r), \qquad (5.2)$$

where the subscript 0 refers to quantities evaluated near the solar surface and $f(r)$ is
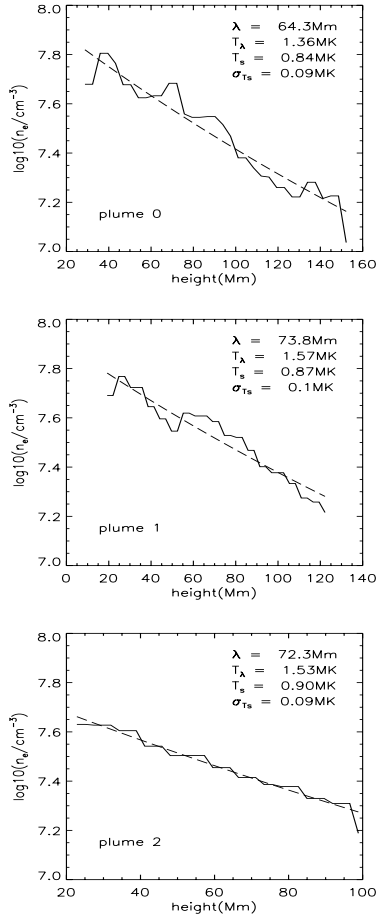
Figure 5.13: Logarithmic electron density along the plumes 0, 1, 2 from SUMER observation as a function of height above the solar surface as deduced from stereoscopic reconstructions (Solid lines). The dashed lines are fits based on hydrostatic equilibrium described by Equation 5.7. In the upper right of each figure we mark the numerical values for λ (density scale height), T_λ (temperature corresponding to scale height), T_s (electron temperature from SUMER) and its standard deviation σ_{T_s} (Feng et al. 2009).

the area expansion factor which reaches an almost constant value of 7.26 beyond 3 $R_\odot$. Therefore, the mean proton flux density mapped to the solar surface in the coronal hole is:

$$\frac{2.05 \times 10^8 \times A(r_E)}{A_0} = 2.05 \times 10^8 \times (\frac{r_E}{r_0})^2 \times 7.26 \, \text{cm}^{-2}\, \text{s}^{-1} \approx 6.88 \times 10^{13} \, \text{cm}^{-2}\, \text{s}^{-1}. \quad (5.3)$$

On the other hand, the electron flux density contributed by plumes are estimated by taking the maximal density in Figure 13 and maximal velocity of $10 \, \text{km}\, \text{s}^{-1}$, that is, $10^{7.8} \, \text{cm}^{-3} \times 10^6 \, \text{cm}\, \text{s}^{-1} \approx 6.31 \times 10^{13} \, \text{cm}^{-2}\, \text{s}^{-1}$. Comparing the mean flux density and the flux density from plumes, we find that the former is a little bit higher than the latter, and taking into account the filling factor of plumes in coronal holes of 10 % (Ahmad and Withbroe 1977), it is unlikely that the plumes investigated in this work are a dominant contributor to the fast solar wind.

We assume that the plume plasma is in hydrostatic balance considering their long lifetime of one or more days and the absence of any measurable flow. However, if the plasma ions are heated by, e.g., ion cyclotron waves a thermodynamic equilibrium does not necessarily exist since the plasma is mainly cooled by a divergent electron heat flux and by inelastic electron collisions with the ions (Tu and Marsch 1997). Following their two-fluid approach, the sum $p = p_i + p_e$ of ion and electron pressure has to obey

$$\frac{d}{dr}(p_i + p_e)(r) = -m_i n g_\odot \frac{R_\odot^2}{r^2} \quad (5.4)$$

Quasineutrality in this balance is insured by an ambipolar electric field which cancels when the momentum equations for ions and electrons are added. Here, m_i is the mean ion mass, n the plasma density and $g_\odot$ the gravity acceleration at the solar surface. For the total pressure we have

$$p = p_i + p_e = nk_B(T_i + T_e) = 2nk_B T_\lambda \quad (5.5)$$

Insertion and integration yields, changing the variable r to $h = r - R_\odot$

$$p = p_0 \exp\left(-\frac{m_i g_\odot}{k_B} \int_0^h \frac{R_\odot^2}{T_\lambda(R_\odot + h')^2} \, dh'\right) \quad (5.6)$$

For the small height range of our observations, we can neglect a possible height variation of T_λ inside the plumes. Then

$$n \simeq n_0 \exp\left(-\frac{m_i g_\odot}{k_B T_\lambda} \frac{h}{(1 + h/R_\odot)}\right) = n_0 \exp\left(-\frac{h}{\lambda_n(T_\lambda)(1 + h/R_\odot)}\right) \quad (5.7)$$

where the scale height $\lambda_n(T_\lambda)$ depends on $T_\lambda = (T_i + T_e)/2$ and n_0 is the density at $h = 0$ taken to be the base of the corona. For typical coronal mean mass m_i we have $\lambda_n(T_\lambda) \simeq 47 \, \text{Mm} \, (T_\lambda/\text{MK})$ (Aschwanden 2005b).

Since we know the density along the plumes from SUMER observations and we know the 3D height from the stereoscopic reconstructions, we can fit these two variables, n_e and h to derive T_λ and n_0 in Equation 5.7. In Figure 5.13, we present the results of fits based on Equation 5.7 to the density stratification of plumes 0, 1, 2. The calculated density scale height is given along with the corresponding temperature T_λ and the electron temperature deduced from SUMER T_s in Figure 5.13. We have invariably $T_\lambda > T_s$. The fits describe the data reasonably well suggesting that they are consistent with hydrostatic equilibrium.

5.4 Discussion and outlook

We have reconstructed the three dimensional geometry of ten polar plumes using simultaneous observations by the two *STEREO* spacecraft. For two different days, the locations of the footpoints of ten plumes and their inclinations were determined. Even though the statistical basis is small, we find that the plumes we could detect from the EUV images are homogeneously distributed over the polar cap. For both cases, the deviation of the plumes to the local meridian plane is rather small with an average of 6.47°. The deviation of the plume projection onto the local meridian plane from the local radial direction becomes larger in general with increasing distance of the plume from solar poles. For these two data sets, a simple dipole model with its axis along the solar rotation axis for the global magnetic field does, however, not provide a good description of the obtained inclinations. The magnetic field in these two coronal holes were more horizontal than this dipole field by 12.9° on average. The lower the latitude is, the larger is the deviation from the dipole field.

Moreover, we find that EUV plumes and EUV surface bright points are not always related, which is consistent with the observations of Wang (1998) and Raouafi et al. (2008). Of the three plumes in front of the solar limb on April 7, only one was definitely associated with a bright point. For the other two we did not find a related bright point. Conversely, we saw a bright point in the images to which no plume pair could be assigned to in the two EUVI images. A possible explanation could be that the lifetime of a bright point is shorter than the formation and decay time of a plume. Wang (1998) assumes a bright-point lifetime of around 12 hours, while for plumes he assumes lifetimes around one day. From the case study of June, we find that care is required when paring plumes with bright points. Spatial coincidence in a single image could easily be misleading.

For the data set in April, based on the results of 3D reconstruction and electron temperature, electron density and Doppler shift derived from the SUMER observations, we calculated the density scale height by assuming that a plume is in hydrostatic equilibrium. Using the reconstructed 3D direction of the plumes in space we could set an upper limit of 10 km s^{-1} for the outflow speed along the plumes. The absence of a significant flow in plumes at heights less than 1.2 $R_\odot$ is in agreement with the conclusions of Wilhelm et al. (2000) and Raouafi et al. (2007). The temperatures derived from the density scale height were all in excess of 10^6 K, while SUMER derived electron temperatures were well below 10^6 K from line ratios of Mg IX. The ratio of the temperature obtained from the scale height, T_λ, to the electron temperature from SUMER, T_s, is $T_\lambda/T_s \approx 1.6 - 1.8$. Recently, Del Zanna et al. (2008) found that the coronal electron temperatures derived from the Mg IX line ratio may have been underestimated. A coronal hole inter-plume temperature of 0.85 MK is now revised to 1.16 MK. This conclusion would reduce the discrepancy between the temperatures derived from the two techniques in our work, but would not eliminate it entirely. Even with this correction, $T_\lambda/T_s \approx 1.32$ to 1.46 remains. A possible explanation for this discrepancy could be a deviation of electron and ion temperatures. The scale height provides the average of the electron and the ion temperature while line-ratios depend on the electron temperature as shown in Chapter 2. The corrected ratio of T_λ to T_s corresponds to a ratio of the ion temperature to the electron temperature of from 1.64 to 1.92, which is qualitatively consistent with the result of Wilhelm (2006) derived from a different method. The effective ion temperatures he deduced from the line

widths are higher than the electron temperatures as well.

By comparing the stereoscopic reconstruction of polar plumes with other data, further fundamental questions related to plumes can be answered. One such application is the projection of the plume footpoints onto photospheric and chromospheric magnetograms. By analysing the magnetic polarities around the footpoint, we can test whether the plume is rooted in a unipolar magnetic field surrounded by several magnetic elements of the same polarity as suggested by Newkirk and Harvey (1968), or in a configuration as described by Wang (1998). According to the latter paper, a plume is formed by the reconnection of a unipolar magnetic flux with an emergent bipolar flux.

6   Conclusion and outlook

In this thesis we have reconstructed the 3D geometry of coronal loops in active regions and polar plumes in coronal holes by analysing image pairs taken by the EUVI/SECCHI instrument on board the twin STEREO spacecraft. Based on the studies of this thesis, the questions listed in the Summary could be answered to some extent. On the other hand, a number of further considerations has been raised which are summarized as an outlook after the conclusion.

Chapter 4 has presented how to reconstruct the 3D geometry of coronal loops and to obtain at the same time the best fit magnetic field lines selected from linear force-free field models with different force-free parameters. We find that the reconstructed 3D loops are neither circular, nor symmetric and even not confined in one plane. The calculated 3D loop lengths and loop heights are helpful to test loop scaling laws, calculate the true density scale heights, etc. Different force-free parameters are associated with different loop pairs. This means that the linear force-free models are sufficient to identify the loop correspondences from the image pairs, but do not yield a consistent magnetic field model for active regions. To better describe the magnetic properties, more sophisticated models, such as nonlinear force-free field models are required.

In Chapter 5, the 3D orientation and position of the polar plumes have been reconstructed. The deviation of the reconstructed plumes from the local meridian planes is quite small. Since plumes outlines the magnetic fields in the coronal holes, this small deviation means that the azimuthal magnetic field component B_φ is much less than the meridional components B_r and B_θ. We have found that the 3D plumes are inclined more horizontally than a dipole field having its axis along the solar rotation axis. The derived 3D orientation can be used as well to test other more complex global magnetic field models (Neukirch 1995). It is shown that the plumes and the EUV bright points are not one-to-one related. One of the explanations could be that comparing to the formation and decay time of plumes, the bright points have shorter lifetime (Wang 1998).

From SUMER observations, the temperature and density maps scanned around the polar cap are obtained. Together with the calculated 3D plume coordinates, the temperature and density distributions as a function of 3D height are derived. The density stratification agrees with the hydrostatic equilibrium reasonably well. We find that the temperature corresponding to the density scale height is invariably larger, around 1.6-1.8 times, than the temperature deduced from SUMER. A possible explanation could be a deviation of the electron and ion temperatures. The scale height depends on the average of the electron and ion temperatures, whereas the line-ratio techniques for SUMER measures the electron temperature. Generally the ion temperature is somewhat higher than the electron temperature. Finally, the outflow speeds corrected by the angle between LOS and the plume orientation give a maxima value of 10 km s^{-1}. This is too small to make plumes a

major contributor to the fast solar wind.

The 3D geometry of coronal loops and polar plumes is only the first step. Further investigations taking advantage of the 3D information are required for a deeper understanding of coronal loops and polar plumes. The outlook of this thesis is summarized below.

- By comparing the loop emissions synthesized from simulations with the observed emissions, we can obtain the information of how a loop is heated. A correct emission synthesis requires us to take into account the angle between the line-of-sight and the local tangent direction along the 3D loop.

- From two different viewpoints, two loop widths and then the shape of the loop cross section can be determined. Subsequently we can check how the cross section of loops varies with height in 3D. Is it consistent with the constant cross section from one-view results? If it is true, how do we explain the expanding flux tube from photosphere to corona?

- From the study of TRACE observations (Wang et al. 2008), it is shown that the 3D loop geometry helps to resolve different kink modes of transverse loop oscillations, whether horizontal or vertical. However, all the previous studies made the assumption that loops were confined in a plane. A complete image of how loops oscillate in 3D is required to more precisely determine some poorly known parameters, such as the mean magnetic field strength of coronal loops.

- It is also interesting to investigate quantitatively how loops change their configuration before and after eruptive events, for example, a flare. By checking the side view of reconstructed 3D loops we can tell whether they are more sheared or twisted before the occurrence of a flare. On the other hand, nonlinear force-free magnetic field extrapolations at the same time are also helpful to calculate the related free energies which are expected to become regularly available after the launch of the SDO mission.

- Considering the 3D orientation and location of polar plumes, the extrapolated footpoints on the solar surface need to be combined with the photospheric or chromospheric magnetograms to find out the magnetic properties at plume footpoints, whether unipolar or bipolar.

A   Differential geometric ridge definition

Consider a local smooth surface generated by the local 2D Taylor expansion of the intensity I at one cell center $\mathbf{i}$

$$I(\mathbf{x}) \simeq \tilde{I}(\mathbf{x}) = I(\mathbf{i}) + \mathbf{g}^T (\mathbf{x} - \mathbf{i}) + \frac{1}{2}(\mathbf{x} - \mathbf{i})^T \mathbf{H} (\mathbf{x} - \mathbf{i}) \qquad (A.1)$$

where the elements $\mathbf{g}$ and $\mathbf{H}$ are

$$\begin{pmatrix} g_x \\ g_y \end{pmatrix} = \begin{pmatrix} \frac{\partial}{\partial x} \\ \frac{\partial}{\partial y} \end{pmatrix} I(\mathbf{x}), \qquad (A.2)$$

$$\begin{pmatrix} H_{xx} & H_{xy} \\ H_{yx} & H_{yy} \end{pmatrix} = \begin{pmatrix} \frac{\partial^2}{\partial x^2} & \frac{\partial^2}{\partial x \partial y} \\ \frac{\partial^2}{\partial x \partial y} & \frac{\partial^2}{\partial y^2} \end{pmatrix} I(\mathbf{x}), \qquad (A.3)$$

we find that the diagonalization of $\mathbf{H}$ gives us the principal directions of the local surface and the ratio of the two principle curvatures as shown below.

From differential geometry it is known, that the vicinity of any point on a regular surface can be described by two tangent vectors - principal directions and two corresponding real numbers - principal curvatures (see Figure A.1). The principal directions and curvatures of the surface in general can be calculated from the Dupin indicatrix (Mei and Huang 2004) which is either one or a pair of conics in the tangent plane at one point $I(\mathbf{i})$ and for elliptical points the radius of the indicatrix in any direction is equal to the square root of the radius of curvature in that direction. The equation of the Dupin indicatrix is written as

$$Lx^2 + 2Mxy + Ny^2 = \pm 1 \qquad (A.4)$$

where for the surface in the form of $\mathbf{r} = (x, y, I(x, y))$,

$$L = \frac{\frac{\partial^2 I}{\partial x^2}}{\sqrt{1 + \left(\frac{\partial I}{\partial x}\right)^2 + \left(\frac{\partial I}{\partial y}\right)^2}}$$

$$M = \frac{\frac{\partial^2 I}{\partial x \partial y}}{\sqrt{1 + \left(\frac{\partial I}{\partial x}\right)^2 + \left(\frac{\partial I}{\partial y}\right)^2}}$$

$$N = \frac{\frac{\partial^2 I}{\partial y^2}}{\sqrt{1 + \left(\frac{\partial I}{\partial x}\right)^2 + \left(\frac{\partial I}{\partial y}\right)^2}} \qquad (A.5)$$
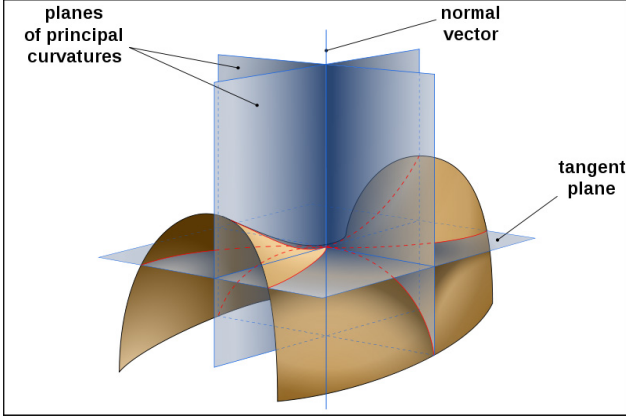
Figure A.1:   A schematic drawing of a local surface with its tangent plane, normal vector and two planes of principal curvatures.   The two principal directions align with the intersections of the two planes of principal curvatures with the tangent plane indicated by the blue lines on the tangent plane (http://commons.wikimedia.org/wiki/File:Minimal_surface_curvature_planes-en.svg).

The principal directions of the Dupin indicatrix which is also the principal directions of the local surface at $I(\mathbf{i})$ are calculated by diagonalizing the matrix

$$\begin{pmatrix} L & M \\ M & N \end{pmatrix} \tag{A.6}$$

the corresponding eigenvalues and eigenvectors are the principal curvatures and directions, respectively. From Equations A.3 and A.5 it can be easily shown that matrix $\mathbf{H}$ has the same eigenvectors and the difference in eigenvalues is only the coefficient $\left(1 + \left(\frac{\partial I}{\partial x}\right)^2 + \left(\frac{\partial I}{\partial y}\right)^2\right)^{-1/2}$.

If we assume the eigenvalues of $\mathbf{H}$ are $h_\perp$ and $h_\parallel$, the corresponding eigenvectors are $\mathbf{u}_\perp$ and $\mathbf{u}_\parallel$, respectively, we have

$$\mathbf{U}^\mathbf{T}\mathbf{H}\mathbf{U} = diag(h_\perp, h_\parallel), \tag{A.7}$$

in which $\mathbf{U} = (\mathbf{u}_\perp, \mathbf{u}_\parallel)$. Ordering $h_\perp$ and $h_\parallel$ so that $h_\perp \leq h_\parallel$, in the case that $\mathbf{i}$ is located exactly on a ridge, then $\mathbf{u}_\perp$ is the principal direction across and $\mathbf{u}_\parallel$ is the direction along the ridge, $h_\perp$ and $h_\parallel$ are the associated second derivatives of the image intensity in the respective directions. A positive ridge is identified according to Lindeberg (1998) in the following:

$$\mathbf{u}_\perp^T \nabla I = \mathbf{u}_\perp^T \mathbf{g} = 0 \qquad \text{a vanishing gradient across the ridge} \tag{A.8}$$

$$(\mathbf{u}_\perp^T \nabla)^2 I = h_\perp < 0 \qquad \text{a negative second-order derivative across the ridge} \tag{A.9}$$

$$|(\mathbf{u}_\perp^T \nabla)^2 I| > |((\mathbf{u}_\parallel^T \nabla)^2 I| \qquad \text{a 2nd order derivative magnitude across the}$$
$$\text{or} \quad |h_\perp| > |h_\parallel| \qquad \text{ridge larger than along} \tag{A.10}$$

B Derivation of Gaussian summation kernels

If we apply the first and second-order derivatives on Equation B.1

$$\bar{I}(\mathbf{x}) = \sum_{\mathbf{j}} w_d(\mathbf{x} - \mathbf{j})I(\mathbf{j}), \tag{B.1}$$

we obtain

$$
\begin{pmatrix} g_x \\ g_y \end{pmatrix} = \begin{pmatrix} \frac{\partial}{\partial x} \\ \frac{\partial}{\partial y} \end{pmatrix} \bar{I}(\mathbf{x}) = -\sum_{\mathbf{j}} \begin{pmatrix} \frac{2}{d^2}(x - j_x) \\ \frac{2}{d^2}(y - j_y) \end{pmatrix} w_d(\mathbf{x} - \mathbf{j})I(\mathbf{j})
$$

$$
= -\sum_{\mathbf{j}} \frac{2}{d^2}(\mathbf{x} - \mathbf{j})w_d(\mathbf{x} - \mathbf{j})I(\mathbf{j}) \tag{B.2}
$$

and

$$
\begin{pmatrix} H_{xx} & H_{xy} \\ H_{yx} & H_{yy} \end{pmatrix} = \begin{pmatrix} \frac{\partial^2}{\partial x^2} & \frac{\partial^2}{\partial x \partial y} \\ \frac{\partial^2}{\partial x \partial y} & \frac{\partial^2}{\partial y^2} \end{pmatrix} \bar{I}(\mathbf{x})
$$

$$
= \sum_{\mathbf{j}} \begin{pmatrix} \frac{4}{d^4}(x - j_x)^2 - \frac{2}{d^2} & \frac{4}{d^4}(x - j_x)(y - j_y) \\ \frac{4}{d^4}(x - j_x)(y - j_y) & \frac{4}{d^4}(y - j_y)^2 - \frac{2}{d^2} \end{pmatrix} w_d(\mathbf{x} - \mathbf{j})I(\mathbf{j})
$$

$$
= \sum_{\mathbf{j}} [\frac{4}{d^4}(\mathbf{x} - \mathbf{j})(\mathbf{x} - \mathbf{j})^T - \frac{2}{d^2}\mathbf{I_2}]\, w_d(\mathbf{x} - \mathbf{j})I(\mathbf{j}) \tag{B.3}
$$

Here and below summation over $\mathbf{j}$ always means over the limited support $\mathbf{j} \in [-m, m] \times [-m, m]$.

The above first and second-order derivatives are derived in the continuous case. To obtain the correct response on a discrete grid, we must modify the coefficients. We denote the various moments of a 1D Gaussian summed over the pixel grid by

$$
s_n = \sum_{j=-m}^{m} j^{2n} e^{-\left(\frac{j}{d}\right)^2} \rightarrow \begin{cases} \sqrt{\pi}d & n = 0 \\ \frac{1}{2}\sqrt{\pi}d^3 & n = 1 \end{cases} \quad \text{for large } d \ll m \to \infty \tag{B.4}
$$

We redefine $\mathbf{g}$ as in Equation B.2 but with a general coefficient c_1

$$
\mathbf{g}(\mathbf{x}) = -c_1 \sum_{\mathbf{j}} (\mathbf{x} - \mathbf{j})w_d(\mathbf{x} - \mathbf{j})I(\mathbf{j}). \tag{B.5}
$$

c_1 is determined so that we obtain unity at $\mathbf{x} = \mathbf{0}$ for a linear $I(\mathbf{j}) = j_x$ or j_y. Hence,

$$\begin{pmatrix} 1 \\ 0 \end{pmatrix} = c_1 \sum_{\mathbf{j}} \begin{pmatrix} j_x^2 \\ j_y j_x \end{pmatrix} w_d(\mathbf{j}) \tag{B.6}$$

which yields

$$c_1 = \frac{1}{c_0 s_0 s_1} = \frac{s_0}{s_1} \;\rightarrow\; \frac{2}{d^2} \quad \text{for large } d \ll m \to \infty. \tag{B.7}$$

For $\mathbf{H}$ we have with general coefficients c_2 and c_3 from Equation B.3

$$\mathbf{H} = \sum_{\mathbf{j}} [c_2(\mathbf{x} - \mathbf{j})(\mathbf{x} - \mathbf{j})^T - c_3 \mathbf{I_2}]\, w_d(\mathbf{x} - \mathbf{j}) I(\mathbf{j}) \tag{B.8}$$

The coefficients are determined by $\mathbf{H}$ at $\mathbf{x} = \mathbf{0}$

$$\begin{aligned}
\mathbf{H(0)} &= \sum_{\mathbf{j}} [c_2(-\mathbf{j})(-\mathbf{j})^T - c_3 \mathbf{I_2}]\, w_d(-\mathbf{j}) I(\mathbf{j}) \\
&= \sum_{\mathbf{j}} \begin{pmatrix} c_2 j_x^2 - c_3 & c_2 j_x j_y \\ c_2 j_x j_y & c_2 j_y^2 - c_3 \end{pmatrix} c_0\, e^{-\left(\frac{x}{d}\right)^2} e^{-\left(\frac{y}{d}\right)^2} I(\mathbf{j})
\end{aligned} \tag{B.9}$$

when $I(\mathbf{j}) = const$, we have $\mathbf{H(0)} = 0$ which yields $c_2 s_1 s_0 - c_3 s_0^2 = 0$. If $I(\mathbf{j}) = j_x j_y$, we come to

$$\mathbf{H(0)} = \begin{pmatrix} 0 & 1 \\ 1 & 0 \end{pmatrix} \tag{B.10}$$

from which we obtain $c_2 c_0 s_1^2 = 1$. Therefore,

$$\begin{aligned}
c_2 &= \frac{s_0^2}{s_1^2} \to \frac{4}{d^4} \quad \text{for large } d \ll m \to \infty \\
c_3 &= \frac{s_0}{s_1} \;\rightarrow\; \frac{2}{d^2} \quad \text{for large } d \ll m \to \infty
\end{aligned} \tag{B.11}$$

In the limit of large m, all coefficients have the values of the continuous differentiations.

C Projections of the 3D magnetic field lines onto EUV images

To project the 3D field lines onto two TRACE images we define three different coordinate systems. For a detailed introduction to the coordinate systems for solar images see Thompson (2006).

Heliographic coordinate system (HGC) The heliographic coordinate system is corotating with the solar surface. It is independent of the positions of the spacecraft. A position on the solar surface is generally specified by heliographic longitude and latitude coordinates (L, B) (in units of degrees). The position of the observer is usually localized in this coordinate system which can be found in the FITS header OBS_B0, $0BS\_L0$. The z axis of this HGC system is along the solar rotation axis, the x and y axes are in the heliographic equator plane towards $0°$ and $90°$ Carrington longitude, respectively. Numerical coordinate values are conveniently given in units of solar radius.

Heliocentric coordinate system (HCC) The coordinates of TRACE and EIT observation are heliocentric coordinate systems which are related to the spacecraft positions. This coordinate system has its origin in the solar center. The z axis points to the observer, the x axis is along the cross product of the z axes of the heliographic and heliocentric coordinate systems, and the y axis is the cross product of the z axis and x axis to make the system right handed. As mentioned earlier TRACE images are aligned with EIT data which have been mapped to the earth view, the position of viewpoint in the heliographic coordinate system then is given by the $EARTH\_B0$ and $EARTH\_L0$ in the FITS header of EIT data.

For an observing point (L, B) in the heliographic system, we can calculate the unit vectors along three axes of the corresponding heliocentric coordinate system. They are stored in the three columns of matrix A.

$$\begin{pmatrix} -\sin L & -\cos L \sin B & \cos L \cos B \\ \cos L & -\sin L \sin B & \sin L \cos B \\ 0 & \cos B & \sin B \end{pmatrix}$$

Given a vector $\mathbf{r}_{\mathrm{HGC}}$ represented by the three HGC coordinates, the projection along three unit vectors of HCC gives the coordinates of $\mathbf{r}_{\mathrm{HGC}}$ in the heliocentric coordinate system $\mathbf{r}_{\mathrm{HCC}}$. Therefore, the transformation from $\mathbf{r}_{\mathrm{HGC}}$ to $\mathbf{r}_{\mathrm{HCC}}$ can be expressed as

$$\mathbf{r}_{\mathrm{HCC}} = A^T \mathbf{r}_{\mathrm{HGC}}. \tag{C.1}$$

Conversely,

$$\mathbf{r}_{\mathrm{HGC}} = A \mathbf{r}_{\mathrm{HCC}}. \tag{C.2}$$

With these two expressions we can transform between the heliocentric coordinate systems for two TRACE (EIT earth) viewpoints.

Magnetic field extrapolation coordinate system (MEC) The Seehafer method of linear force-free field extrapolation is computed in a rectangular box with the bottom in the range of $[0 : L_x, 0 : L_y]$ covering the area chosen in the MDI magnetogram. To project the 3D magnetic field lines onto two TRACE images we should convert the coordinates in the MEC system to the coordinates in the two HCC systems of TRACE observations. The idea is that we first transform the MEC system to the HGC system and then to the two TRACE HCC systems respectively according to Equation C.1.

For convenience of transformation, we shift the origin of MEC coordinate system to the center of the selected region $(\frac{1}{2}L_x, \frac{1}{2}L_y)$ on the solar surface. Then the z axis points outwards from the coordinate origin along the connection line of the solar center and the shifted origin, the x and y axes lie in the plane vertical to the z axis. This MEC system is easily transformed to the HCC system by shifting the origin from the solar surface to the solar center and rescaling to the units of solar radius, as the numerical coordinate values in this extrapolation coordinate system are given in units of MDI pixels.

To transform the coordinates in the HCC system to the HGC system we should know the coordinate values (L, B) of the shifted MEC origin in the heliographic coordinate system. To find it we calculate its heliocentric coordinate values in units of arc seconds first from the pixel system by

$$x = CDELT1(i - CRPIX1) \tag{C.3}$$

$$y = CDELT2(j - CRPIX2) \tag{C.4}$$

$$z = \sqrt{R_\odot^2 - x^2 - y^2} \tag{C.5}$$

Here (i, j) are the coordinates of the origin in the pixel system, (x, y, z) are the coordinates in the heliocentric coordinate system. CDELT1, CDELT2, CRPIX1 and CRPIX2 are spatial resolutions in units of arcsec and the position of Sun center in the pixel system and can be found in the FITS header of MDI data. We rescale (x, y, z) values in units of arc seconds to the values in units of solar radius. Now the coordinate values of the origin can be transformed to the heliographic coordinates according to Equation C.1 to obtain the (L, B) coordinates of the origin.

With the calculated (L, B), now the coordinates of the 3D field lines in the HCC system can be converted to the coordinates in HGC system. The whole process from the MEC system to the HGC system is shown in Equation C.6.

$$\mathbf{r}_{\text{HGC}} = A_{\text{MEC}} \left(\frac{\mathbf{r}_{\text{MEC}} - (\frac{1}{2}L_x, \frac{1}{2}L_y, 0)^T}{R_\odot(\text{pixel})} + (0, 0, 1)^T \right) \tag{C.6}$$

where A_{MEC} is the coordinate transform matrix calculated from (L, B) of the origin of the MEC system. Then the coordinates in the TRACE HCC system are obtained by applying Equation C.1

$$\mathbf{r}_{\text{HCC}} = A_{\text{TRACE}}^T \mathbf{r}_{\text{HGC}} = A_{\text{TRACE}}^T A_{\text{MEC}} \left(\frac{\mathbf{r}_{\text{MEC}} - (\frac{1}{2}L_x, \frac{1}{2}L_y, 0)^T}{R_\odot(\text{pixel})} + (0, 0, 1)^T \right). \tag{C.7}$$

Here A_{TRACE} is the coordinate transform matrix from (L, B) of the TRACE spacecraft position. For the projections onto TRACE images, only x and y values of $\mathbf{r}_{HCC}$ are needed.

Bibliography

Ahmad, I. A., Webb, D. F., 1978, X-ray analysis of a polar plume, Sol. Phys., 58, 323–336

Ahmad, I. A., Withbroe, G. L., 1977, EUV analysis of polar plumes, Sol. Phys., 53, 397–408

Alexander, D., Katsev, S., 1996, Geometrical Considerations in Imaging the Solar Corona, Sol. Phys., 167, 153–166

Aschwanden, M. J., 2005a, 2D Feature Recognition And 3d Reconstruction In Solar Euv Images, Sol. Phys., 228, 339–358

Aschwanden, M. J., 2005b, Physics of the Solar Corona. An Introduction with Problems and Solutions (2nd edition), Pour la Science

Aschwanden, M. J., Fletcher, L., Schrijver, C. J., Alexander, D., 1999a, Coronal Loop Oscillations Observed with the Transition Region and Coronal Explorer, Astrophys. J., 520, 880–894

Aschwanden, M. J., Newmark, J. S., Delaboudinière, J.-P., Neupert, W. M., Klimchuk, J. A., Gary, G. A., Portier-Fozzani, F., Zucker, A., 1999b, Three-dimensional Stereoscopic Analysis of Solar Active Region Loops. I. SOHO/EIT Observations at Temperatures of (1.0-1.5) X 10ˆ6 K, Astrophys. J., 515, 842–867

Aschwanden, M. J., Alexander, D., Hurlburt, N., Newmark, J. S., Neupert, W. M., Klimchuk, J. A., Gary, G. A., 2000, Three-dimensional Stereoscopic Analysis of Solar Active Region Loops. II. SOHO/EIT Observations at Temperatures of 1.5-2.5 MK, Astrophys. J., 531, 1129–1149

Aschwanden, M. J., de Pontieu, B., Schrijver, C. J., Title, A. M., 2002, Transverse Oscillations in Coronal Loops Observed with TRACE II. Measurements of Geometric and Physical Parameters, Sol. Phys., 206, 99–132

Aschwanden, M. J., Burlaga, L. F., Kaiser, M. L., e. a., 2008a, Theoretical modeling for the stereo mission, Space Science Reviews, 136, 565–604

Aschwanden, M. J., Lee, J. K., Gary, G. A., Smith, M., Inhester, B., 2008b, Comparison of Five Numerical Codes for Automated Tracing of Coronal Loops, Sol. Phys., 248, 359–377

Aschwanden, M. J., Nitta, N. V., Wuelser, J.-P., Lemen, J. R., 2008c, First 3D Reconstructions of Coronal Loops with the STEREO A+B Spacecraft. II. Electron Density and Temperature Measurements, Astrophys. J., 680, 1477–1495

Aschwanden, M. J., Wülser, J.-P., Nitta, N. V., Lemen, J. R., Sandman, A., 2009, First Three-Dimensional Reconstructions of Coronal Loops with the STEREO A and B Spacecraft. III. Instant Stereoscopic Tomography of Active Regions, Astrophys. J.

Banaszkiewicz, M., Axford, W. I., McKenzie, J. F., 1998, An analytic solar magnetic field model, Astron. & Astrophys., 337, 940–944

Berton, R., Sakurai, T., 1985, Stereoscopic determination of the three-dimensional geometry of coronal magnetic loops, Sol. Phys., 96, 93–111

Bjoerck, Ä., 1996, Numerical Methods for Least Squares Problems, Cambridge University Press, 1996

Carcedo, L., Brown, D. S., Hood, A. W., Neukirch, T., Wiegelmann, T., 2003, A Quantitative Method to Optimise Magnetic Field Line Fitting of Observed Coronal Loops, Sol. Phys., 218, 29–40

Curdt, W., Wilhelm, K., Feng, L., Kamio, S., 2008, Multi-spacecraft observations of polar coronal plumes, Astron. & Astrophys., 481, L61–L64

DeForest, C. E., 2007, On the Size of Structures in the Solar Corona, Astrophys. J., 661, 532–542, arXiv:astro-ph/0610178

Deforest, C. E., Hoeksema, J. T., Gurman, J. B., Thompson, B. J., Plunkett, S. P., Howard, R., Harrison, R. C., Hassler, D. M., 1997, Polar Plume Anatomy: Results of a Coordinated Observation, Sol. Phys., 175, 393–410

DeForest, C. E., Lamy, P. L., Llebaria, A., 2001a, Solar Polar Plume Lifetime and Coronal Hole Expansion: Determination from Long-Term Observations, Astrophys. J., 560, 490–498

DeForest, C. E., Plunkett, S. P., Andrews, M. D., 2001b, Observation of Polar Plumes at High Solar Altitudes, Astrophys. J., 546, 569–575

Del Zanna, G., Rozum, I., Badnell, N. R., 2008, Electron-impact excitation of Be-like Mg, Astron. & Astrophys., 487, 1203–1208

Delaboudinière, J.-P., Artzner, G. E., Brunaud, J., Gabriel, A. H., Hochedez, J. F., Millier, F., Song, X. Y., Au, B., Dere, K. P., Howard, R. A., Kreplin, R., Michels, D. J., Moses, J. D., Defise, J. M., Jamar, C., Rochus, P., Chauvineau, J. P., Marioge, J. P., Catura, R. C., Lemen, J. R., Shing, L., Stern, R. A., Gurman, J. B., Neupert, W. M., Maucherat, A., Clette, F., Cugnon, P., van Dessel, E. L., 1995, EIT: Extreme-Ultraviolet Imaging Telescope for the SOHO Mission, Sol. Phys., 162, 291–312

Dwivedi, B. N., 1991, Forbidden line ratios from SI VIII and S X coronal ions, Sol. Phys., 131, 49–52

Dymova, M. V., Ruderman, M. S., 2006, The geometry effect on transverse oscillations of coronal loops, Astron. & Astrophys., 459, 241–244

Feng, L., Inhester, B., Solanki, S. K., Wiegelmann, T., Podlipnik, B., Howard, R. A., Wuelser, J.-P., 2007a, First Stereoscopic Coronal Loop Reconstructions from STEREO SECCHI Images, Astrophys. J., 671, L205–L208, `0802.0773`

Feng, L., Wiegelmann, T., Inhester, B., Solanki, S., Gan, W. Q., Ruan, P., 2007b, Magnetic Stereoscopy of Coronal Loops in NOAA 8891, Sol. Phys., 241, 235–249

Feng, L., Inhester, B., Solanki, S., Wilhelm, K., Wiegelmann, T., Podlipnik, B., Howard, R., Plunkett, S., Wuelser, J., Gan, W., 2009, Stereoscopic polar plume reconstructions from STEREO/SECCHI images, Astrophys. J., p. accepted

Fisher, R., Guhathakurta, M., 1995, Physical Properties of Polar Coronal Rays and Holes as Observed with the SPARTAN 201-01 Coronagraph, Astrophys. J., 447, L139–L142

Fowler, C. M. R., 2005, The Solid Earth, The Solid Earth, by C. M. R. Fowler, pp. 500. ISBN 0521584094. Cambridge, UK: Cambridge University Press, February 2005.

Gabriel, A. H., Bely-Dubau, F., Lemaire, P., 2003, The Contribution of Polar Plumes to the Fast Solar Wind, Astrophys. J., 589, 623–634

Giordano, S., Antonucci, E., Noci, G., Romoli, M., Kohl, J. L., 2000, Identification of the Coronal Sources of the Fast Solar Wind, Astrophys. J., 531, L79–L82, `arXiv: astro-ph/0001257`

Gopalswamy, N., Schmahl, E. J., Kundu, M. R., 1992, Observations of stationary radio sources: Coronal polar plumes?, in Coronal Streamers, Coronal Loops, and Coronal and Solar Wind Composition, (Ed.) C. Mattok, vol. 348 of ESA Special Publication, pp. 113–115

Guo, Y., Ding, M. D., Wiegelmann, T., Li, H., 2008, 3D Magnetic Field Configuration of the 2006 December 13 Flare Extrapolated with the Optimization Method, Astrophys. J., 679, 1629–1635

Handy, B. N., Acton, L. W., Kankelborg, C. C., e. a., 1999, The transition region and coronal explorer, Sol. Phys., 187, 229–260

Hassler, D. M., Dammasch, I. E., Lemaire, P., Brekke, P., Curdt, W., Mason, H. E., Vial, J.-C., Wilhelm, K., 1999, Solar Wind Outflow and the Chromospheric Magnetic Network, Science, 283, 810–813

Howard, R. A., Moses, J. D., Vourlidas, A., Newmark, J. S., Socker, D. G., Plunkett, S. P., Korendyke, C. M., Cook, J. W., Hurley, A., Davila, J. M., Thompson, W. T., St Cyr, O. C., Mentzell, E., Mehalick, K., Lemen, J. R., Wuelser, J. P., Duncan, D. W., Tarbell, T. D., Wolfson, C. J., Moore, A., Harrison, R. A., Waltham, N. R., Lang, J., Davis, C. J., Eyles, C. J., Mapson-Menard, H., Simnett, G. M., Halain, J. P., Defise, J. M., Mazy, E., Rochus, P., Mercier, R., Ravet, M. F., Delmotte, F., Auchere, F., Delaboudiniere,

J. P., Bothmer, V., Deutsch, W., Wang, D., Rich, N., Cooper, S., Stephens, V., Maahs, G., Baugh, R., McMullin, D., Carter, T., 2008, Sun Earth Connection Coronal and Heliospheric Investigation (SECCHI), Space Science Reviews, 136, 67–115

Inhester, B., 2006a, Stereoscopy basics for the STEREO mission, to appear as a Publ. of the Int. Space Sci. Inst., astro-ph/0612649, `astro-ph/0612649`

Inhester, B., 2006b, A Ridge Detector for EIT and TRACE Images, private manuscript

Inhester, B., Feng, L., Wiegelmann, T., 2008, Segmentation of Loops from Coronal EUV Images, Sol. Phys., 248, 379–393, `0801.3240`

Jackson, J. D., 1975, Classical electrodynamics, New York, Academic Press, 2nd ed., 1975

Klimchuk, J. A., 2000, Cross-Sectional Properties of Coronal Loops, Sol. Phys., 193, 53–75

Klimchuk, J. A., Antiochos, S. K., Norton, D., 2000, Twisted Coronal Magnetic Loops, Astrophys. J., 542, 504–512

Kouchmy, S., Molodensky, M. M., 1992, Three-dimensional image of the solar corona from white-light observations of the 1991 eclipse, Nature, 360, 717–719

Lang, K. R., 2001, The Cambridge Encyclopedia of the Sun, The Cambridge Encyclopedia of the Sun, by Kenneth R. Lang, pp. 268. ISBN 0521780934. Cambridge, UK: Cambridge University Press, October 2001.

Lee, J., Newman, T., Gary, G., 2006, Oriented connectivity-based method for segmenting solar loops, Pattern Recognition, 39, 246–259, ISSN 0031-3203

Lindeberg, T., 1998, Edge detection and ridge detection with automatic scale selection, International Journal of Computer Vision, 30, 117–154

Lundquist, L. L., Fisher, G. H., McTiernan, J. M., 2008a, Forward Modeling of Active Region Coronal Emissions. I. Methods and Testing, Astrophys. J., 179, 509–533

Lundquist, L. L., Fisher, G. H., Metcalf, T. R., Leka, K. D., McTiernan, J. M., 2008b, Forward Modeling of Active Region Coronal Emissions. II. Implications for Coronal Heating, Astrophys. J., 689, 1388–1405

Mariska, J. T., 1992, The solar transition region, Cambridge Astrophysics Series, New York: Cambridge University Press, |c1992

Marsch, E., Wiegelmann, T., Xia, L. D., 2004, Coronal plasma flows and magnetic fields in solar active regions. Combined observations from SOHO and NSO/Kitt Peak, Astron. & Astrophys., 428, 629–645

McComas, D. J., Barraclough, B. L., Funsten, H. O., Gosling, J. T., Santiago-Muñoz, E., Skoug, R. M., Goldstein, B. E., Neugebauer, M., Riley, P., Balogh, A., 2000, Solar wind observations over Ulysses' first full polar orbit, J. Geophys. Res., 105, 10 419–10 434

Mei, X. M., Huang, J. Z., 2004, Differential Geometry, Higher Education Press, 3rd Ed., in Chinese, 2004

Munro, R. H., Jackson, B. V., 1977, Physical properties of a polar coronal hole from 2 to 5 solar radii, Astrophys. J., 213, 874–886

Neukirch, T., 1995, On self-consistent three-dimensional analytic solutions of the magnetohydrostatic equations., Astron. & Astrophys., 301, 628–639

Newkirk, G. J., Harvey, J., 1968, Coronal Polar Plumes, Sol. Phys., 3, 321–343

Parent, P., Zucker, S., 1989, Trace Inference, Curvature Consistency, and Curve Detection, IEEE Transactions on Pattern Analysis and Machine Intelligence, 11, 823–839

Portier-Fozzani, F., Inhester, B., 2001, 3D Coronal structures and their evolutions measured by Stereoscopy, consequences for Space Weather and the STEREO mission, Space Science Reviews, 97, 51–54

Raouafi, N.-E., Harvey, J. W., Solanki, S. K., 2007, Properties of Solar Polar Coronal Plumes Constrained by Ultraviolet Coronagraph Spectrometer Data, Astrophys. J., 658, 643–656

Raouafi, N.-E., Petrie, G. J. D., Norton, A. A., Henney, C. J., Solanki, S. K., 2008, Evidence for Polar Jets as Precursors of Polar Plume Formation, Astrophys. J., 682, L137–L140

Raymond, J. C., Wood, K., 2000, Coronal Diagnostics, in Revista Mexicana de Astronomia y Astrofisica Conference Series, (Eds.) S. J. Arthur, N. S. Brickhouse, J. Franco, vol. 9 of Revista Mexicana de Astronomia y Astrofisica, vol. 27, pp. 32–39

Reale, F., Peres, G., Serio, S., Betta, R. M., DeLuca, E. E., Golub, L., 2000a, A Brightening Coronal Loop Observed by TRACE. II. Loop Modeling and Constraints on Heating, Astrophys. J., 535, 423–437

Reale, F., Peres, G., Serio, S., DeLuca, E. E., Golub, L., 2000b, A Brightening Coronal Loop Observed by TRACE. I. Morphology and Evolution, Astrophys. J., 535, 412–422

Riley, P., Linker, J. A., Mikić, Z., Lionello, R., Ledvina, S. A., Luhmann, J. G., 2006, A Comparison between Global Solar Magnetohydrodynamic and Potential Field Source Surface Model Results, Astrophys. J., 653, 1510–1516

Rosner, R., Tucker, W. H., Vaiana, G. S., 1978, Dynamics of the quiescent solar corona, Astrophys. J., 220, 643–645

Ruan, P., Wiegelmann, T., Inhester, B., Neukirch, T., Solanki, S. K., Feng, L., 2008, A first step in reconstructing the solar corona self-consistently with a magnetohydrostatic model during solar activity minimum, Astron. & Astrophys., 481, 827–834

Saito, K., 1965, Polar Rays of the Solar Corona, II., Publ. Astron. Soc. Japan, 17, 1–26

Scherrer, P. H., Bogart, R. S., Bush, R. I., Hoeksema, J. T., Kosovichev, A. G., Schou, J., Rosenberg, W., Springer, L., Tarbell, T. D., Title, A., Wolfson, C. J., Zayer, I., MDI Engineering Team, 1995, The Solar Oscillations Investigation - Michelson Doppler Imager, Sol. Phys., 162, 129–188

Schrijver, C. J., Aschwanden, M. J., Title, A. M., 2002, Transverse oscillations in coronal loops observed with TRACE I. An Overview of Events, Movies, and a Discussion of Common Properties and Required Conditions, Sol. Phys., 206, 69–98

Seehafer, N., 1978, Determination of constant alpha force-free solar magnetic fields from magnetograph data, Sol. Phys., 58, 215–223

Solanki, S. K., 1993, Smallscale Solar Magnetic Fields - an Overview, Space Science Reviews, 63, 1–2

Thompson, W. T., 2006, Coordinate systems for solar image data, Astron. & Astrophys., 449, 791–803

Török, T., Kliem, B., Titov, V. S., 2004, Ideal kink instability of a magnetic loop equilibrium, Astron. & Astrophys., 413, L27–L30, `arXiv:astro-ph/0311198`

Tu, C.-Y., Marsch, E., 1997, Two-Fluid Model for Heating of the Solar Corona and Acceleration of the Solar Wind by High-Frequency Alfven Waves, Sol. Phys., 171, 363–391

Wang, T., Solanki, S. K., Curdt, W., Innes, D. E., Dammasch, I. E., 2002, Doppler Shift Oscillations of Hot Solar Coronal Plasma Seen by SUMER: A Signature of Loop Oscillations?, Astrophys. J., 574, L101–L104

Wang, T. J., Solanki, S. K., 2004, Vertical oscillations of a coronal loop observed by TRACE, Astron. & Astrophys., 421, L33–L36

Wang, T. J., Solanki, S. K., Curdt, W., Innes, D. E., Dammasch, I. E., Kliem, B., 2003, Hot coronal loop oscillations observed with SUMER: Examples and statistics, Astron. & Astrophys., 406, 1105–1121

Wang, T. J., Solanki, S. K., Selwa, M., 2008, Identification of different types of kink modes in coronal loops: principles and application to TRACE results, Astron. & Astrophys., 489, 1307–1317, `0808.0685`

Wang, Y.-M., 1994, Polar plumes and the solar wind, Astrophys. J., 435, L153–L156

Wang, Y. M., 1998, Network Activity and the Evaporative Formation of Polar Plumes, Astrophys. J., 501, L145–L150

Wang, Y.-M., Sheeley, Jr., N. R., 1995, Coronal Plumes and Their Relationship to Network Activity, Astrophys. J., 452, 457–461

Warren, H. P., Winebarger, A. R., 2006, Hydrostatic Modeling of the Integrated Soft X-Ray and Extreme Ultraviolet Emission in Solar Active Regions, Astrophys. J., 645, 711–719, `arXiv:astro-ph/0602052`

Watko, J. A., Klimchuk, J. A., 2000, Width Variations along Coronal Loops Observed by TRACE, Sol. Phys., 193, 77–92

Wiegelmann, T., 2007, Nonlinear force-free modelling of the solar coronal magnetic field, J. Geophys. Res.

Wiegelmann, T., Inhester, B., 2006, Magnetic Stereoscopy, Sol. Phys., 236, 25–40, `arXiv:astro-ph/0612636`

Wiegelmann, T., Neukirch, T., 2002, Including stereoscopic information in the reconstruction of coronal magnetic fields, Sol. Phys., 208, 233–251, `0801.3234`

Wiegelmann, T., Inhester, B., Lagg, A., Solanki, S. K., 2005a, How To Use Magnetic Field Information For Coronal Loop Identification, Sol. Phys., 228, 67–78

Wiegelmann, T., Lagg, A., Solanki, S. K., Inhester, B., Woch, J., 2005b, Comparing magnetic field extrapolations with measurements of magnetic loops, Astron. & Astrophys., 433, 701–705, `0801.4519`

Wilhelm, K., 2006, Solar coronal-hole plasma densities and temperatures, Astron. & Astrophys., 455, 697–708

Wilhelm, K., Curdt, W., Marsch, E., Schühle, U., Lemaire, P., Gabriel, A., Vial, J.-C., Grewing, M., Huber, M. C. E., Jordan, S. D., Poland, A. I., Thomas, R. J., Kühne, M., Timothy, J. G., Hassler, D. M., Siegmund, O. H. W., 1995, SUMER - Solar Ultraviolet Measurements of Emitted Radiation, Sol. Phys., 162, 189–231

Wilhelm, K., Marsch, E., Dwivedi, B. N., Hassler, D. M., Lemaire, P., Gabriel, A. H., Huber, M. C. E., 1998, The Solar Corona above Polar Coronal Holes as Seen by SUMER on SOHO, Astrophys. J., 500, 1023–+

Wilhelm, K., Dammasch, I. E., Marsch, E., Hassler, D. M., 2000, On the source regions of the fast solar wind in polar coronal holes, Astron. & Astrophys., 353, 749–756

Wilhelm, K., Dwivedi, B. N., Curdt, W., 2009, Spectroscopic Diagnostics of Polar Coronal Plumes, ArXiv e-prints, `0902.4167`

Winebarger, A. R., Warren, H. P., 2004, Can TRACE Extreme-Ultraviolet Observations of Cooling Coronal Loops Be Used to Determine the Heating Parameters?, Astrophys. J., 610, L129–L132

Winebarger, A. R., Warren, H. P., Mariska, J. T., 2003, Transition Region and Coronal Explorer and Soft X-Ray Telescope Active Region Loop Observations: Comparisons with Static Solutions of the Hydrodynamic Equations, Astrophys. J., 587, 439–449

Wood, K., Raymond, J., 2000, Resonant Scattering of Emission Lines in Coronal Loops: Effects on Image Morphology and Line Ratios, Astrophys. J., 540, 563–571, `arXiv:astro-ph/0004131`

Wuelser, J.-P., Lemen, J. R., Tarbell, T. D., Wolfson, C. J., Cannon, J. C., Carpenter, B. A., Duncan, D. W., Gradwohl, G. S., Meyer, S. B., Moore, A. S., Navarro, R. L., Pearson, J. D., Rossi, G. R., Springer, L. A., Howard, R. A., Moses, J. D., Newmark, J. S., Delaboudiniere, J.-P., Artzner, G. E., Auchere, F., Bougnet, M., Bouyries, P., Bridou, F., Clotaire, J.-Y., Colas, G., Delmotte, F., Jerome, A., Lamare, M., Mercier, R., Mullot, M., Ravet, M.-F., Song, X., Bothmer, V., Deutsch, W., 2004, EUVI: the STEREO-SECCHI extreme ultraviolet imager, in Society of Photo-Optical Instrumentation Engineers (SPIE) Conference Series, (Eds.) S. Fineschi, M. A. Gummin, vol. 5171 of Society of Photo-Optical Instrumentation Engineers (SPIE) Conference Series, pp. 111–122

Young, P. R., Klimchuk, J. A., Mason, H. E., 1999, Temperature and density in a polar plume - measurements from CDS/SOHO, Astron. & Astrophys., 350, 286–301

Publications

Refereed scientific journals

- Feng, L., Wiegelmann, T., Inhester, B., Solanki, S., Gan, W. Q., Ruan, P.: Magnetic Stereoscopy of Coronal Loops in NOAA 8891, Solar Physics, 2007, 241, 235-249.

- Feng, L., Inhester, B., Solanki, S. K., Wiegelmann, T., Podlipnik, B., Howard, R. A., Wuelser, J.-P.: First Stereoscopic Coronal Loop Reconstructions from STEREO SECCHI Images, The Astrophysical Journal, 2007, 671, L205-L208.

- Feng, L., Inhester, B., Solanki, S.K., Wilhelm, K., Wiegelmann, T., Podlipnik, B., Howard, R.A., Plunkett, S.P., Wuelser, J.P., Gan, W.Q.: Stereoscopic Polar Plume Reconstructions from STEREO/SECCHI Images, The Astrophysical Journal, 2009, accepted.

- Inhester, B., Feng, L., Wiegelmann, T.: Segmentation of Loops from Coronal EUV Images, Solar Physics, 2008, 248, 379-393.

- Curdt, W., Wilhelm, K., Feng, L., Kamio, S.: Multi-spacecraft Observations of Polar Coronal Plumes, Astronomy and Astrophysics, 2008, 481, L61-L64.

- Ruan, P., Wiegelmann, T., Inhester, B., Neukirch, T., Solanki, S. K., Feng, L.: A First Step in Reconstructing the Solar Corona Self-consistently with a Magneto-hydrostatic Model during Solar Activity Minimum, Astronomy and Astrophysics, 2008, 481, 827-834.

Conference proceedings

- Feng, L., Wiegelmann, T., Inhester, B.: Magnetic Stereoscopy of Coronal Loops in NOAA 8891, in Modern Solar Facilities - Advanced Solar Science, Kneer, F., Puschmann, K.G., Wittmann, A.D. (Eds.), 2007.

Presentations and posters

- COSPAR (Committee on Space Research) Meeting, China, July 2006 (poster).

- Solar Image Processing Workshop 3, Ireland, September 2006 (oral).

- Modern Solar Facilities - Advanced Solar Science workshop, Germany, September 2006 (oral).

- SECCHI/STEREO Consortium Meeting 5, France, March 2007 (oral).

- Coronal Loop Workshop 3, Greece, June 2007 (two oral talks).

- International Study Team Meeting on Coronal Plumes and Inter-plume Regions, Switzerland, October 2007 (invited talk).

- SECCHI/STEREO Consortium Meeting 6, USA, November 2007 (poster).

- AGU (American Geophysical Union) Fall Meeting, USA, December 2007 (oral).

- Solar C Scientific Meeting, Germany, January 2008.

- EGU (European Geosciences Union) General Assembly 2008, Austria, April 2008 (oral).

- STEREO Workshop and SECCHI/STEREO Consortium Meeting 7, France, April 2008 (oral).

- AGU (American Geophysical Union) Spring Meeting, USA, May 2008 (invited talk).

- AOGS (Asia Oceania Geosciences Society) Conference, Korea, June 2008 (oral).

- NLFFF (Nonlinear Force-Free Field) Workshop 5, Germany, July 2008.

- STEREO Consortium Meeting 8, USA, October 2008.

- Solar Imaging Processing Workshop 4, USA, October 2008 (oral).

- International Study Team Meeting on Coronal Plumes and Inter-plume Regions, Switzerland, November 2008 (invited talk).

Acknowledgements

The research leading to this thesis was performed at the Max-Planck-Institute for Solar System Research (MPS) in Katlenburg-Lindau. I would like to thank MPS and especially the International Max Planck Research School (IMPRS) for giving me this great opportunity to carry out my PhD study in such a nice research atmosphere.

I greatly thank all my supervisors in MPS for their continuous support. Thanks Dr. Bernd Inhester for sharing his great insights in many fields of physics, mathematics and numeric methods. I am always wondering if there is something Bernd does not know. Thanks Dr. Thomas Wiegelmann for always helpful in solving various scientific problems and taking care of almost every step in my PhD research. Thanks Prof. Sami Solanki for his many new ideas in solar physics to inspire the interesting in my research. Thank all of you for giving me the opportunities of attending quite a number of conferences to know the frontier in relevant fields and present the work done by ourselves.

I am indebted to my supervisor Prof. Gan in China for keeping my position in Purple Mountain Observatory. No need to worry about the future job makes me concentrate on the study here.

I warmly thank Prof. Stefen Dreizler for accepting me as his student at the University of Goettingen and for always being helpful.

I am grateful to Dr. Klaus Wilhelm for dealing with the SUMER data and teaching me many rules on how to use Latex. Thanks Klaus for inviting me to the international plume team in Bern for two times which greatly enriches my understanding of plume researches. In MPS, I also would like to thank Borut Podlipnik for the help of installing softwares, providing the STEREO data in house and solving network problems.

Many thanks to the coordinator of IMPRS Dr. Dieter Schmitt, for keeping the research school in such a good order.

Thanks my officemate Megha for always encouraging me by asking when you will start the next chapter of your thesis and discussing about life and science. Thanks Zhi, Mingyuan who left Lindau a few months ago for the good time spent together and keeping encouraging me by emails and phone calls. My thanks also go to Jingnan, Peng, Shuo, Julia, Philippe, Hui, Shangbin, Roberto, Jie, Judith and new students Yeon Joo and Supriya in Lindau and Xianyi in Branschweig.

Finally I want to thank my parents and my younger sister for their support through the years and thank my husband Shu for his understanding and taking caring of me in the last two months of my PhD life.

Lebenslauf

Persönliche Daten

Name: Li Feng

Geburtstag: 18.01.1981

Geburtssort: Taixing, Jiangsu, China

Staatsbürgerschaft: Chinesisch

Schulbildung

09/1995-06/1998:   Mittelschule in Taixing, Provinz Jiangsu, China

Studium

09/1998-06/2002:   Studium in Mathematik, Arbeit in Angewandte Mathematik, Nanjing Paedagogische Universität, Nanjing, China. Abschluß: Bachelor of Science

09/2002-06/2005:   Diplomarbeit in Physik, Arbeit in Astrophysik, Purpur Berg Observatorium (PMO), Nanjing, China. Abschluß: Master of Science

01/2006-03/2009:   Doktorarbeit am dem Max-Planck-Institut für Sonnensystemforschung, Katlenburg-Lindau, und der George-August Universität, Göttingen.